UNIVERSIDADE DE SANTIAGO DE COMPOSTELA

FACULTAD DE FÍSICA
Departamento de Física de Partículas

Fission studies in inverse kinematics and associated development of new time-of-flight detectors

Memoria presentada por:
Yassid Ayyad Limonge
como disertación para optar al
Grado de Doctor
en Ciencias Físicas
Junio 2012

UNIVERSIDADE DE SANTIAGO DE COMPOSTELA

José Benlliure Anaya, Catedrático de Física Atómica, Molecular y Nuclear de la Universidad de Santiago de Compostela y **Carlos Paradela Dobarro**, investigador contratado de la Universidad de Santiago de Compostela,

CERTIFICO: que la memoria titulada **Fission studies in inverse kinematics and associated development of new time-of-flight detectors** ha sido realizada por **Yassid Ayyad Limonge** en el **Departamento de Física de Partículas** de esta Universidad bajo mi dirección y constituye el trabajo de **tesis** que presenta para optar al **Doctor en Ciencias Físicas**.

Santiago de Compostela, Junio de 2012

Fdo: José Benlliure Anaya

Fdo: Carlos Paradela Dobarro

Fdo: Yassid Ayyad Limonge

Contents

Introduction

Soon after its discovery in 1938 by Hahn and Strassmann [Hah39], the first description of the fission process was given by Bohr-Wheeler [Boh39] in their transition-state theory based on the liquid-drop model. However, fission is an extremely complex mechanism that requires a dynamical approach to describe the evolution of the process in terms of intrinsic and collective excitation of the nuclear constituents. Transport theories [Wei80] based on Langevin calculations has proven to be a suitable tool for the description of the collective evolution of the nuclei and they constitute the basis of most of the current theoretical models. Nevertheless, more than 70 years of intense research reveal that fission is still far from being understood and the theoretical and experimental knowledge is unsatisfactory. The measurement with high precision and resolution of signatures such as fission probabilities, masses and nuclear-charges, fission fragment kinetic energies and light particles and γ-ray multiplicities is limited by the available technology and results obtained with different techniques and setups present several inconsistencies. A substantial improvement is needed to address the existing discrepancies, validate newly developed models and extend the present limits of our understanding of the fission process.

The nuclear fission plays a key role in the description of several nuclear properties and provides valuable information in general physics and astrophysics. Indeed, topics such as shell effects in super- and hyper-deformed nuclei, r-process in the nucleosynthesis, viscosity of the nuclear matter and heat transfer between nascent fragments need a good knowledge of the fission process. Fission is also extremely important in the production of radioactive ion beams (RIB) to study the properties of exotic neutron-rich nuclei far from the stability [PL11], nuclear power installations and the development of spallation neutron sources for ADS (Accelerator Driven System) technologies among others.

In the present work we have investigated the proton-induced fission of ^{181}Ta and proton- and deuteron-induced fission of ^{208}Pb at relativistic energies. The experiments were conducted at GSI (Darmstadt) by using a dedicated setup for fission studies in inverse kinematics. This setup facilitated the counting of the projectiles and the identification of the reaction products. The unambiguous determination of both fission fragments simultaneously, with high efficiency and acceptance, allowed us to disentangle fission from other reaction channels and measure, with high precision, the total fission cross section for ^{181}Ta+p at 1000, 800, 500 and 300 A MeV, and, for ^{208}Pb+p and ^{208}Pb+d at 500 A MeV. We investigated the effect of the nuclear dissipation in the fission probability, especially in the ^{181}Ta+p reaction where a wide range in excitation energy was covered. Moreover, in the ^{208}Pb case, the charge identification of both fission fragments made it possible to reconstruct the charge of the fissioning nuclei and classify each fission event according to its excitation energy and impact parameter. The partial fission cross sections and the width of the fission fragments charge distribution as a function of the charge of the fissioning nuclei were carefully determined for the reactions ^{208}Pb+p and ^{208}Pb+d. The use of two different targets allowed us to explore the effect of the excitation energy on the fissioning system. These observables were used to extract quantitative results about dissipative effects and dynamical times in the pre-saddle stage of the fission process with the support of state-of-the-art nuclear reaction-codes including an analytical solution of the Fokker-Plank equation (FPE) to describe the dynamical evolution of the fission process.

The combination of the inverse kinematics technique and a dedicated experimental setup is a powerful tool to perform fission experiments since all fission fragments leave the target with high kinetics energies in forward direction and their properties can be determined with high accuracy. However, the isotopic identification of both fission fragments simultaneously with high precision and resolution has never been achieved and still is a long-standing problem still present in the most modern detection setups. The scientific program of the forthcoming R^{3}B experiment at FAIR facility (Germany) will include the complete study of fission, spallation and multi-fragmentation reactions in inverse kinematics by using an improved detection scheme similar to that of the present work including a powerful dipole magnet. The isotopic identification of the fission and spallation fragments will require state-of-the-art time-of-flight detectors with high efficiency, acceptance and time resolution below 30 ps. To fulfill these requirements, a time-of-flight wall based on RPC (Resistive Plate Chambers) detectors is proposed. RPCs are widely-used timing detectors in several high-energy physics experiments around the world. However, the present information concerning their response when detecting ions at relativistic energies is scarce. In this work, we have investigated the performance of RPC prototypes under relativistic heavy ion irradiation. The efficiency and time resolution of the prototypes were determined using ion beams with different atomic numbers and electron beams. The obtained results indicate the feasibility of RPC detectors for the detection of heavy ions and the construction of such a time-of-flight wall.

This manuscript is organized as follows: In Chapter 1 a review on the basic ideas of the dynamics of the fission process and different experimental approaches to measure them are discussed. Chapter 2 includes the results of the experiment aiming at measuring proton-induced fission of ^{181}Ta at several relativistic energies, presenting a detailed explanation of the data reduction and the considered uncertainties. In addition, the data are compared with calculations performed with different nuclear-reaction codes and several concepts about the fission probability and dissipation are discussed. Chapter 3 includes an analog description of the Chapter 2 for the reactions ^{208}Pb+p and ^{208}Pb+d using an improved fission setup. A detailed discussion on transient and dissipative effects in the fission process is also included in this chapter. Finally, the objective of Chapter 4 is to introduce the forthcoming experiments measuring fission in inverse kinematics and the state-of-the-art time-of-flight detectors that will be deployed in these experiments. The development of timing RPCs (tRPCs) as proposed technology for time-of-flight measurements of fission residues within the R^{3}B framework is explained in this chapter.

Chapter 1

Fission dynamics and experimental signatures

The aim of this chapter is to compile different theoretical and experimental aspects of the dynamics of the fission process. The section 1.1 is devoted to the description of the current and most accepted picture of the nuclear fission. The concept of dissipation and its effects are introduced as well as several theoretical approaches based on transport theories determining its magnitude. Section 1.2 includes an insight into the experimental observables to probe dissipative effects and a discussion about the validity and reliability of each signature. In the section 1.3, the reaction mechanism to induce fission used in the experiment of the present work is described. The experimental technique and the exploited signatures are carefully explained, and, an overview of state-of-the-art codes utilized in this work to infer quantitative results on dissipation is given.

1.1. Present understanding of the fission process

Fission is the splitting of a highly-deformed heavy nucleus in two fragments with comparable mass as a consequence of the large-scale collective motion of nucleus constituents. The evolution of the process depends on the initial conditions of the fissioning nuclei (namely its excitation energy, angular momentum and shape) and the potential as a function of the deformation and mass asymmetry. The process can occur spontaneously for very heavy nuclei, or can be induced. In the latter case, the excitation energy transferred to the system is transformed into collective motion of most of its constituents that induces a significant deformation on it. During the evolution of the fissioning system along the deformation coordinate, there exists a competition between the surface contribution to the binding energy which opposes the deformation of the system, and, the decreasing Coulomb energy due to the separation of the nuclear charge, which favours the split of the system in two fragments. As a consequence, as can be seen in Fig. 1.1, the potential landscape that guides the nuclear shape evolution appears in the deformation and asymmetry coordinates. A threshold excitation energy is needed to promote the nuclei from the ground-state configuration above the saddle point, to the zone of the potential in which the separation of both fragments occurs. The different symmetric and asymmetric fission modes correspond to specific valleys represented in this landscape.

The fission process, the potential landscape and the mass asymmetry are often described using fully dynamical microscopic models based on Hartree-Fock and Hartree-Fock-Bogoliubov methods [Ber84; Gou05] or macroscopic-microscopic models [Möl01]. In the latter, the macroscopic term corresponds to the liquid-drop model potential energy modified according to the microscopic energy term that accounts for nuclear shell structure effects, which are responsible of the observed asymmetric mass distributions, and pairing correlations [Str67]. Both are especially strong in low energy fission. However, the precision of these theoretical models in the prediction of some key observables such as the mass-yield curve is limited due to the complexity of the involved many-body calculations. Moreover, owing to fission is a time-dependent process, static potential energy surfaces are insufficient and not all models include a dynamical treatment of the process.

Since a microscopic treatment presents severe restrictions and problems, the dynamics of the fission process can be described with the help of macroscopic variables which fluctuates in a stochastic way. Using transport theories one can describe this evolution with collective and intrinsic degrees of freedom which corresponds to coordinate motion and individual state of the nucleons, respectively. Thus, fission dynamics is governed by the evolution of collective parameters.

1.1.1. Dynamical effects in fission

In order to describe the evolution of the fissioning system and its collective degrees of freedom, Kramers [Kra40], in 1940, proposed an interpretation of the fission process as a diffusion process within the framework of transport theories. In this description, in analogy to the Brownian motion, the collective degrees of freedom move in an external field force affected by the heat bath of the individual nuclear constituents, which corresponds to the internal degrees of freedom of the system. The equation of motion is given

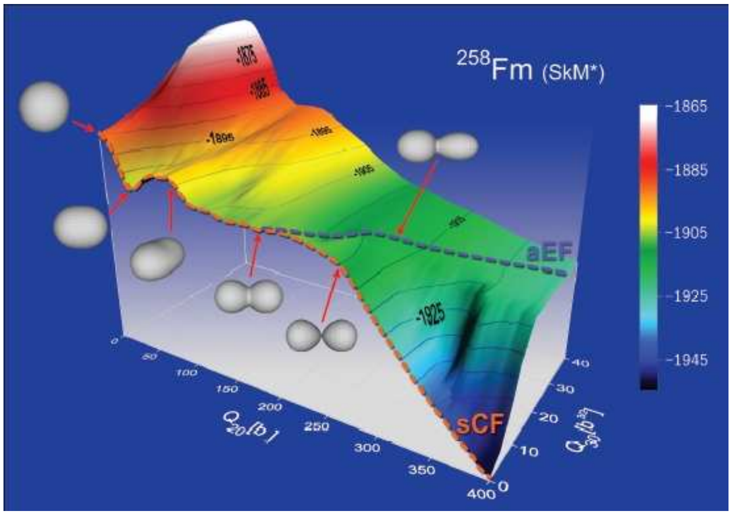

Figure 1.1: Representation of the potential landscape of ^{258}*Fm as a function of the nuclear deformation* (Q_{20}) *and the asymmetry* (Q_{30}). *Figure taken from [Sci07]*

by the specific Langevin equation:

$$\frac{dv}{dt} = -\beta v - \frac{1}{m}\frac{\partial}{\partial x}U(x) + \frac{F'(t)}{m} \tag{1.1}$$

where $U(x)$ is the nuclear deformation potential and $F'(t)$ its the stochastic external force and v is the velocity. The term βv is the friction force derived from the interaction of the system with the surrounding medium. Owing to the random nature of $F'(t)$, the Langevin equation should be solved in each case to describe the motion of all constituents involved. However, instead of that, the Fokker-Planck equation (FPE) [Ris89] describing the evolution of the system according to the time-dependent probability distributions $W(x, v, t)$ of finding the system with a given velocity v and time t, is used. Assuming the time the collective degrees of freedom needs to make a significant change is much larger than the relaxation time of the internal degrees of freedom [Wei80], the FPE expression is:

$$\frac{dW}{dt} = \left[-\frac{\partial}{\partial x}v + \frac{\partial}{\partial v}\left(\beta v - \frac{1}{m}\frac{\partial}{\partial x}U(x)\right) + \frac{\beta k T}{m}\frac{\partial^2}{\partial v^2}\right] W \tag{1.2}$$

where k is the Boltzmann's constant and T is the temperature of the heat bath. The stationary solution of the FPE found by Kramers accounts for the reduction of the fission width predicted by Bohr-Wheeler's model by taking into account the nuclear dissipation:

$$\Gamma_f^K = \Gamma_f^{BW} \left(\left[1 + \left(\frac{\beta}{2\omega_0} \right)^2 \right]^{1/2} - \frac{\beta}{2\omega_0} \right) \tag{1.3}$$

where Γ_f^{BW} is the fission decay width predicted by Bohr-Wheeler's statistical model, and, ω_0 is the frequency of the harmonic-oscillator of the inverted potential at the saddle point. β is the dissipation coefficient which is explained as the excitation energy exchange between collective degrees of freedom and the heat bath. If the energy transfer flows from collective to intrinsic degrees of freedom the nucleus motion along the deformation coordinate is slowed preventing it to cross the saddle point with a certain probability and, therefore, the fission chance is reduced because the nucleus cools down by evaporation.

Kramers picture was not established until Bohr-Wheeler model failed in reproducing neutron and γ-ray experimental multiplicities of Gavron *et al.* work [Gav81; Gav82], and, consequently led to an overestimation of the fission rate. This fact revealed that a dynamical description of the process was needed in order to explain the hindrance of the fission channel owing to the competition with particle evaporation.

1.1.2. Transient effects induced by nuclear dissipation

Motivated by the results obtained by Gavron *et al.*, Grangé and collaborators [Gra83] investigated the effects of the nuclear dissipation on the temporal evolution of the fissioning system. Grangé *et al.* found a time-dependent fission decay width, $\Gamma(t)$ by numerically solving a time-dependent FPE equation, and, considering an initial system in the deformation ground-state with high intrinsic excitation energy. According to this solution, during the early stage of the process, $\Gamma(t)$ is completely suppressed and needs a transient time, τ_f (less than 10^{-21} s), to reach the 90% of its asymptotic value (see upper panel of Fig. 1.2), which corresponds to Kramers fission decay width [Bha86]. The strong competition with the evaporation of neutrons during this time can cool down the compound nucleus preventing it undergo fission. Usually, the internal equilibration time of the internal degree of freedom is short compared to the characteristic time of the diffusion process itself and the decay times. Transient regime only manifests at high excitation energies where the average decay time of the system is comparable with the relaxation time of the degree of freedom. At lower excitation energies the evolution of the fissioning system is ruled by the phase space and Bohr-Wheeler's transient-state model is applied.

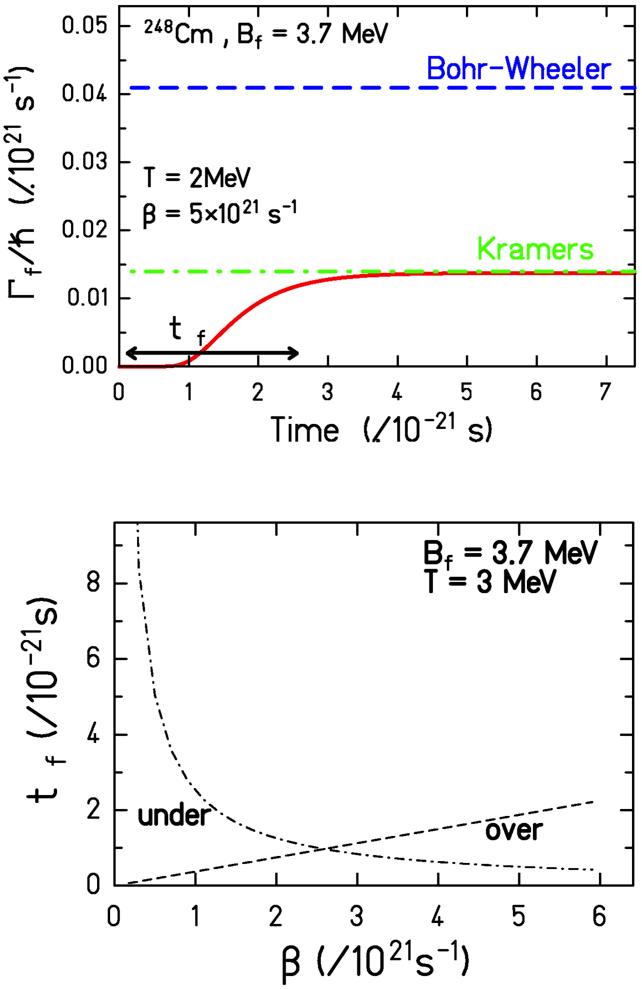

Figure 1.2: Upper panel: Fission rate as a function of time. The dashed and the dashed-dotted line corresponds to Bohr-Wheeler (Γ_f^{BW}) and Kramers fission rate (Γ_f^K), respectively. The solid line represents the numerical solution of the FPE, $\Gamma(t)$ [Bha86] for a system with A=248, $\beta = 5 \times 10^{21} s^{-1}$ and T=2 MeV. Lower panel: Transient time as a function of the dissipation coefficient for a system with A=248 and T=3 MeV.

Transient time emerges from the idea underlying the complex description of the energy transfer rate between collective and intrinsic degrees of freedom. The relation between the reduced dissipation coefficient and the transient time is [Bha86]:

$$\begin{aligned} \tau_f &= \tfrac{1}{\beta}\ln\left(\tfrac{10B_f}{T}\right) \qquad for\ \beta < 2\omega_{gs} \\ \tau_f &= \tfrac{\beta}{2\omega_{gs}^2}\ln\left(\tfrac{10B_f}{T}\right) \qquad for\ \beta > 2\omega_{gs} \end{aligned} \tag{1.4}$$

where ω_{gs} the oscillation frequency at the ground state, B_f the fission barrier height and T is the temperature. The value of β defines the dissipation regime (see lower panel of Fig. 1.2). For $\beta<2\omega_{gs}$, the system follows an underdamped regime characterized by the fast energy transfer of intrinsic excitation energy into collective degree of freedom as β increases. If $\beta>2\omega_{gs}$, τ_f increases with increasing β. In this case, the energy is injected very fast but the time the system needs to reach the stationary regime is increased owing to the damping of the motion of the collective degree of freedom in the deformation space. There exists a critical damping in which the compromise between the energy transfer rate and collective motion hindering leads to the shortest transient time.

1.1.3. Determination of nuclear dissipation strength

The determination of the magnitude of the dissipation coefficient β is still nowadays under debate and several transport theories provide different quantitative results. In this section, a brief summary of other theories explaining the nuclear dissipation are presented. Hofmann and collaborators [Hof97; Hof01] extended Kramers picture into quantal formalism. In this theory, the equation of motion of the collective degree of freedom is expressed using transport coefficients which depends on the deformation and the temperature:

$$M\frac{d^2x}{dt} + \eta\frac{dx}{dt} + Cx(t) \tag{1.5}$$

where M is the inertia coefficient, η is the friction coefficient and C is the stiffness coefficient. The expression for the dissipation coefficient depends strongly on the temperature (T):

$$\beta(T) \approx \frac{0.6T^2}{1+\frac{T^2}{40}} \tag{1.6}$$

Also within the framework of Langevin equations, Fröbich and co-workers [Frö98] introduced a deformation-dependent dissipation coefficient using the combined dynamical statistical model (CDSM). At the beginning of the process, for compact nuclear shapes, the magnitude of the dissipation coefficient is rather small ($\beta \approx 2 \times 10^{21}\ s^{-1}$). During the deformation of the nuclei, the value of β increases up to $30 \times 10^{21}\ s^{-1}$ at the scission point. Using this parametrization, this model explains the fission probabilities and pre-saddle neutron multiplicities, especially for systems with long saddle-to-scission path.

Another phenomenological theory is that of the wall and window formula for one-body dissipation [Blo78]. Based on the Gross model [Gro75], the wall formula describes the dissipation as the interaction of the nuclear constituents with the nuclear potential, which is represented as a moving wall compressing the nucleons. The energy dissipated by this moving wall is proportional to the velocity of nucleons in a Fermi gas and their mass density. An improved wall friction formulation [Cha01] reveals a strong suppression of the friction strength of $\beta \approx 2 \times 10^{21}\ s^{-1}$. On the other hand, the window formula is applied to the scission of the fissioning system, where two sub-systems are communicated through a small window. In this formula, the energy dissipation is proportional to the velocity of the particles moving in each sub-system, and, to the area of the window.

The dissipative diabatic dynamics (DDD) approach was introduced by Nörenberg [Nör83] to describe heavy-ion collisions at few A MeV. According to this picture, based on the adiabatic theorem, the single-particle (nucleons) motion is coherently coupled to a time-dependent mean field. The diabatic excitation of single-particles and holes produces repulsive forces on the collective motion which kinetic energy is stored as a conservative potential. An incoherent coupling introduced by residual two-body collisions (interaction between nucleons) leads to equilibrium by destroying the diabatic part of the potential and dissipating the stored energy. Therefore, the dissipation term of the equation of motion of the collective degree of freedom includes a time retardation. In this theory, the dissipation coefficient is proportional to $1/T^2$ and a estimated value of $\beta \approx 40 \times 10^{21}\ s^{-1}$ at $T = 2.5$ MeV [Hil92]

1.2. Experimental observables probing nuclear dissipation

In this section, the standard observables of the fission process sensitive to dissipation and transient effects and the experimental approaches are discussed. Most representative experiments exploited observables such as fission probabilities or pre-saddle particle multiplicities to extract information about the time evolution of the process, whereas others used sophisticated clocks to directly measure the times involved in it. An overview of the most representative techniques and observables is presented in this section.

1.2.1. Fission cross sections

Fission probabilities are the most suitable observable to investigate the effects of the nuclear dissipation during the pre-saddle phase of the fission process. If transient effects are considered, the fission channel is completely suppressed at the early stage of the process. During that delay, the fissioning nucleus is cooled down by particle evaporation, hence, the temperature of the system at the saddle point and its fissility is reduced. This effect is more prominent at higher excitation energies where the evaporation time is shorter. Moreover, as explained before, the dissipation also reduces the asymptotic value of the fission width predicted by the transition-state model. These two effects significantly reduce the fission cross section. The evaporation residue cross sections were also investigated to extract more information about pre-saddle dynamics [Frö98]. However, the interpretation of dissipative effects using the fission and evaporation residues cross sections needs the support of model calculations which depends on parameters such as the ratio of level density parameters a_f/a_n and the magnitude of the fission barriers. Fission cross sections will be investigated in the next chapters of this work.

1.2.2. Direct measurements using atomic clocks

The direct measurement of the times involved in the fission process is a difficult and challenging task with a limited sensitivity. These kind of measurements give access to the information of the time evolution of the system up to scission. Two methods has been used: the filling of the K-shell hole created in the collision of the nuclei with the inner electrons of an atom of a given medium [Mol93] and the crystal blocking technique [Gol99].

In the former, created vacancies in the inner shells are occupied by electrons of the outer shell emitting characteristic X-rays which decay line-width determine the lifetime of that vacancy. The characteristic X-ray allows to distinguish whether it was emitted due to the interaction with fission fragments or before scission of the nuclei. Assuming a known probability for a vacancy creation and an exponential decay law for the processes, the scission time is determined with an X-ray emitted by a pre-scission vacancy in coincidence with the fission fragments. Owing to the precision of the method, only upper limits for the scission time of the order of 10^{-18} s have been estimated [Wil04].

In the blocking technique, charged particles moving inside a single crystal along the direction of an specific axis are deflected owing to atomic interactions with the atoms. Thus, the angular distribution of the emerging particles presents a characteristic dip due to the blocking or deflection. In the fission case, an excited nuclei is created inside the crystal with a recoil velocity. The depth and the shape of the dip of the angular distribution depends on where the fission fragments are emitted after the path travelled by the recoiling nuclei. Therefore, this is connected to the total scission time. The sensitivity of this method, which is around 10^{-19} s, is limited by the thermal vibrations of the crystal atoms.

1.2.3. Nuclear clocks: Light-particle and γ-ray emission

The number of emitted light-particles, namely neutrons, and γ-ray yield valuable information about fission time scales prior to scission. The number of emitted particles is linked to the time the nucleus needs to reach the saddle point, thus, for longer times, the multiplicities are higher. In the case of neutron emission (neutron clock [Hil92; Hin92]), the lifetime in the pre-scission stage (τ_f) is basically the sum of the mean evaporation time of each emitted particle (τ_n), which is calculated according to the statistical model. At high excitation energies, the pre-scission time is approximated using the excitation energy at the scission point (E^*_{sci}) which is reconstructed using the post-scission neutron multiplicities: $\tau_f \approx \tau_n E^*_{sci}$. Pre- and post-scission multiplicities are discriminated by their kinematics.

The γ-ray emitted during the fission process come from the de-excitation of the Giant Dipole Resonance mode (GDR) of the nuclei. The authors of [Pau94] stressed the influence of the dissipation in the increase of the GDR γ-ray emission with respect to the predictions of the statistical model. In this case, the γ-ray emission comes either from pre-scission stage or from the fission fragments. However, contrary to the neutron clock case, pre- and post-scission GDR γ-ray contributions need the support of model calculations to be disentangled.

To extract qualitative results about early transient time using nuclear clocks, pre- and post-saddle contributions have to be disentangled. However, it is impossible to experimentally access to the saddle point information and model calculations are needed [Sax94].

1.2.4. Temperature at the saddle point

The temperature at the saddle point (T_{sad}) is a key parameter in the fission decision. As mentioned before, the modification of the excitation energy (temperature) at the saddle point during the transient time alters the fission probability. Since the experimental measurement of T_{sad} is inaccessible with the present technology, other observables are needed.

The expression of the width of the mass A of the fission fragment distribution (σ_A) as a function of the temperature at the saddle point [Fon69; Arm70] is:

$$\sigma_A^2 = A_{fiss}^2 T_{sad}/(16d^2V/d\eta^2) \tag{1.7}$$

where $(16d^2V/d\eta^2)$ is the potential stiffness, $\eta = (4/A_{fiss}/(M - A_{fiss}/2)$ is the mass asymmetry deformation, and A_{fiss} and M are the mass of the fissioning nuclei and the mass of the fragments, respectively. Due to the high probability of neutron evaporation compared to proton emission, the width of the charge distribution of the fission fragments, σ_z, is a more suitable to investigate dissipative and transient effects. The connection between mass and charge distributions is:

$$\sigma_z^2 \approx (Z_{fiss}/A_{fiss})^2 \sigma_A^2 = Z_{fiss}^2 T_{sad}/(16d^2V/d\eta^2) \tag{1.8}$$

Z_{fiss} being the charge of the of the fissioning nuclei. An empirical parametrization of the potential stiffness at the saddle point as a function of the fissility of the nuclei, found by Rusanov and collaborators [Rus97], is used to infer the temperature at the saddle point. A deeper insight into transient effects extrapolated from T_{sad} needs the backup of model calculations, as we will see in the next section.

1.3. Experimental technique of the present work

In this section, the experimental method used in the present work will be described, as well as the pertinent tools to extract information about dissipative and transient effects. The reaction mechanism used to induce fission and the signatures sensitive to dissipation are introduced, and, in the last point the nuclear-reaction codes utilized in this work are presented.

1.3.1. Spallation and fragmentation reactions in inverse kinematics at high excitation energies

There exist several mechanisms to excite nuclei and induce fission. The excitation energy, angular momentum and shape of the created fissioning nuclei is determined by the reaction mechanism. According to the work of Grangé and collaborators [Gra83], the ideal conditions to observe transient effects require high excitation energy, low angular momentum and the nucleus in the deformation ground-state.

Fissioning systems can be created in the nucleus-nucleus collisions at low energies (less than 100 A MeV). It is the so called fusion-fission reactions which is the most used mechanism to probe dissipation effects. The compound nuclei or fissioning nuclei formed in this kind of reactions have a well-defined mass and charge, and, a broad angular momentum distribution. The excitation energies acquired by the fissioning nuclei are less than 120 MeV. This fact complicates the manifestation of pre-saddle dynamical times since an excitation energy threshold is needed (140 MeV) [Tho93; Mor95]. Most part of the fusion-induced fission experiments used atomic and nuclear clocks measuring pre-scission neutrons, light-charged particles and GDR γ-ray multiplicities. Owing to the high angular momentum induced the fissioning system, this may have a considerable deformation and the transient delay is therefore reduced. If the fission is induced by nucleon-transfer reaction the situation is similar to that of the fusion-fission reaction with even lesser excitation energies (below 80 MeV). In this case the number of highly fissile systems is even more limited.

Fragmentation induced by heavy ions and spallation reactions at relativistic energies also fulfill the ideal conditions established by Grangé for the manifestation of transient regimes [Ye12]. These reactions can be divided in two stages with different time scales [Ser47]. The first stage consists of the fast interaction between the projectile and the target in which the composition of the system is modified and high excitation energy is induced in it. Initially, due to the fast interaction between the projectile and the target, a highly excited compound nucleus is well formed with a narrow shape distribution and with collective degrees of freedom out of equilibrium. During the second stage, the thermalization and de-excitation of the system occurs through evaporation of neutrons, light-charged particles, intermediate mass fragments (IMF), γ-ray and fission.

Benlliure and collaborators [Ben02] investigated dissipative effects in spallation reactions at relativistic energies in inverse kinematics. In this experiment, performed at FRS (FRagment Separator [Gei92]) at GSI (Darmstadt - Germany), highly excited nuclei with an average angular momentum of $10\hbar$ [Jon97], were created in peripheral collisions of a ^{197}Au beam impinging on a proton target at relativistic energies. The schematic view is represented in Fig. 1.3. Focusing on the fission channel, the reaction was reconstructed with the velocity, charge and mass of one fragment. The key observables sensitive to dissipation used in this work were the total fission cross section and the width of the charge distribution of the fission fragment (σ_Z). From Eq. 1.2.4, the temperature at the saddle T_{sad} point was inferred , and, a mean excitation energy above the saddle of around 110 ± 20 MeV was calculated considering $E^*_{saddle} = a_f T^2_{saddle}$, where a_f is the level-density parameter calculated according Ignatyuk *et al.* [Ign75]. Taking into account a contribution of the fission barrier B_f of around 18 MeV, the excitation energy of the nucleus at the the saddle amounted to 128 MeV. A transient time of $(3 \pm 1) \times 10^{-21}$ was calculated comparing the experimental results with ABRABLA nuclear-reaction code [Gai91; Kel09] and considering a step-function function to evaluate the time-dependent fission decay width $\Gamma(t)$.

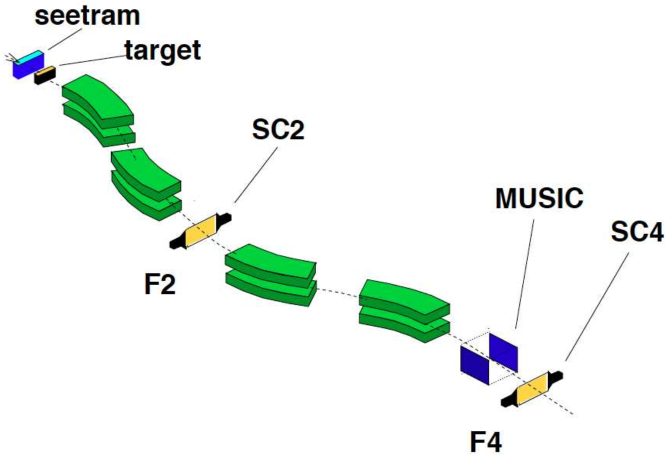

Figure 1.3: Sketch of the FRagment Separator and the experimental setup used in [Ben01]. The fission fragments produced in the target are identified in mass and charge (MUSIC ionization chamber placed at the end). The kinetic energies of the fragments are measured via Time-of-Flight between SC2 and SC4.

Based on these ideas, a new experimental approach was proposed by Jurado *et al.* [Jur04] to deduce a value of the transient time through peripheral relativistic heavy-ion collisions. An innovative fission setup in inverse kinematics [Sch00] with high acceptance and efficiency, placed behind the FRS, was used to make a complete reconstruction of the reaction (see Fig. 1.4 for a schematic view). Previous experiments performed at the FRS in inverse kinematics, measured the mass and charge of fission residues with high precision, in addition to the fission cross sections [FD05; Ben02; Ber03; Enq01; Per07]. However, the transmission of the fission fragments was limited by the acceptance of the spectrometer, and only one fission fragment was measured. In this innovative experimental setup, owing to the kinematics of the reaction, both fission fragments were emitted in the forward direction with large kinetic energies and detected in-flight simultaneously . The charge of both fission fragments allowed to reconstruct the charge of the fissioning nuclei, $Z_1 + Z_2$, and select each fission event according to the excitation energy induced in the collision and its impact parameter. For low impact parameters, high excitation energies are induced in the fissioning system, more nucleons are removed, hence, the value of $Z_1 + Z_2$ decreases.

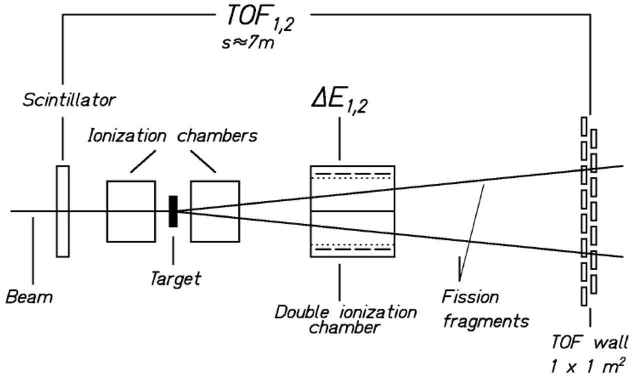

Figure 1.4: Dedicated setup for fission studies in inverse kinematics placed behind the FRS. Both fission fragments are identified in-flight simultaneously. The figure was extracted from [Jur04]

Two new signatures sensitive to transient effects were extracted. The partial fission cross sections for each fissioning system $Z_1 + Z_2$ with high excitation energies revealed a suppression of the fission channel because evaporation decay times are faster than the transient time during which the fission decay is completely inhibited. This signature proved to be more sensitive to these effects than the total fission cross section since the events were selected according to its excitation energy. Another signature exploited in Jurado's work was that of the width of the charge distribution of the fission fragments σ_Z as a function of $Z_1 + Z_2$. This allowed to measure the temperature at the saddle point which increases with decrease of $Z_1 + Z_2$. At higher excitation energies transient and dissipative effects lower the temperature at the saddle point, and therefore, the width of the charge distribution. The results were compared with a modified version of the ABRABLA code including an analytical solution of the FPE [Jur03; Jur05] in order to extract conclusions on transient effects. In this case, a transient delay of $(1.7 \pm 0.4) \times 10^{-21}$ was calculated. These signatures were also exploited in several systems, with different fissilities, created by fragmentation of spherical radioactive heavy nuclei using a similar setup [Sch10].

In the present work, two different experimental schemes based on the experimental setup utilized in [Sch00] were used to measure the proton-induced fission of ^{181}Ta, and, proton- and deuteron-induced fission of ^{208}Pb. For ^{181}Ta+p the total fission cross section was measured at different relativistic energies (0.3, 0.5, 0.8 and 1 A GeV). This allowed to investigate the fission probability in a wide range of excitation energy. In the ^{208}Pb case, fission was induced at 500 A MeV using two different targets (proton and deuteron) to explore two different ranges of excitation energy. In addition, the nuclear charge of both fission fragments were unambiguously determined, and following the work of Jurado *et al.*, the charge of the fissioning nuclei ($Z_1 + Z_2$) is reconstructed to discriminate each event according to its excitation energy. Therefore, the excitation energy is modified either by changing the target or varying the Z_1+Z_2 range. Since ^{181}Pb is a doubly magic and spherical nuclei, its fission induced by spallation at relativistic energies represents a favorable scenario to investigate the dissipative and pre-saddle transient effects using the above-mentioned signatures. Specific details about the detectors used in the setup will be explained in the corresponding chapters.

1.3.2. Nuclear-reaction codes

In this section, a short description of the available codes to model the fission process at intermediate and high energies are presented. The use of these reactions codes to extrapolate quantitative results about pre-saddle transient times are compulsory since the direct experimental measurement is technologically impossible. Following the idea of two-stage process, calculations are made using a code describing the first fast interaction stage coupled to a de-excitation code.

For the first stage two different INC (Intranuclear-cascade) models are used: INCL (Liège) [Bou02] and ISABEL [Yar79]. The former is applied to reactions between light projectiles (pions, light nuclei and nucleons) and heavy targets. The particle of the target are moving along straight trajectories inside a potential well and the evolution of the projectile is described as a succession of binary collisions between the particles along a complete cascade event. It includes also a detailed description of Δ resonances. It is also worth pointing out the fact that INCL parameters are not adjusted but taken from optical model phenomenology. The ISABEL model describes reactions between heavy-ions within relativistic classical mechanics frame. In this time-like intra-nuclear cascade model model, both the projectile and target particles are inside a potential well and are treated as a continuous medium or Fermi sea which is perturbed by the collisions provoked by the cascade particles. The interaction between particles inside the same Fermi sea are not considered. The description of the first stage also can be done using ABRA code which is included in ABRABLA. ABRA was originally developed to describe nucleus-nucleus collisions and it was extended to include also nucleon-nucleus collisions including a model (BURST) based on the parameterizations made according to INCL results.

The description of the de-excitation stage is made either according to Weisskopf-Ewing or Hauser-Feshbach [Hau52] formalisms. In the ABLA code the de-excitation by particle emission is described according to Weisskopf-Ewing formalism as a competition between fission and other decay channels (namely emission of neutrons, γ-rays, light charged particles and intermediate mass fragments (IMF)). The fission decay channel includes a dynamical description based on an analytical solution of the FPE [Jur05]. Hence, ABLA includes a realistic picture of the nuclear dissipation effects in the fission process. In such codes, a critical parameter is that of the level-density parameter which is calculated in ABLA according to [Ign75]. Fission barriers are calculated from the finite-range liquid-drop model of Sierk [Sie86]. The influence of the angular momentum on the fission barrier is also considered.

On the other hand, GEMINI++ is also used to describe the de-excitation process. This model was originally developed to address complex-fragment emission in heavy-ion fusion experiments. Here, the decay of the compound nucleus is described as a succession of binary decays until the competition with γ-ray emission makes the particle emission improbable because of the energy of the system. The evaporation of light-charged particles is described by the Hauser-Feshbach formalism which includes a more specific angular momentum treatment. The production of IMF and heavier fragments via binary decay is ruled by Moretto [Mor75] formalism. The main difference with ABLA lies in the treatment of the fission decay. In this case, the fission width is predicted using Bohr-Wheeler formalism and Sierk's model for the fission barriers, and therefore, GEMINI++ does not include any description about dissipative and transient effects, and, the basic parameters have to be adjusted to reproduce the experimental data.

Chapter 2

Proton-induced fission of ^{181}Ta at relativistic energies

Spallation reactions induced by relativistic protons on ^{181}Ta lead to excited target remnants with large fission barriers (20-25 MeV) covering a broad range in excitation energy. The investigation of the fission process under these extreme conditions is expected to provide relevant information on the dynamics of fission at high excitation energies. On the other hand, tantalum and tungsten alloys are proposed as optimum materials for the construction of spallation neutron sources because of their properties under extreme irradiation conditions: relatively large neutron production, corrosion resistance, and a high melting point. Spallation targets are of interest in different domains. One of the technologies which relies on spallation reactions is that of accelerator-driven systems, ADS [Nif01], which are currently under study as an option for nuclear waste incineration. Recently the construction of the ESS (European Spallation Source) [Cla03] facility has been approved and different research communities are awaiting its opening to undertake a wide range of experimental programs in material science, biology and other scientific disciplines. Tantalum targets are also used for the production of exotic nuclei at ISOL-type [ISO] facilities and neutrinos [Bur96].

Fission may have a significant effect on the performance of a spallation target. Therefore, a good knowledge of the interaction of protons (commonly used as spallation sources drivers) with these materials is mandatory for their characterization. Reactions leading to fission are of interest because they contribute to the production of hazardous remnants, in particular gaseous ones, such as the isotopes of Kr and Xe. The composition of that radioactive inventory, its evolution, the influence of these changes to the target performance itself and its structural damages can be estimated with state-of-the-art models. However, only through an evaluation of numerical calculations with accurate data it is possible to validate these models and improve their reliability for use in technical applications.

Unfortunately, presently available data related to total fission cross sections of ^{181}Ta above 700 MeV proton-beam energy are scarce and show clear discrepancies at 1000 MeV [Yur05; Boc78]. The situation does not improve at lower energies, where the available data are more abundant, but they also present inconsistent results [Bar62; Kon66; Shi73; Mau65], in particular between 300 and 500 MeV. Most of these experiments were performed using passive track detectors and only few of them are based on coincident measurements of both fission fragments [Ste67]. Under such conditions it seems difficult to unambiguously identify a fission channel with a few mb cross section as is expected in this case. All previous measurements of fission reactions induced by protons on ^{181}Ta were performed using the direct kinematics technique. Therefore, the reaction products have a very low kinetic energy, preventing their escape from the target. To overcome this difficulty the detection scheme presented in 1.3 was utilized.

This chapter is dedicated to the analysis of the fission cross section of ^{181}Ta+p at 300, 500, 800 and 1000 A MeV. The experimental setup and the main aspects of the detectors utilized in this work are presented. We implemented a method to recognize fission events and calculate the fission yields normalized to the number of projectiles. Then, fission cross sections and their uncertainties were determined with high accuracy. In the last part of this chapter, we compared the results with previous measurements and systematics found in the literature and with calculations based on state-of-the-art models describing the fission process.

2.1. Description of the experimental setup

In the present experiment, the ^{181}Ta nuclei were accelerated using the basic installation of GSI, the UNILAC linear accelerator and the SIS-18 synchrotron, up to 300, 500, 800 and 1000 A MeV with an intensity of the order of 10^4 ions/s and a spill duration of 7 s. The beams were guided to a dedicated experimental setup (shown in Fig. 2.1) where impinged onto a liquid hydrogen target surrounded by two Multi-sampling ionization chambers (MUSIC), used to identify the reactions of the beam particles with any layer of matter placed in the setup. A Multi-wire chamber (MW) and a veto scintillator were used to collimate the beam and determine its position. Due to the kinematics of the reaction, we were able to detect efficiently both fission fragments which were emitted in the forward direction with large kinetic energies. A double paddle scintillator was used for this purpose. This capability enabled the use of relatively thick targets, increasing the statistics. The beam dose was measured using a scintillator placed upstream of the first MUSIC.

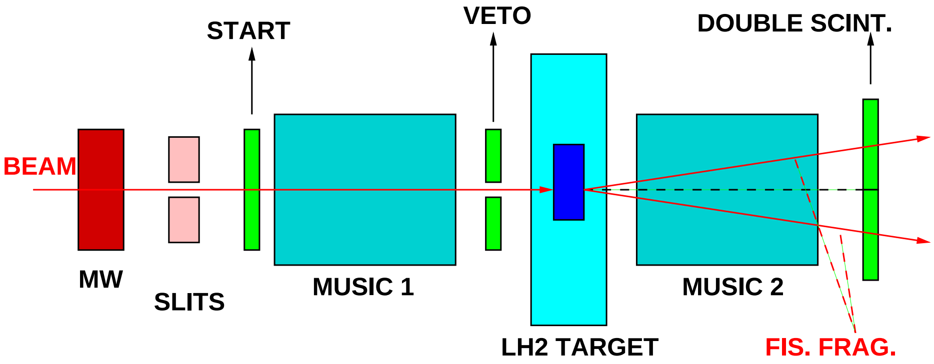

Figure 2.1: Schematic representation of the experimental setup used in the present experiment.

Multi-wire chambers A Multi-wire chamber (MW) [Ste91] and thick iron slits were used to collimate the ^{181}Ta beam at the target. These MW consists of five parallel wire planes with different voltages. The anode plane is made of tungsten wire of 20 μm with 2 mm pitch while the cathode electrodes have 50 μm wires separated by 1 mm. The latter define the X and Y orthogonal directions. The spacing between anode and cathode planes is 5 mm. The chamber operates with a gas mixture (Ar and CO_2) at atmospheric pressure.

Scintillators A first scintillator detector (start) placed upstream of the target, determined the beam flux. This detector consists of a BC420 3 mm thick plastic scintillator coupled to two R2083 Hamamatsu photomultiplier allowing a double lecture from both sides (left and right). With this double lecture we determined the position of the beam at the exit of the FRS (S4). Another similar scintillator detector was placed in the second plane S2. A ^{181}Ta ion that reacted in any layer of the spectrometer, losing neutrons or capturing electrons, arrived at different positions in S2 and S4. By combining the positions measured in both focal planes, the contaminants were identified and rejected.

A veto scintillator with a 15 mm diameter hole placed just before the target allowed the rejection of beam-halo particles and misaligned beam trajectories. The two fission fragments were detected independently, but in temporal coincidence, by a double paddle made of two BC420 scintillators (up and down read out) placed downstream of the target (300 mm x 70 mm and 3 mm thickness each paddle separated by a 1 mm gap).

The signals coming from the photomultipliers were discriminated using constant fraction discriminators (CFD) and then sent to a time-to-amplitude converter (TAC) which signal was digitized by a CAEN V785 analog-to-digital converter (ADC). The signals were also sent to a CAEN V792 charge-to-digital converter (QDC) to register the charge of the pulses.

Target The proton target consisted of a liquid hydrogen cell of about 1 cm thick and 3 cm diameter (85 mg/cm^2), isolated by a titanium foil and five layers of Al-coated mylar strips. The cell was introduced inside a container at high vacuum with 100 μm titanium windows for protecting the beam line vacuum in case of rupture of the cell, and a cryostat for liquefying the hydrogen was used to establish a pressure and temperature of around 1 atm and 20 K, respectively.

Multi-sampling ionization chambers The target was surrounded by two Multi-sampling Ionization Chambers (MUSIC80) [Pfü94] having an active area of 200 mm x 80 mm and 460 mm of active length filled with CF_4 (see Fig. 2.7). The windows of the chambers were made of float glass and aluminum-coated mylar. A voltage of 8000 V was applied between the eight anodes and the cathode to create an uniform electric field. A Frisch-grid at 0 V was placed near the anodes to restrict the position dependence of the induced signals. The electrons, released in the ionization of the medium by an ion crossing the chamber, were forced to drift to the anodes. The induced signals were registered by charge-sensitive amplifier that converted the charge into amplitude signal. These amplitude signal were digitized by a CAEN V785 ADC. Therefore, both chambers measured the energy loss of the tantalum beam particles and that of the products of the reaction, respectively. These ionization chambers, having almost 100 % efficiency for the detection of relativistic heavy nuclei and high rate capability (40 kHz), were used to identify reactions of ^{181}Ta produced in the hydrogen target and in any other layer of matter present in the beam line.

Data acquisition The pulses were digitized using standard VME electronic modules. The control of the VME bus was done with the CES RIO3 processor. The data read out of the VME modules was managed by the multi-branch system (MBS) develop at GSI [MBS]. This data was read out and sent to an event builder for each accepted trigger. According to the setup geometry, two different triggers were used for data acquisition: The “beam” trigger was provided by the plastic scintillator placed upstream of the target in anti-coincidence with the signal of the veto scintillator. The "reaction" trigger was produced by the coincidence between the "beam" trigger and the time-coincident signals on both paddles of the double scintillator placed downstream the target. These two triggers provided the measurement of the beam flux together with the fission events. The average rates for the "beam" and "reaction" triggers were around 10^4 and 700 triggers/s, respectively. We used CAEN V820a scalers to count the number of "beam" and "reaction" triggers .The "beam" trigger was downscaled to reduce the data acquisition dead time.

2.2. Determination of the fission cross sections

2.2.1. Identification of the fission events

The identification of the fission events was based on the amplitude of the signals recorded by the two MUSIC chambers surrounding the target and the amplitude of the signals provided by the two paddles of the double plastic scintillators located downstream of the target. With this information, we were able to isolate fission events from other reactions channels occurring in the hydrogen target.

In Fig. 2.2 a scatter plot of the energy losses of ions traversing the two MUSICs, before and after the target, is depicted using the "reaction" trigger. The events lying in the diagonal of this plot correspond to ions which kept their atomic number when passing through the target. These nuclei, lighter than the primary beam, have been produced in nuclear reactions induced by ^{181}Ta projectiles in any layer of matter situated upstream of the hydrogen target. The dominant ^{181}Ta spot of non-interacting beam particles is clearly visible at the top, near channel 3800 on the vertical axis. The vertical group below the beam spot corresponds to residual fragments produced in the interaction of ^{181}Ta with hydrogen. In this group, events inducing high and small energy loss signals, correspond to residual heavy nuclei and emitted light nuclei from evaporation processes.

Since the energy loss of nuclei is proportional to their atomic number squared (Z^2), fission fragments are expected to produce energy loss signals corresponding to about half of the value obtained for the primary beam ($\Delta E_{f.f.} \propto Z_1^2 + Z_2^2 = Z_{beam}^2/2$). Therefore, fission products should be located around channel 1800 on the MUSIC 2 energy loss axis. To count for the fission events, n_{fiss}, a condition in the scatter plot shown in Fig. 2.2 was applied

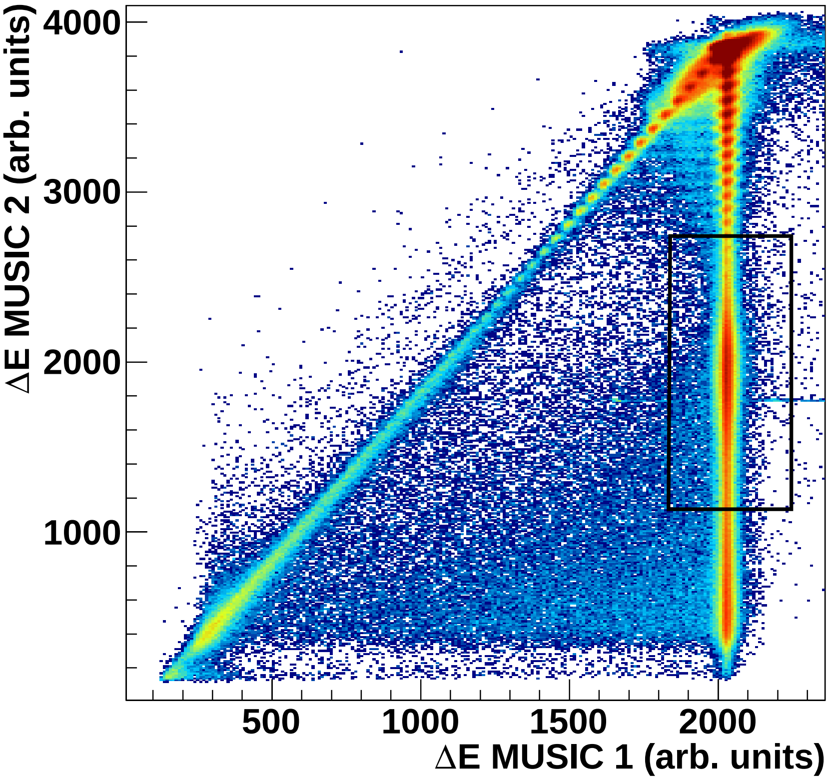

Figure 2.2: Scatter plot of the amplitudes of the signals registered with the two MUSIC detectors. Nuclei lighter than ^{181}Ta produced in reactions before MUSIC 1 appear in the diagonal region. In the vertical line the ^{181}Ta spot corresponding to non-interacting beam particles is represented, and below the events corresponding to reactions in the target. The box encloses the fission region and the color code represents counts on the logarithmic scale.

selecting the region where the fission products are expected. Focusing on the selected region, indicated by the rectangular area in Fig. 2.2, the fission events were identified combining the amplitude (energy loss) of the signals recorded by the two paddles of the double plastic scintillator.

In Fig. 2.3 the amplitudes of the signals registered by both plastic scintillators in temporal coincidence (at 1 A GeV and 300 A MeV in the left and right panels, respectively), using the “reaction” trigger, are represented in a scatter plot. Due to the charge splitting of the fission process, fission events

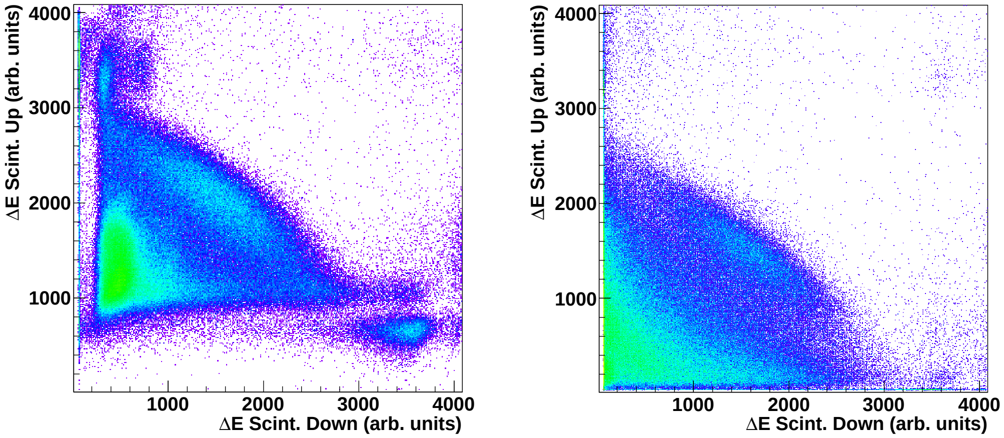

Figure 2.3: Scatter plot of the energy loss signals provided by the two paddles of the double plastic scintillator placed downstream the target with the reaction trigger (Upper panel 1 A GeV Full target - Lower panel 300 A MeV Full target). Both plots are normalized to the same number of counts to highlight the influence of different reaction channels. The color code represents counts on the logarithmic scale.

are expected to populate the diagonal band in this figure, and are separated from other much more abundant reaction channels. This fission region only represents a small part of the plot statistics since the fission probability is rather small. For this reason, fission events could only be properly identified by a detection setup enabling the identification of different reaction channels.

In order to provide an accurate measurement of the fission cross section, we evaluated the background which remains in the fission region due to simultaneous break-up and evaporation processes. To evaluate this background we used Fig. 2.4, where the energy loss provided by the two paddles of the double plastic scintillator at 1000 A MeV is represented by selecting only events compatible with a fission signal in the MUSIC detectors (rectangular area in Fig. 2.2).

In this figure, intermediate mass fragments (IMFs) produced in simultaneous break-up reactions may populate the fission region (dotted contour in Fig. 2.4). The evaluation of this break-up background was performed via dividing the fission region into slices as shown by the thin rectangles in Fig. 2.4. Each slice was then projected along its longitudinal dimension (insets in Fig. 2.4), which clearly enhanced the profile of the contributions coming from background (left peak) and fission (right peak). Gaussian fits to each of the two contributions defined the correction for the break-up background suppression. On the other hand, evaporation residues could also populate the edges of the fission region along an axis $\Delta E_1+\Delta E_2$ (dashed line in Fig. 2.4) defined by the sum of the signals of the two scintillators. To overcome this problem, the region profile (dotted contour in Fig. 2.4) was projected onto this $\Delta E_1+\Delta E_2$ axis to evaluate this contribution by means of gaussian fits as shown in Fig. 2.5.

The number of measured fission events n_{fiss} corresponds then to the number of events in the fission region corrected by the overlapped simultaneous break-up and evaporation background contributions.

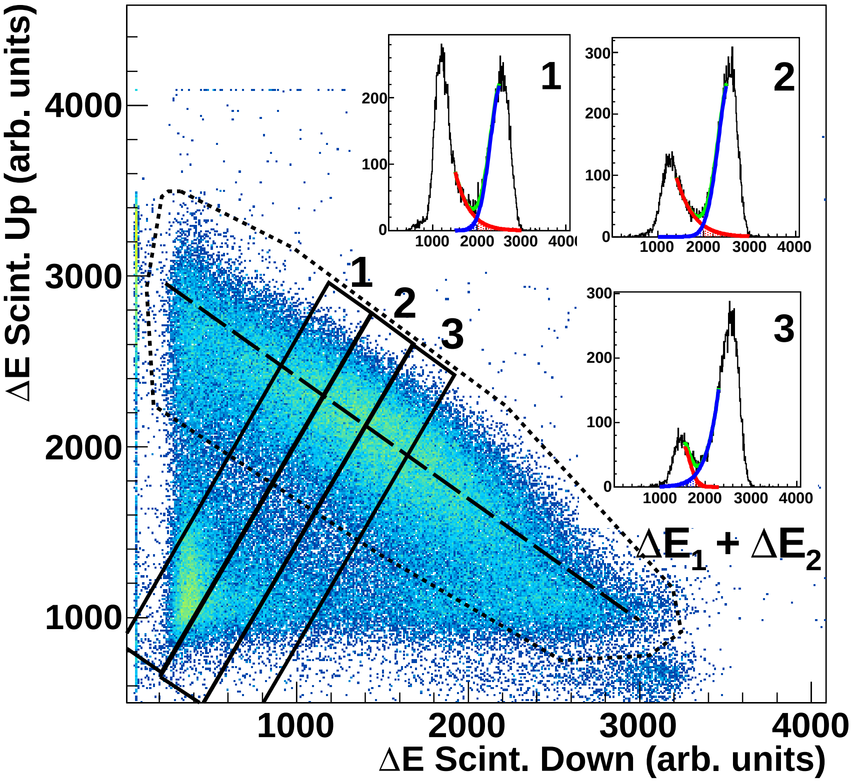

Figure 2.4: Same as the upper panel in Fig. 2.3 but conditioned by the fission selection from Fig 2.2. The different contours and insets illustrate the background suppression method used to identify fission events as explained in the text.

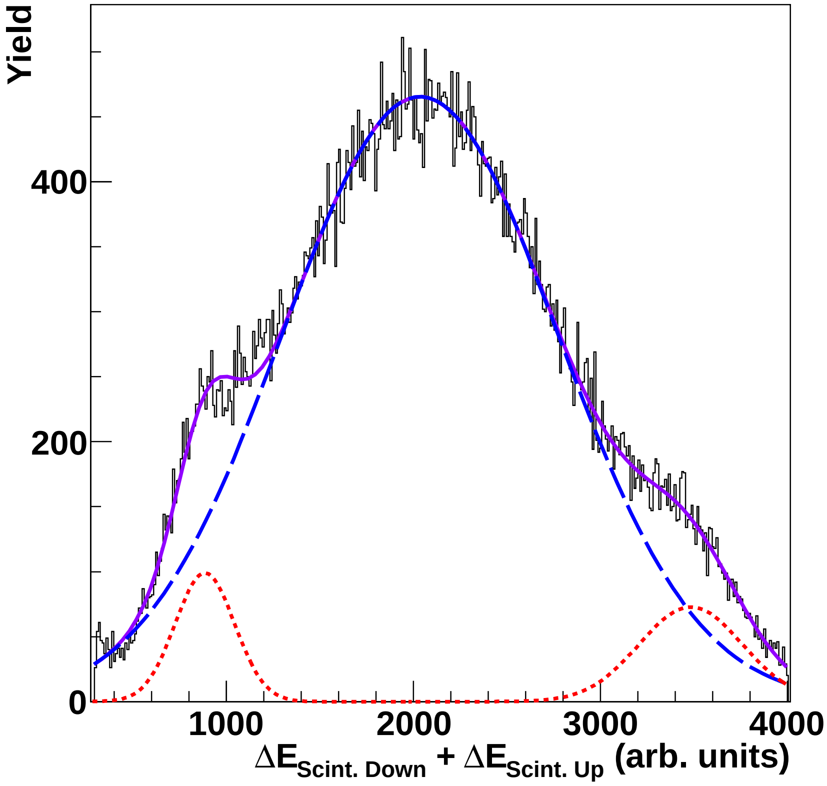

Figure 2.5: Projection of the fission region defined in Fig. 2.4 on the ΔE_1+ΔE_2 *axis represented in the same figure. The contribution of evaporation residues was evaluated by means of a gaussian fit (dotted line) and subtracted from the total contribution (dashed line).*

2.2.2. Fission yields and cross sections

Fission yields (Y_{fiss}) were obtained from fission event measurements corrected by the background (n_{fiss}) and additional effects such as the secondary reactions of the fragments in the target (f_d) and the geometrical acceptance of the experimental setup (f_{geo}), according to the following equation:

$$Y_{fiss} = n_{fiss} \cdot f_d \cdot f_{geo} \tag{2.1}$$

Secondary reactions of the fission fragments in the target were evaluated using the Karol's microscopic model [Kar75]. The number of reactions ε_d

amounted to less than 2.5 % for full target and less than 0.5 % for empty target measurements at 1000 A MeV. The correction factor was determined according to $f_d = 1/(1 - \varepsilon_d)$.

Geometrical constraints were also considered to evaluate the efficiency of the detection setup. Fission products emitted close to the double paddle scintillator gap had a probability of passing through it or through the same paddle. A Monte Carlo calculation of the post-scission kinetic energy of the fission fragments [Wil76] was performed to evaluate the ratio of fission product losses due to the geometry of the setup. The kinetic energies of the fission fragments can be calculated with the following equation:

$$TKE = \frac{Z_1 Z_2 e^2}{d} \tag{2.2}$$

where Z_1 and Z_2 are the nuclear-charges of the fission fragments. D is the distance between their respective centers at the scission point which is calculated using the following expression:

$$D = r_0 A_1^{1/3} \left(1 + \frac{2}{3}\beta_1\right) + r_0 A_2^{1/3} \left(1 + \frac{2}{3}\beta_2\right) + d \tag{2.3}$$

A_1 and A_2 being the masses of the fission fragments, β_1 and β_2 the deformation coefficients, $r_0 = 1.16\ fm$ and $d = 2\ fm$. Using equations 2.2 and 2.3. We calculated the velocity of the fragments in the center of mass frame and then a Lorentz boost in the beam direction was applied to transform the velocities into the laboratory frame. Taking into account the dispersion of the beam as measured with the Multi-wire chamber detector, the velocities of the fragments, and, the alignment and the distance from the centre of the hydrogen target to the double plastic scintillator, we calculated the perpendicular dimensions of the fission fragments distribution in the double plastic scintillator detection plane (see Fig. 2.6). The acceptance of these scintillators (300 mm x 140 mm and 1 mm gap) allowed us to evaluate the losses, by counting the number of fragments lost in the gap, and estimate the geometrical efficiency of the double paddle scintillator ε_{geo} having a value smaller than 10 % at 1000 A MeV and decreasing with the beam energy.. Thus, the resulting yield was corrected by a geometrical factor ($f_{geo} = 1/\varepsilon_{geo}$).

To determine the number of projectiles (n_b), we used the first MUSIC to identify tantalum among other nuclei that have been created in other layers of matter placed in the beam line before the target, as shown in Fig. 2.7. The sum of the $Z = 73$ ions identified according to this procedure using the “beam” and the “reaction” trigger corrected by the downscaling factor provided the total number of projectiles.

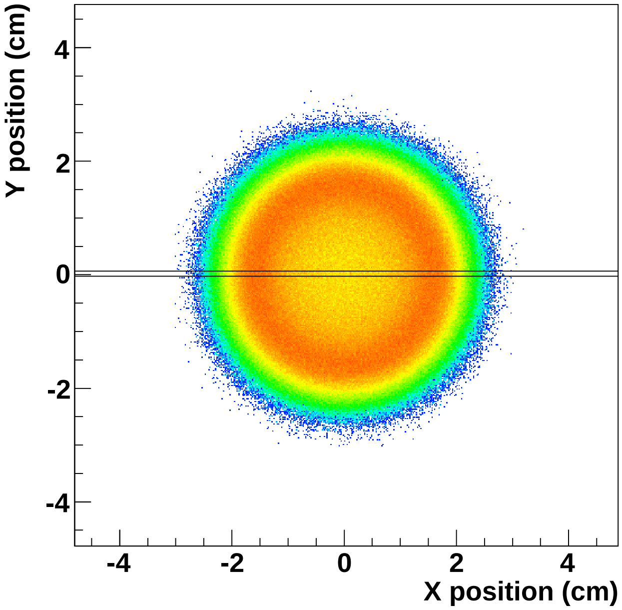

Figure 2.6: Fission fragments spatial distribution in the double plastic scintillator plane. The are between both solid lines represents the size of the gap.

Due to the relatively large thickness of the target, a fraction of projectiles ε_a were attenuated (< 5 % for full target and < 1 % for empty target at 1000 A MeV). Assuming linear decrease of the beam intensity, the mean attenuation corresponds to the value when the beam reaches half the target. Therefore the number of projectiles was corrected by a factor $f_a = 1 - \varepsilon_a$ taking into account the attenuation of the beam intensity along the target. The value of this factor was also evaluated using Karol's model. To correct for reactions taking place in the target windows (namely Ti) which surrounded the liquid hydrogen, fission yields determined with the empty target following the same analysis procedure were subtracted from the fission yield obtained with the full target.

Finally, the respective fission yields were normalized to the number of projectiles and the number of nuclei in the target per unit area (N_t) to determine the total fission cross section according to the following expression (with $N_b = n_b \cdot \mathrm{f}_a$):

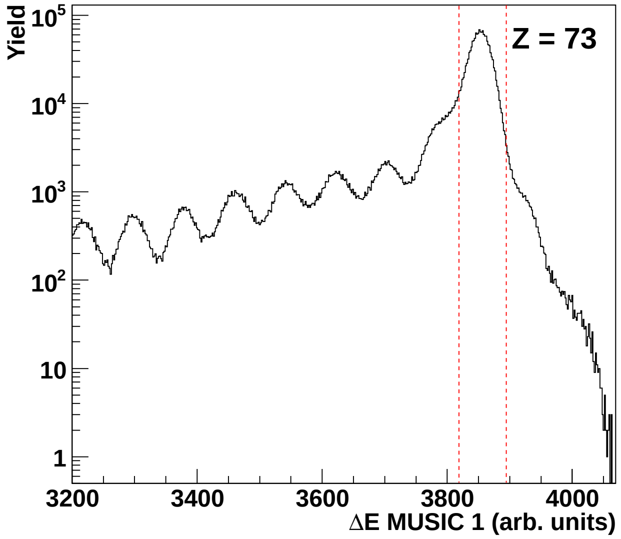

Figure 2.7: Energy Loss signals provided by the MUSIC 1. The region between the dotted red lines corresponds to ^{181}*Ta.*

$$\sigma = \left(\frac{Y_{fiss}^{full}}{N_b^{full}} - \frac{Y_{fiss}^{empty}}{N_b^{empty}} \right) \cdot \frac{1}{N_t} \tag{2.4}$$

The different correction factors and their values are listed in the table 2.1. The independent number of fission with the empty target at 500 A MeV could not be determined. To overcome this problem, the yields normalized to the number of projectiles at 300, 800 and 1000 A MeV for the empty target were fitted to a function based on the fission cross-section parametrization proposed by Fukahori and Pearlstein [Fuk90]:

$$\sigma(E_p) = P_1(1 - exp[-P_3(E_p - P_2)]) \tag{2.5}$$

where E_p is the energy of the projectile, and P_1, P_2 and P_3 are the fit parameters. We extrapolated the value and the uncertainty of the normalized yield at 500 A MeV from this fit (see Fig 2.8).

2.2.3. Uncertainties

Particular attention was paid to the evaluation of the corresponding uncertainties. The main sources of systematic uncertainties were the identifi-

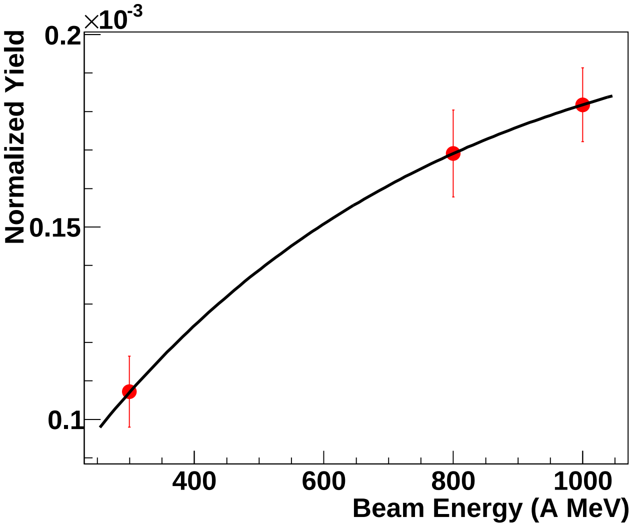

Figure 2.8: Yields normalized to the number of projectiles as a function of the beam energy. The solid line represents the fit to extract the value of the yield at 500 A MeV.

		Full Target		Empty Target	
Energy	ε_{geo}	ε_d	ε_a	ε_d	ε_a
1000 A MeV	91.1%	2.2%	4.1%	0.4%	0.5%
800 A MeV	92.2%	2.2%	4.0%	0.4%	0.5%
500 A MeV	94.1%	2.2%	3.9%	0.4%	0.5%
300 A MeV	95.35%	2.2%	3.8%	0.4%	0.5%

Table 2.1: Geometric efficiency (ε_{geo}), beam attenuation (ε_a) and secondary reactions of the fission fragments (ε_d).

cation of fission events ranging from 2 to 10% ($\epsilon(n_{fiss})$), the beam intensity ($\approx 5\%$) and the target thickness ($\approx 4\%$). The sources of systematic uncertainty for the different correction factors were also evaluated. The systematic uncertainty of the geometrical correction factor (f_{geo}) was estimated to be smaller than 5 %. The evaluation was done by changing the size of the double plastic scintillator gap and the beam profile in our simulation. The value of the systematic uncertainty of the correction factors due to the beam attenuation (f_a) and the secondary reactions of the fission fragments (f_d) were smaller than 1 % and almost the same for all energies. Due to the relatively large number of recorded fission events the statistical uncertainties were below 1.5 %. Statistical and systematic uncertainties, others than the ones associated to the beam intensity and target thickness, for the measurements with the full and empty target are presented in Table 2.2 and Table 2.3.

Energy	$\epsilon_{stat.}$	$\epsilon(\mathrm{n}_{fiss})$	$\epsilon(\mathrm{f}_{geo})$	$\epsilon(\mathrm{f}_a)$	$\epsilon(\mathrm{f}_d)$
1000 A MeV	0.38%	6.01%	4.32%	0.43%	0.22%
800 A MeV	0.39%	7.16%	3.72%	0.41%	0.22%
500 A MeV	0.45%	7.84%	2.80%	0.39%	0.22%
300 A MeV	0.33%	9.51%	2.05%	0.38%	0.22%

Table 2.2: Statistical ($\epsilon_{stat.}$) and systematic uncertainties due to the identification of fission fragments ($\epsilon(n_{fiss})$), geometrical acceptance ($\epsilon(f_{geo})$) and the attenuation correction factors ($\epsilon(f_a)$) of the beam affecting our measurements.

Energy	$\epsilon_{stat.}$	$\epsilon(\mathrm{n}_{fiss})$	$\epsilon(\mathrm{f}_{geo})$	$\epsilon(\mathrm{f}_a)$	$\epsilon(\mathrm{f}_d)$
1000 A MeV	1.45%	1.95%	4.32%	0.05%	0.04%
800 A MeV	1.05%	4.56%	3.72%	0.05%	0.04%
500 A MeV	-	-	2.80%	0.05%	0.04%
300 A MeV	0.96%	7.08%	2.05%	0.05%	0.04%

Table 2.3: Same as table 2.2 but for empty target measurements.

2.3. Results and discussion

Using the method described in the previous sections, we have measured with high precision the total fission cross section of ^{181}Ta induced by protons at 300, 500, 800 and 1000 A MeV. The results obtained for each energy are presented in Table 2.4. The magnitude of the measured cross sections is rather small and strongly decreases for the lower beam energies. The associated uncertainties are also rather small (≈ 10 %) but increase for the lowest energies (≈ 18 %) since the smaller fission cross sections complicates the identification of fission events.

In Fig. 2.9, we present the cross sections obtained in this work as solid points compared to previous measurements by different authors. In this figure, we also present predictions obtained from the systematics established by Prokofiev some years ago [Pro01] (dashed line).

From the analysis of the previously measured cross sections, one can identify some clear discrepancies. At the highest energies, one can find two rather discrepant measurements around 670 MeV by Konshin *et al.* [Kon66] (14.0 ± 1.9 mb) and by Baranovskiy *et al.* [Bar62] (8.0 ± 2.5 mb). At 800 MeV it exists a single measurement by Yurevich *et al.* [Yur05] and at 1000 MeV one finds again two discrepant values obtained by Yurevich *et al.* (15.65 ± 5.4 mb) and Bochagov *et al.* [Boc78] (27.0 ± 1.5 mb). Our results are in very good agreement with the measurement of Yurevich *et al.* at 800 MeV and within the error bars at 1000 MeV, solving the existing discrepancy in this energy range. Moreover, we also confirm the predictions estimated by the systematics of Prokofiev.

Energy (A MeV)	Fiss. cross section (mb)	Stat. uncert. (%)	Syst. uncert. (%)
1000	20.17 ± 2.19	0.46	10.85
800	13.09 ± 1.62	0.32	12.34
500	7.53 ± 1.40	0.51	18.54
300	6.55 ± 1.00	0.48	15.21

Table 2.4: Total fission cross sections determined in this work

In the energy range between 300 and 600 MeV, we can also observe important discrepancies between different measurements. Around 300 MeV the data obtained by Yurevich *et al.* (5.2 ± 1.6 mb) and Konshin *et al.* (2.6 ± 0.4

mb) differ by a factor two. Around 400 MeV, the measurements by Yurevich *et al.* (5.79 ± 1.78 mb) and Konshin *et al.* (4.7 ± 0.7 mb) are in rather good agreement. However, the measurement by Konshin *et al.* is significantly smaller than the one obtained from the systematics of Prokofiev (7.60 mb). The measurement by Yurevich *et al.* could be compatible with the systematics owing to its large uncertainty. Finally, around 500 MeV the measurements by Konshin *et al.* (8.3 ± 1.1 mb) and Yurevich *et al.* (5.59 ± 1.72 mb) also differ by a large factor. Our measurements at 300 and 500 MeV are consistent with the estimated values from the Prokofiev formula, and, confirm the largest values of the cross sections measured in this region.

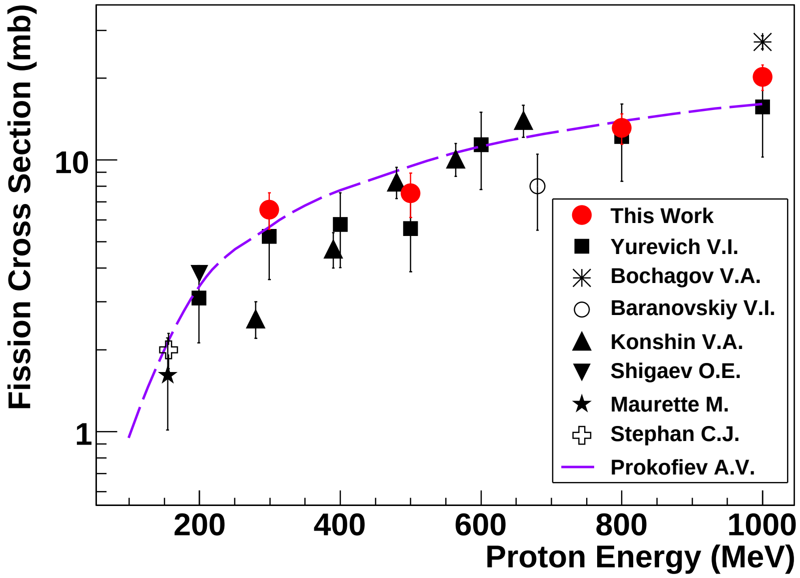

Figure 2.9: Fission cross sections measured in this work (solid circles) in comparison to previously measured data and estimates obtained from the systematics established by Prokofiev (dashed line).

From this analysis we can conclude that our data confirm the measurements by Yurevich *et al.* and the cross sections estimated by the systematics above 700 MeV. At lower energies our measurements clarify the discrepancies existing until now. In the energy range between 300 and 600 MeV, our data favor those measurements presenting the highest cross sections. Moreover our data confirm the predictions obtained by the systematics of Prokofiev over the entire energy range covered by this work.

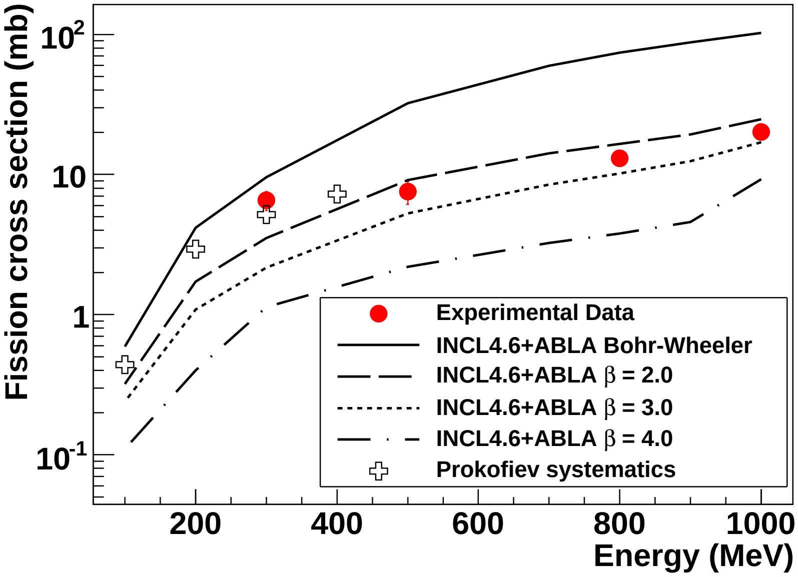

Figure 2.10: Fission cross sections measured in this work (solid circles) in comparison to model calculations using INCL4.6+ABLA for different values of the reduced dissipation coefficient.

2.4. Reaction model benchmarking

A better insight into the fission probabilities of ^{181}Ta can be obtained using reaction codes based on models describing this process. An overview of the features and characteristics of each code utilized in this work is found in Chapter 1.3.2.

Here, we used INCL intra-nuclear cascade code describing the interaction between the projectile and the target couple to a ABLA de-excitation code. The comparison between the experimental data and the calculations for different values of the dissipation coefficient, β, is shown in Fig. 2.10. As can be seen, calculations made according the statistical model (Bohr-Wheeler) clearly overestimate the fission cross sections in the energy range from 500 MeV up to 1000 MeV (solid line). However, a dynamical description of the fission process with a value of β between 2.0 and 3.0 × 10^{21} s^{-1}, dashed and dotted lines, respectively, provides a good description of the data in that energy range although only a rough estimation of the magnitude of the exact value of the dissipation coefficient is given by direct comparison due to the limited sensitivity of the calculations with respect to this factor.

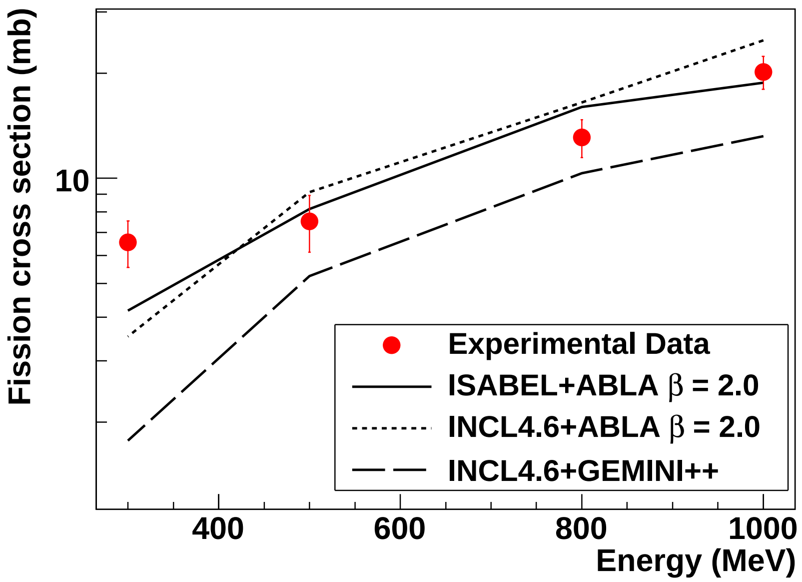

Figure 2.11: Fission cross sections measured in this work (solid circles) in comparison to model calculations using INCL4.6+ABLA and ISABEL+ABLA ($\beta = 2.0 \times 10^{21}$ s^{-1}), and INCL+GEMINI++. The cross sections predicted by the systematics are also included.

The experimental data were also compared with other combinations of codes based in other similar formalisms describing fission reactions induced by protons. We used ISABEL intra-nuclear cascade code and for the evaporation stage we used GEMINI++. The results of calculations performed with ISABEL+ABLA (solid line) and INCL+GEMINI++ (dashed line) and previous calculations made with INCL+ABLA (dotted line) are shown in Fig. 2.11. Both cascades coupled to ABLA predict similar total fission cross sections in the entire range and both present a good agreement with the experimental data, being calculations performed with ISABEL more accurate. Calculations with INCL+GEMINI++ yield lower values of the fission cross section. It is worth mentioning that for the lowest energies (below 300 MeV), the model predictions underestimate the experimental values measured in this work and the ones obtained according to Prokofiev systematics. Thus, dynamical effects, which do not manifest at those energies, are too strong in the model calculations.

In order to better understand the predictive power of these models, we used them to obtain the mass and charge yields of the prefragment (the resid-

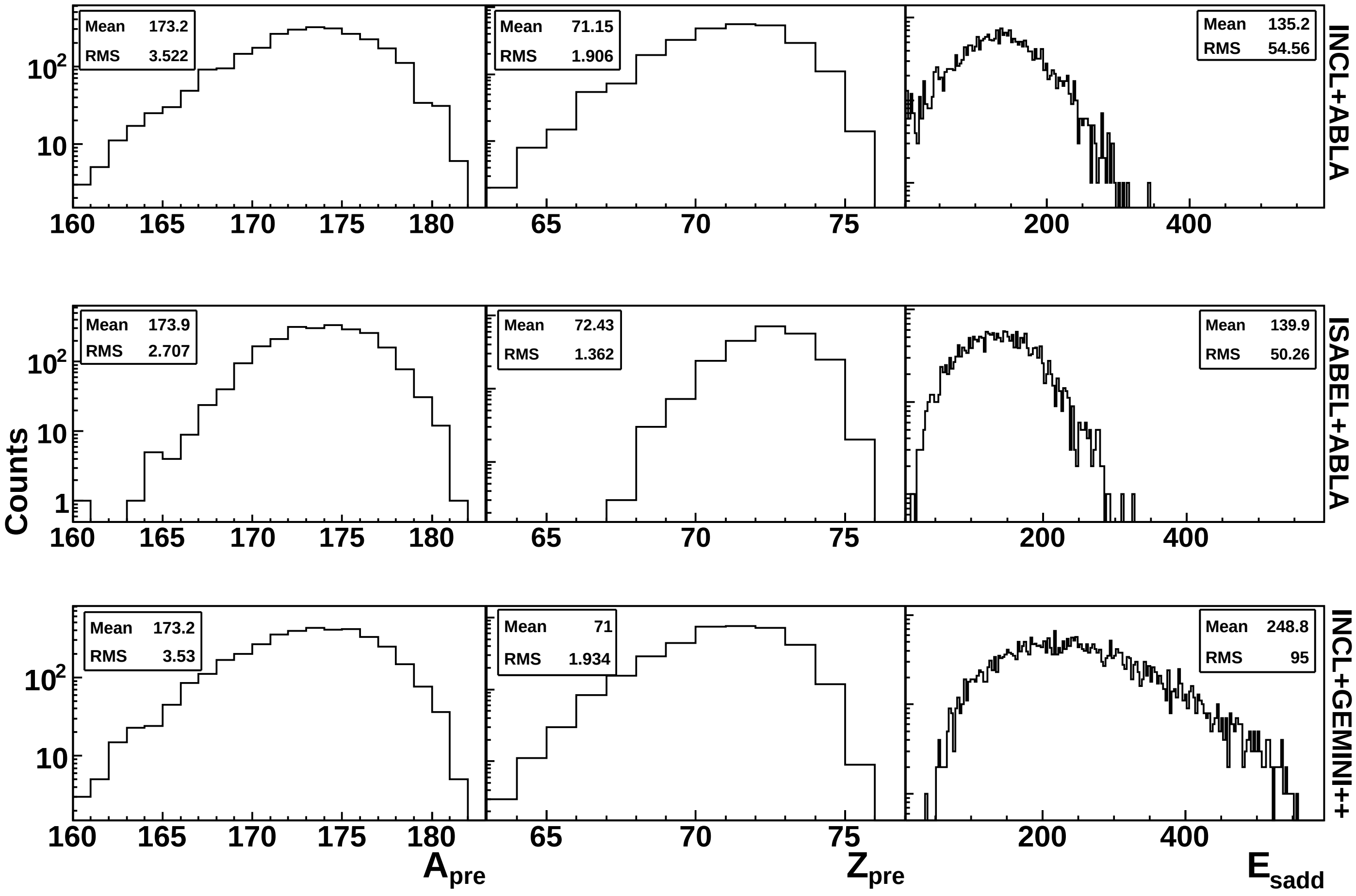

Figure 2.12: Mass and charge yields of the prefragment of a fissioning system created in the reaction ^{181}*Ta+p at 1 A GeV, and, saddle point excitation energy distributions predicted by INCL4.6+GEMINI++, and, INCL4.6+ABLA and INCL4.6+ABLA considering* $\beta = 2.0 \times 10^{21}\ s^{-1}$.

ual nucleus created after the collision), as well as, its excitation energy at the saddle point, as shown in Fig. 2.12. These results allow us to determine the difference in the value of the fission cross section between calculations performed with INCL+ABLA and INCL+GEMINI++ which can be explained in terms of excitation energy at the saddle point. Since the latter is calculated during the de-excitation stage, the main difference between both calculations lies in how GEMINI++ and ABLA treat the fission channel. To obtain a clear comparison between the results given by the codes shown in Fig. 2.12, we plotted the mean and the RMS of the distributions as a function of the proton projectile energy in Fig. 2.13 and Fig. 2.14, respectively. As can be seen, the mean value of the excitation energy distribution and its RMS calculated with INCL+GEMINI++ (dashed line) are both around a factor two larger compared to the ones calculated with INCL+ABLA (dotted line) and ISABEL+ABLA (solid line), which means that in the case of GEMINI++, the prefragment needs a larger excitation energy to undergo fission, and thus, the fission probability is reduced.

On the other hand, one can see also a clear difference between both intranuclear cascades utilized here. Despite calculations done with INCL and ISABEL both coupled to ABLA yield consistent values of the fission cross section and similar excitation energy distributions, there exist a discrepancy in the mean value and RMS of the mass and charge distributions of the prefragment calculated with both codes, as shown in Fig. 2.13 and Fig. 2.14. Predictions made using ISABEL+ABLA (solid line) show narrower distributions (lower values of the RMS) slightly shifted to higher mean values of Z. This difference underlies on the angular momentum induced in the prefragment during the cascade stage. According to the distributions shown in Fig. 2.15, calculations performed with INCL at 1 GeV have slightly larger values of angular momentum which increases the fission probability of the system with respect to the ones calculated with ISABEL. This fact explains the difference between both values calculated at that energy.

From the theoretical stand point, one can find several differences between the description of the fission process included in ABLA and GEMINI++. While the former predicts a reduction of the fission width due to the transient time and nuclear friction established by Kramers, the latter reproduces this reduction by changing the height of the fission barriers given by Sierk. In addition, GEMINI++ does not consider the fission delay due to the transient time of the fission process included in ABLA which hinders the fission probability. Thus, in GEMINI++, an increase of the ratio of level-density parameters in the saddle point and ground-state configurations up to a_f/a_n=1.036 accounts for this reduction [Man10]. It is worth pointing out that the calculations using ABLA were done using a a_f/a_n factor cal-

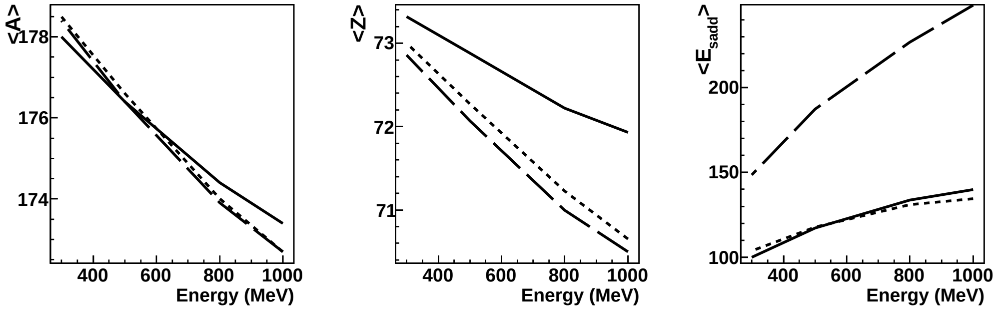

Figure 2.13: Mean value of the mass, charge of the prefragment and excitation energy at the saddle point for the reaction ^{181}*Ta+p as a function of the beam energy calculated with INCL+ABLA (dotted line) and ISABEL+ABLA (solid line) considering* $\beta = 2.0 \times 10^{21}\ s^{-1}$*, and INCL+GEMINI++ (dashed line).*

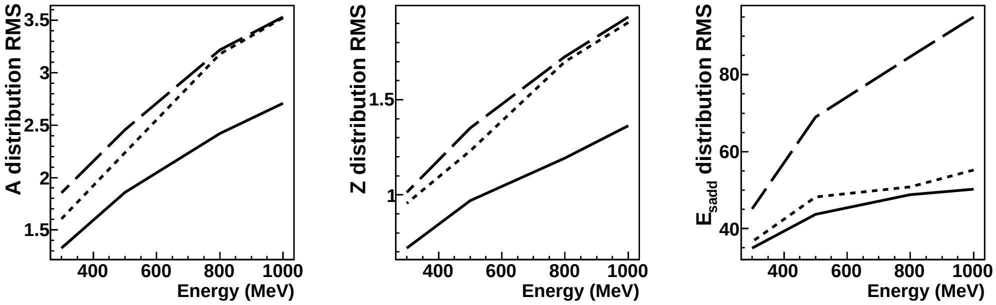

Figure 2.14: Same as fig. 2.13 but for the RMS of the distributions.

culated according to the parameterization found in the Ref. [Ign75], and, a strength of the dissipation coefficient which value may vary in a range between 2 and 3 × 10^{21} s^{-1}. In conclusion, ABLA de-excitation code is able to reproduce the experimental data using different formalisms. GEMINI++ requires a parameter tuning in order to predict the fission probabilities, while ABLA considers a fission delay and reduction due to the nuclear friction to reproduce the experimental data, which is mandatory in order to explain the dynamical nature of the fission process.

The predictive power of these codes allow us to perform calculations concerning other systems with different fissility and entrance channel. A survey of the calculations for different systems is presented in Table 2.5. The experimental values are taken from experiments conducted at the FRS dedicated to measure the residues of different spallation reactions. The predictions of

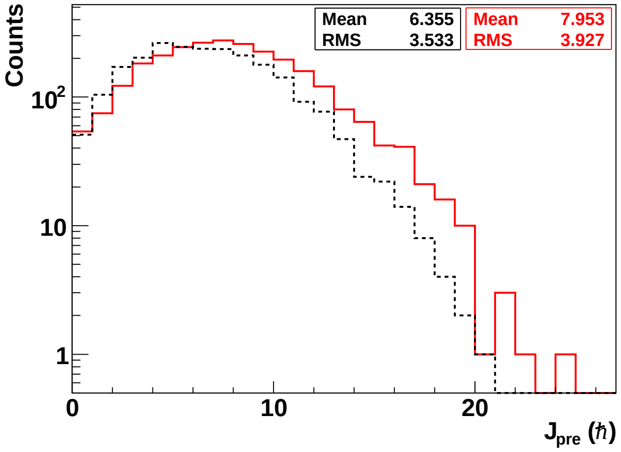

Figure 2.15: Angular momentum distribution of the prefragment calculated with INCL+ABLA (solid red line) and ISABEL+ABLA (dotted black line).

the models have a good agreement with the experimental data considering a value of the dissipation coefficient of around 2.0 and 3.0 $\times$ 10^{21} s^{-1}. Therefore, fission cross sections can be estimated with good accuracy, but, only a rough value of β can be inferred from the values obtained from the model calculations performed for all the systems presented here. Moreover, we have demonstrated before, that, despite calculations with different codes provide similar fission cross section values, other observables present several discrepancies to be addressed. Thus, other experimental signatures are needed in order to completely benchmark the predictive power of the codes, which will allow us to obtain valuable information important for the characterization of the fissioning systems and the interpretation of the experimental data.

Reaction	Energy	$\sigma_{fis}^{\beta=3.0}$ (mb)	$\sigma_{fis}^{\beta=4.0}$ (mb)	Exp. value (mb)
^{238}U+p	1 A GeV	1798	1725	1530 ± 150 [Ber03]
^{238}U+d	1 A GeV	2035	1965	2000 ± 420 [Per07]
^{197}Au+p	0.8 A GeV	81	43	65 ± 10 [Ben01]
^{208}Pb+p	1 A GeV	219	140	157 ± 26 [Enq01]

Table 2.5: Fission cross sections of different systems predicted by INCL4.6+ABLA for two different values of the dissipation coefficient.

2.5. Conclusions

We have investigated the proton induced fission of ^{181}Ta in inverse kinematics at 300, 500, 800 and 1000 A MeV. The combination of the inverse kinematics technique with a highly efficient detection setup made it possible to determine the total fission cross sections with high accuracy. The coincident measurement between both fission fragments and their identification from the rough determination of their atomic number allowed to clearly identify and separate the fission events from other reaction channels. This selection is shown to be extremely useful at lower energy when the fission cross section is small and complicates the identification of this reaction channel. The new data have completed the scarce number of measurements existing above 700 MeV. At intermediate energies, the quality of the new data enabled to clarify previous results. Moreover, these new data are overall in good agreement with the systematics established by Prokofiev over the entire energy range.

A comprehensive comparison of the experimental data with different state-of-the-art models describing fission was made to extract several qualitative results about the dynamics of the fission process and benchmark the codes. Both intra-nuclear cascade codes used in this work (INCL and ISABEL) coupled to ABLA de-excitation code provide a rather good description of the measured fission cross sections, taking into account a dynamical picture of fission. However, it has to be considered that the sensitivity of the fission cross section to the dissipation coefficient β is limited, and, only an approximate value can be estimated for the energy range studied here. On the other hand, INCL coupled to the GEMINI++ evaporation code based on a statistical description of the fission width, underestimates the experimental values obtained in this work. Thus, we have proven that using GEMINI++, the fissioning system needs more excitation energy to undergo fission when compared to ABLA. We also stated the main discrepancies between both intra-nuclear cascade codes (INCL and ISABEL) and both de-excitation models (ABLA and GEMINI++) when calculating the mass and charge distributions of the prefragment and its excitation energy at the saddle point. We have demonstrated that calculations performed with ISABEL at 1 GeV predict fissioning systems with lower angular momentum, and thus, lower fission probability compared to INCL. In conclusion, despite fission cross sections provide valuable information to benchmark the codes, other observables are needed to fully characterize its predictive power.

Chapter 3

Proton- and deuteron-induced fission of ^{208}Pb at 500 A MeV

Spallation reactions induced in heavy-mass nuclei lead to highly excited nuclei characterized by low angular momentum and nearly undistorted shapes. In this scenario which fulfills the conditions established by Grangé and collaborators (see section 1.1.2), one can investigate the dynamics of the fission process at high excitation energies. In this work in particular, we studied transient and dissipative effects experienced by fissile systems produced by bombarding ^{208}Pb nuclei with protons and deuterons at 500 A MeV. Several signatures sensitive to these dynamical effects, such as the total and partial fission cross sections, and, the width of the fission fragments charge distribution, are extracted from this experiments and are expected provide valuable experimental information concerning the magnitude of the nuclear dissipation and the manifestation of a finite fission delay. Moreover, the use of protons and deuterons allows to investigate the effect of the excitation energy induced in the system after the collision.

On the other hand, since lead is a low-cost material and a good high-energy neutron emitter under proton bombarding is also considered as prospective material for the construction of spallation neutron targets and its features under such conditions have to be investigated. Nevertheless, the situation is similar to that of ^{181}Ta and a great experimental effort is needed in order to address the discrepancies of the previously measured data, and, to benchmark nuclear-reaction codes and systematics used to predict the behavior of a large variety of target nuclei under particle irradiation in a wide range of energy.

The detection setup utilized in this experiment is an improved version of the ^{181}Ta experimental scheme detailed in the chapter 2.1. Here, the previous setup was complemented with two new detectors: A double ionization chamber that allowed us to identify with high resolution the nuclear-charge of both fission fragments (Z_1 and Z_2) simultaneously with an efficiency of more than 90% and a time-of-flight (ToF) wall which was used to determine the vertical position of the reaction products.

In the first part of this chapter, a brief overview of the setup and a detailed description of both new detectors is given. In the second part, we will explain the procedure to identify the fission events in order to determine the fission fragment charge distribution, reconstruct the charge of the fissioning nuclei and calculate the total and partial fission cross sections. We will discuss the improvements with respect to the previous method explained in the section 2.2. Then, we will focus on the analysis and interpretation of the observables inferred from the measurement of the nuclear-charges of the fission residues, the partial fission cross sections and the width of the charge distribution. Finally, the observables will be compared with calculations performed with the codes to extract conclusions about dissipative and transient effects in fission.

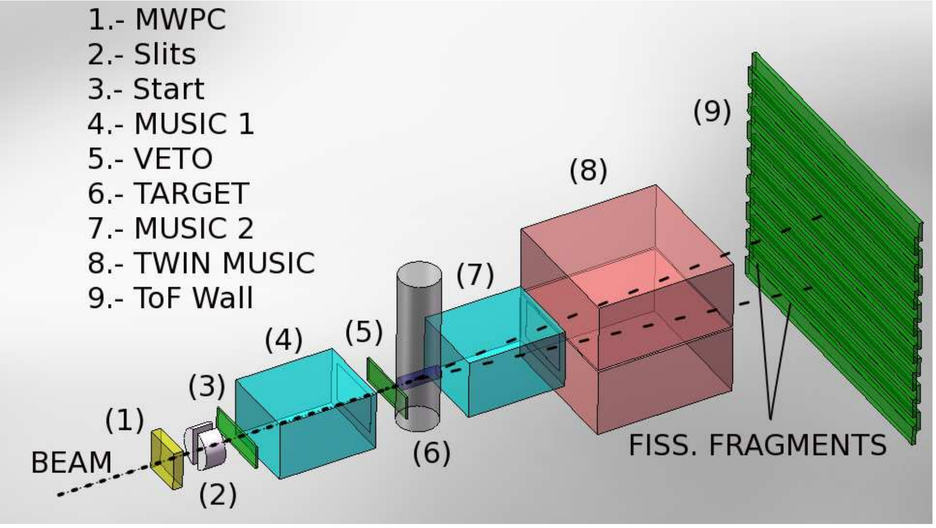

Figure 3.1: Schematic drawing of the experimental setup used in the present experiment.

3.1. Description of the experimental setup

Following the experimental procedure based on inverse kinematics, a ^{208}Pb ion beam was accelerated at the SIS-18 synchrotron and guided through the FRS to the fission setup. As can be seen in Fig. 3.1, the position of the beam at the entrance of the setup was measured with the MW (Multi-Wire [Ste91]) detector and the collimation was made with iron slits. To measure the beam dose together with the fission fragments, we used the scintillator placed upstream of the ionization chamber situated before the target, and, the veto scintillator was used to reject misaligned beam particles. The first scintillator was also used to define the data acquisition trigger. The active target consisted of a cell filled with liquid hydrogen (85 mg/cm^2) or deuterium (201 mg/cm^2) depending on the reaction to be studied isolated by a titanium foil and five layers of Al-coated mylar strips, surrounded by two multi-sampling ionization chambers (MUSIC). In this experiment we used another model of the MUSIC detector with 6 anodes and filled with P10 gas (90% Ar and 10% CH_4). Only the 4 central anodes were used for the read out of the induced signals because the external anodes were used to preserve the homogeneity of the electric field. The operation principle of the chamber is the same as explained in section 2.1. The MUSICs were used to identify reactions of the beam particles with the layers between the FRS exit window and the hydrogen target, and, in the target itself. The detection of both fission fragments simultaneously was made with a double ionization chamber (Twin MUSIC) with high charge resolution, efficiency and acceptance. Due to the kinematics of the reaction both fission fragments are boosted in the forward direction and detected in both parts of the Twin MUSIC. Here, the double paddle scintillator was not installed to avoid secondary reactions of the fission fragments and only the beam trigger provided by the first scintillator was considered for the acquisition. The last detector included in this setup was a time-of-flight wall whose purpose was to measure the position and the velocity of the fission fragments as well as a rough determination of its nuclear-charges. In the following we will describe the two new detectors added to the experimental setup described in chapter 2

3.1.1. Twin MUSIC

The Twin MUSIC detector is a double ionization chamber consisting of two active volumes of the same dimension (see Fig 3.2) filled with P10 gas and separated by a common central cathode with two windows of 25 μm aluminized Kapton. The dimensions of the outer volume of the chamber are 800 mm long, 400 mm height and a width of 600 mm. The cathode was supplied with -4000 V and two groups of four anodes, placed at the top and bottom of the chamber, with 1000 V each. This creates an uniform electric field in both parts of the chamber which forces the electrons liberated in the ionization of the gas by an ion crossing it, to drift to the anodes where the signal is induced and read out from each side of the anode (16 signals) by the pre-amplifiers. The signal is proportional to the energy loss of the ions, and therefore, to its nuclear-charge. The anodes were designed with a triangular geometry to allow the measurement of the horizontal position of the fragments. The vertical position is determined from the drift time of the electrons measured in each anode (8 signals). The position of the cathode in the setup was coincident with the height of the beam in order to maximize the geometric efficiency of the setup and avoid the recombination of the positively-charged non-fissioning projectiles with the electrons released in the ionization of the gas by the fission fragments. The pre-amplified signals are sent to a shaping amplifier to filter the lower frequencies and improve the resolution, and then, they are digitized using and V785 ADC and V775 TDC, both CAEN VME modules.

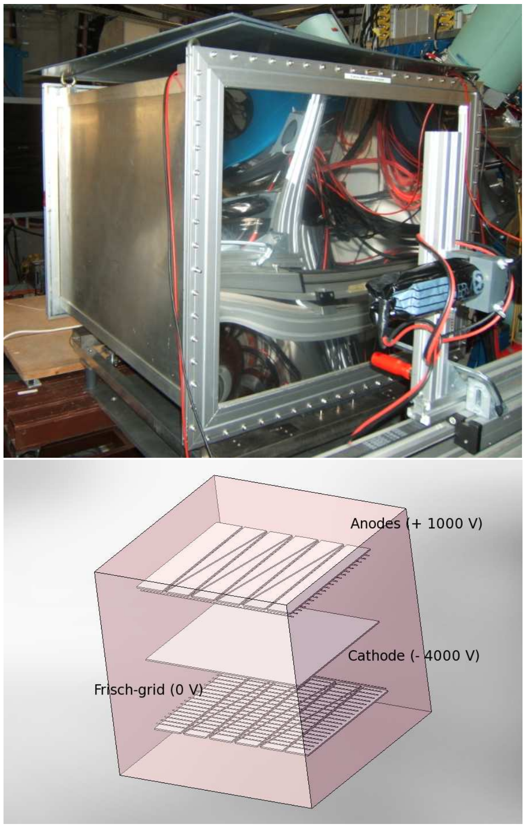

Figure 3.2: Picture of the Twin MUSIC detector.

3.1.2. Time-of-flight wall

The ToF wall consisted of 15 BC420 scintillator paddles of 1 m long, 10 cm high and 5 mm thick disposed in two planes (front and rear) covering an area of 1 m^2. Each paddle of the front (rear) plane had an overlap of 3.3 cm in the vertical direction with the adjacent paddles situated in the rear (front) plane, as shown in Fig. 3.3. One additional paddle was mounted in vertical position to facilitate the calibration in time of the other scintillator paddles. The paddles are coupled to HAMAMATSU H2431se1 fast photomultipliers in both extremes which allowed the measurement of the horizontal position. The granularity in the vertical direction (3.3 cm) allowed to determine the vertical position of both fission fragments. This detector was proposed as a solution for the measurement of the velocities of the fission residues with high resolution and determine their atomic charge. The time resolution of this ToF wall is around 170 ps (FWHM).

Figure 3.3: Picture of the ToF Wall.

3.2. Identification of the fission products

The selection of the fission products was done using the information of both MUSICs surrounding the target and the information given by the double ionization chamber and the ToF wall. In the upper panel of Fig. 3.4 the energy loss of ions in both MUSICs is shown. In the diagonal of this scatter plot, ions with different atomic number that did not interact with the target are represented. These ions were produced in nuclear reactions of the lead beam with layers of matter placed upstream of the target. The vertical line represents residual heavy nuclei and emitted light fragments from evaporation processes produced in the interaction of ^{208}Pb beam particles with the target. The energy loss of nuclei in the MUSICs is proportional to their atomic number squared (Z^2) and considering $\Delta E_{f.f.} \propto Z_1^2 + Z_2^2 = Z_{beam}^2/2$, where $\Delta E_{f.f.}$ is the energy loss of both residues in the MUSIC 2, the fission fragments are located around channel 500 on the MUSIC 2 energy loss axis. Furthermore, a selection in the MUSIC 1 was made in order to reject ions with nuclear charges lighter than ^{208}Pb and count the number of lead projectiles (see lower panel of Fig. 3.4).

Focusing on the region in the scatter plot of both MUSICs where the fission is expected (rectangular selection represented in the upper panel of Fig. 3.4), fission events were easily identified combining the energy loss of each fission fragment in each part of the double ionization chamber, as shown in the two-dimensional energy-loss spectrum in Fig. 3.5. The solid line encloses the events of interest. This method used to identify and isolate fission events had higher precision compared to that of used in the ^{181}Ta experiment, owing to the clear separation of the fission products from the fragmentation and evaporation backgrounds in the Twin MUSIC detector.

3.2.1. Nuclear-charge calibration

The energy loss of both fragments was transformed into atomic charge considering that Z$\propto \sqrt{\Delta E}$. The square root of the energy-loss signals of the selected fission events is represented in a two-dimensional plot shown in Fig. 3.6. Here, the diagonal lines correspond to different charges of the fissioning nuclei. The absolute calibration in atomic number Z was performed using the sum spectrum of the charges of both fragments Z_1+Z_2, assuming that the peak with highest value of Z_1+Z_2 corresponded to fission after the exchange of one proton of the target with one neutron of the projectile, and the adjacent peak on the left with higher intensity corresponded to the atomic number of the projectile Z=82. We also assumed for the calibration the charge distribution of the fission fragments to be identical for both parts of the Twin MUSIC. The resolution of the detector was found to be σ=0.55 charge units (around 1.4%). Aside from the calibration in charge of both parts of the detector, we also determined with this procedure the charge of the fissioning nucleus for the ^{208}Pb+p and ^{208}Pb+d reactions. The distributions of Z_{fiss} (charge of the fissioning system) are shown in Fig. 3.7. At first glance

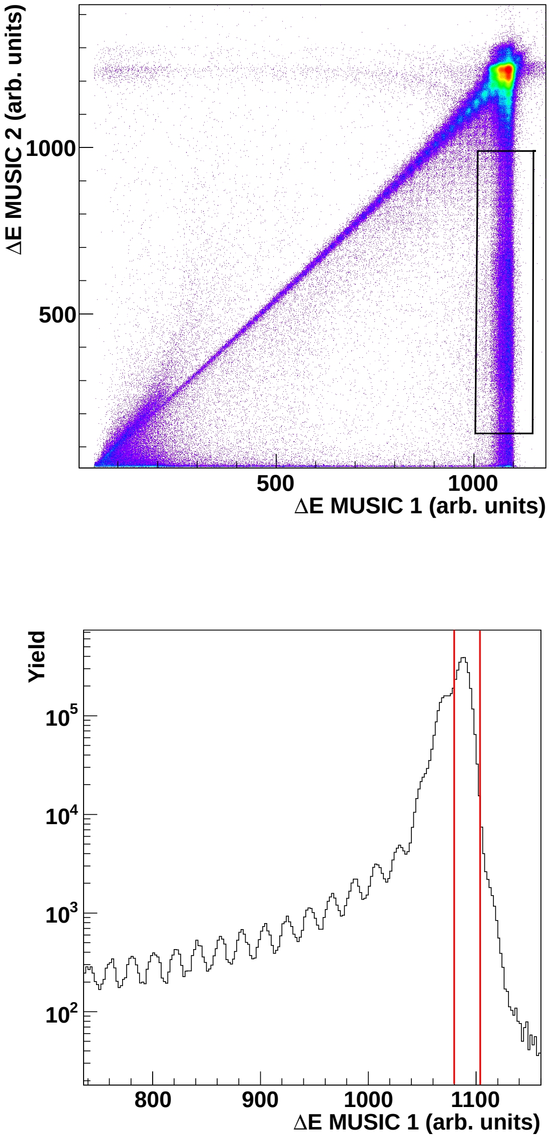

Figure 3.4: Upper panel: Scatter plot of the amplitudes of the signals registered with the two MUSIC detectors. The rectangular selection represents the region were fission residues were expected. Lower panel: Energy Loss signals provided by the MUSIC 1. The region between the red lines corresponds to ^{208}*Pb beam particles.*

one sees that in the collision with deuteron, the excitation energy induced in the reaction is larger than the proton one which allow us to produce fissile

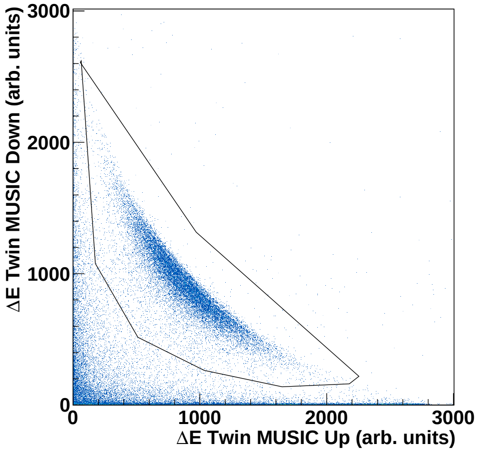

Figure 3.5: Two-dimensional spectrum of the energy-loss amplitude signals of the fission fragments recorded separately in the Twin MUSIC detector. The solid-line box encloses the fission events.

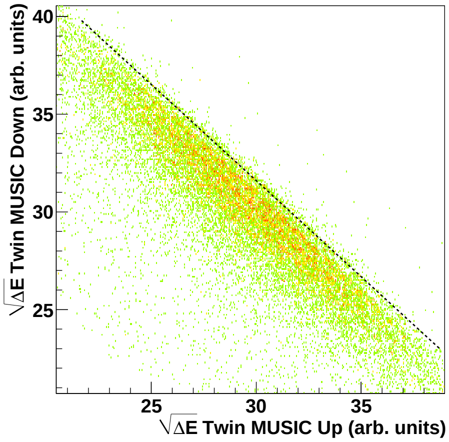

Figure 3.6: Same as Fig. 3.5 but for the square root of the energy-loss of both fragments. The dotted line represents the charge of the fissioning nucleus $Z_1+Z_2=83$.

systems with lower Z_{fiss}.

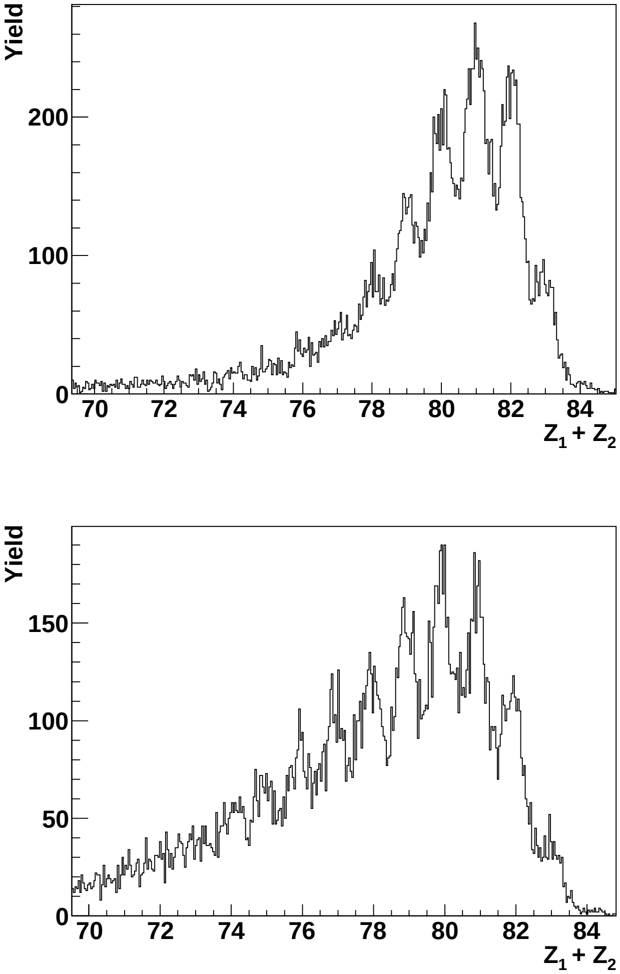

Figure 3.7: Sum spectrum of the nuclear charges of the fission fragments Z_1*+*Z_2*. Upper panel:* ^{208}*Pb+p. Lower panel:* ^{208}*Pb+d.*

3.2.2. Detection efficiency

Both fission fragments had a non-negligible probability of passing through the same part of the Twin MUSIC owing to the alignment of the chamber with the beam axis and the beam emittance. Also fragments may pass close to the cathode which also derives in an incorrect detection due to the homogeneity of the electrical field in that region. The overall detection efficiency is thus reduced since the condition to recognize a fission event is the detection in both parts of the Twin MUSIC. To evaluate the losses we calibrated the position, and, the angle of the fragments inside the chamber. The horizontal position of the fragments was given by the triangular geometry of the anodes. The position was calculated considering that:

$$x(mm) = 300\frac{Q^l - Q^r}{Q^l + Q^r} \tag{3.1}$$

where the factor 300 corresponds to the length of the anodes and Q^l and Q^r are the charges of the signal induced in the anodes that were read out from left and right side, respectively. We calculated the position in the fourth anode of the Twin MUSIC.

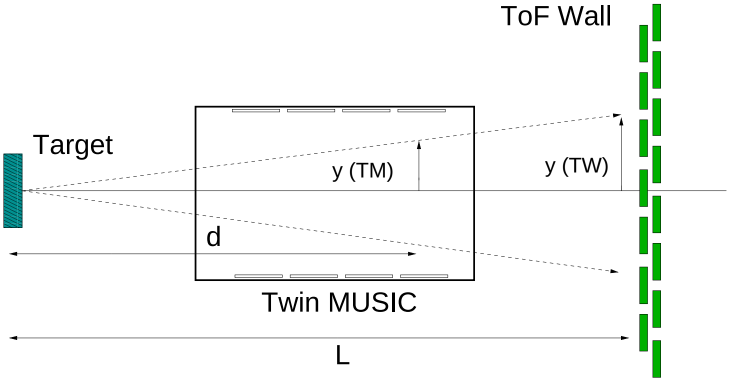

Figure 3.8: Determination of the vertical positions in the ToF Wall and in the anode of the Twin MUSIC.

Figure 3.8 shows a sketch of the fission fragment trajectories inside of the Twin MUSIC chamber and its impact point at the segmented ToF Wall. The vertical position was determined using the difference of the drift times measured in the first and the fourth anodes of both parts of the chamber, and, the vertical position on the ToF Wall were the fragments impinged. As we mentioned before, each paddle in the ToF Wall had an overlap of 3.3 cm with its respective neighbours defining a detection cell. In addition, due to this disposition a cell of 3.3 cm was defined in the center of each paddle without any overlap. Thus, the rough position of the fission residues corresponded to the height of the cells where the fragments impinged. The position calibration was made representing the spectra of the drift time differences recorded in both parts of the Twin MUSIC in coincidence with different cells of the wall (see left panel of Fig. 3.9). In order to do this, we considered double multiplicity, this is, each of both fragments arrived to two different cells of the ToF Wall, one over and one below the beam line, respectively. The paddle situated in the beam line was not considered for calibration effects. As can be seen in Fig. 3.9, each drift time distribution is limited by the physical boundaries of the different cells. Therefore, the drift times were calibrated taking into account the vertical position of each cell in the ToF Wall using the following linear correlation:

$$y^{TW} = a\left(T_4^d - T_1^d\right) + b \tag{3.2}$$

where T_4^d and T_1^d were the drift times measured in the first and fourth anode, respectively. The a and b coefficients were inferred from the linear fit of the functions represented in the right panel of the Fig. 3.9. The position of the fragments in the fourth anode of the Twin MUSIC (y^{TM}) were calculated considering the distances of the anode (d) and the ToF Wall (L) from the target using a geometrical relation:

$$y^{TM} = y^{TW}\frac{d}{L} \tag{3.3}$$

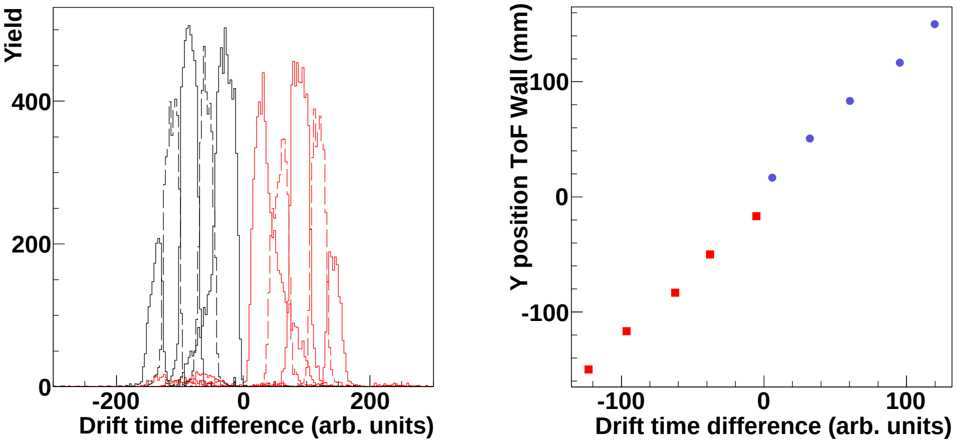

Figure 3.9: Left panel: Difference of the drift times measured in the first and fourth anode of both parts of the Twin MUSIC in coincidence with each cell. Right panel: Calibration of vertical position of the boundaries of the different cells as a function of the drift time. Red squares and blue circles refer to the lower and the upper part of the Twin MUSIC, respectively.

To determine the detection efficiency of the Twin MUSIC, the spatial two-dimensional distribution of the fragments in the position of the fourth anode of the Twin MUSIC, represented in the left panel of Fig. 3.10, was extrapolated for all detected fission events. The distribution had a dimension of around 20×20 cm^2 and an expected symmetric ring shape due to the Coulomb repulsive force between both fragments. To evaluate the losses due to fragments passing close to the cathode of the chamber and misalignment of the beam, the two-dimensional distribution of Fig. 3.10 was projected into the y coordinate axis. The depression in the center of the spectrum was caused by fragment losses and it allowed to determine the efficiency of the chamber by fitting this spectrum using a rectangular function convoluted with a Gaussian distribution due to the different velocities caused by the mass split of the fission fragments, as represented in the right panel of Fig. 3.10. The symmetry of the experimental spectrum was distorted due to a malfunction of the upper part of the Twin MUSIC when registering fragments near the cathode. Around 1% of the total amount of events were registered with negative drift time differences which induced a systematic uncertainty. A Monte Carlo simulation, already explained in section 2.2, was performed to evaluate the uncertainty in the determination of the Twin MUSIC efficiency considering the beam emittance and the distance of the fourth anode of the Twin MUSIC from the target. The geometrical efficiency of the chamber and its uncertainty was evaluated introducing a variable-size dead zone due to the cathode thickness in the detection plane. Since in this calculation we only considered geometrical limits, the simulated spectrum presented sharp edges in the dead zone as shown if Fig. 3.11, contrary to the experimental spectrum, where the position is determined by the drift time difference. With this information, the efficiency of the Twin MUSIC was estimated to be 94±5 % for ^{208}Pb + p and ^{208}Pb + d reactions.

3.3. Total fission cross section

To determine the total fission cross sections, we counted the number of fission events n_{fiss}, which were unambiguously identified inside the polygonal selection of the Twin MUSIC energy loss plot in the upper panel of Fig. 3.6. Furthermore, the contamination of the fragmentation background was estimated by projecting the two-dimensional spectrum of the nuclear charges of the fission fragments registered by the Twin MUSIC onto an axis perpendicular to the $Z_1 + Z_2 = 82$ axis direction (see lower panel of Fig. 3.6), and then fitting the projected spectrum with the sum of two exponential functions, drawn in Fig. 3.12. With the value of the integral of the functions, we inferred the amount of background underneath the fission region, ε_b, which amounted to less than 3% for measurements with proton, deuterium and empty target. Hence, the number of fission events was corrected by a factor f_b=(1-ε_b).

Secondary reactions of the fission residues in layers of matter placed between the target and the entrance of the Twin MUSIC were evaluated using

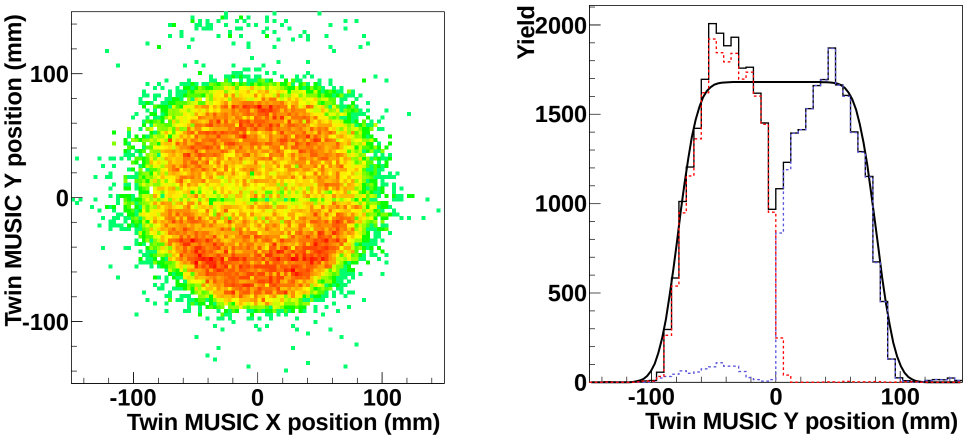

Figure 3.10: Left panel: Calibrated two-dimensional distribution of the fragments in the detection plane perpendicular to the beam direction for the reaction ^{208}Pb + p at 500 A MeV. Right panel: Projection of the distribution into the y axis. The thick solid line represents the fit to a rectangular function convoluted with a Gaussian. The red dashed and blue dashed distributions correspond to lower and upper part of the Twin MUSIC, respectively.

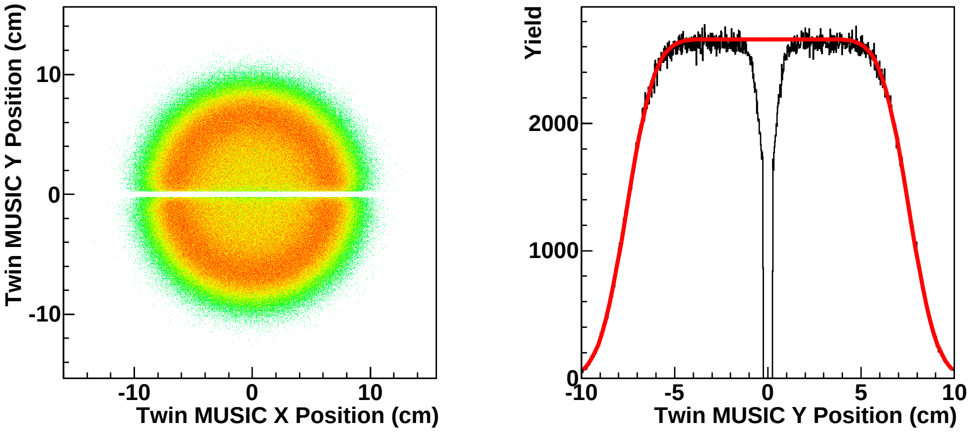

Figure 3.11: Simulation of the spectra shown in Fig. 3.10.

Karol's microscopic model. The losses induced by secondary reactions were moderate since most of them were peripheral. A correction factor f_d=1 / (1- ε_d), where ε_d was the number of reactions which amounted to less than

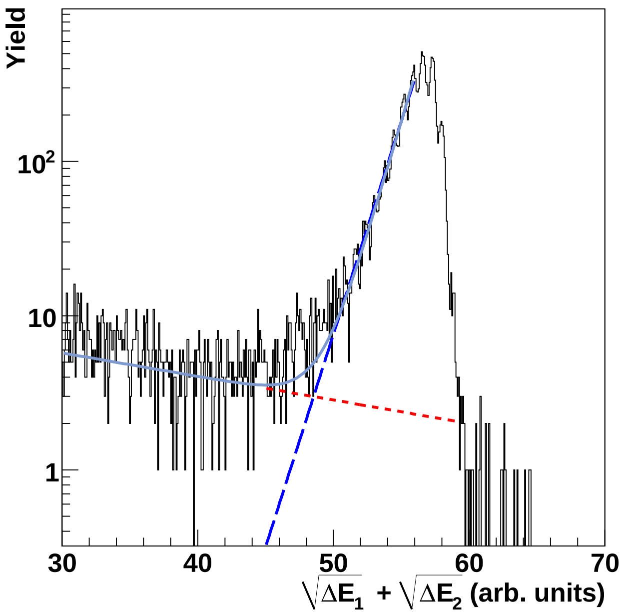

Figure 3.12: Projection of the fission region along an axis perpendicular to $Z_1 + Z_2 = 82$. ΔE_1 *and* ΔE_2 *refer to the energy loss in the upper and lower part of the Twin MUSIC. The dashed line and the dotted line are the exponential functions fitted to the fission and background regions, respectively. The solid line represents the sum of both functions. The plot refers to the reaction* ^{208}*Pb+p at 500 A MeV.*

4% for full target and less than 0.5% for the empty target for both reactions studied in this work. The fission yields Y_{fiss} were calculated with the following expression:

$$Y_{fiss} = n_{fiss} \cdot f_d \cdot f_{geo} \cdot f_b \tag{3.4}$$

where $f_{geo} = 1/\varepsilon_{geo}$ was the geometrical correction factor and ε_{geo} the Twin chamber efficiency. The number of lead projectiles n_b was determined with spectrum of the MUSIC 1 represented in the lower panel of Fig. 3.4, and, the first plastic scintillator which also provided the only trigger for the data acquisition. We applied a correction, f_a, to the total number of projectiles due to the attenuation of the beam intensity along the target thickness. The mean attenuation of the beam, ε_a, was calculated considering a lineal decrease of the beam intensity and corresponded to the value after crossing half the target. Thus, the number of projectiles was evaluated following $N_b = n_b \cdot f_a$

where $f_a = (1 - \varepsilon_a)$. The values of the different factors are shown in the table 3.1.

Reaction	ε_a	ε_d	ε_{geo}	ε_b
^{208}Pb+p	4.72%	4.33%	94%	2.54%
^{208}Pb+d	6.05%	5.54%	94%	2.12%
^{208}Pb+empty	0.5%	1.35%	94%	2.87%

Table 3.1: Twin MUSIC efficiency (ε_{geo}), beam attenuation (ε_a), secondary reactions of the fission fragments (ε_d) and fragmentation background ε_b for each reaction studied in this work.

Fission yields with empty target were determined in order to subtract the contribution of fission reactions taking place in any layer surrounding the target cell. The total fission cross sections were obtained by normalizing the corrected fission yields for full and empty target, to the number of projectiles and the number of nuclei in the target per unit area N_t:

$$\sigma = \left(\frac{Y_{fiss}^{full}}{N_b^{full}} - \frac{Y_{fiss}^{empty}}{N_b^{empty}} \right) \cdot \frac{1}{N_t} \tag{3.5}$$

The value of the fission cross sections are listed in the table 3.2. The associated uncertainties were determined with a precision for the total fission cross sections of around 7%. The main contributions to the systematic uncertainty were the uncertainties of the target thickness ($\approx 4\%$), beam intensity ($\approx 5\%$), determination of the fission events (1.24%, 2.61% and 3.56% for proton, deuteron and empty target respectively) and corrections factors (less than 1%). Furthermore, we considered a systematic uncertainty of 1.5% due to the misidentified events in the upper part of the Twin MUSIC. The statistical contributions amounted to less than 1% in all cases.

We compared the results with previously measured data found in the literature. For the reaction ^{208}Pb+p at 500 A MeV, the data measured at the FRS amounted to 232±33 mb [FD05] having a deviation of more than 50% with respect to the result of this work . The precision achieved in this measurement was constrained by the limited acceptance of the spectrometer and large correction factors were needed. Vaishnene *et al.* [Vai10] measured a value for the fission cross section of 110±7 mb using a scintillator counter telescope to count the beam dose and PPAC detectors (Parallel

Reaction	Fiss. Cross Sections	Stat. uncert.	Syst. uncert.
^{208}Pb+p 500 A MeV	152 ± 10 mb	0.88%	6.53%
^{208}Pb+d 500 A MeV	207 ± 14 mb	0.74%	6.54%

Table 3.2: Total fission cross sections determined in this experiment.

Plate Avalanche Counter) to detect the fission fragments. This experiment was performed in direct kinematics using a proton beam of 505 MeV. Furthermore, we compared the values of the cross sections obtained in this work with the systematics establish by Prokofiev. There exists a discrepancy between the predicted values (112 mb) and our data of around 20%. It is worth pointing out that the systematics were based on evaluation of cross sections measured before 2001 with a limited amount of data, especially at 500 A MeV where the information was non-existing.

3.4. Partial fission cross section

Partial fission cross sections, for both ^{208}Pb+p and ^{208}Pb+d reactions, were calculated by determining the fission yields for full and empty target for each Z_1+Z_2 value. Similarly to the procedure we used in the previous section to calculate the total fission cross sections, we deduced each yield normalizing the number of fission counts registered for each fissioning system to the total number of ^{208}Pb projectiles. Similar correction factors depending on the atomic number of the fissioning system were applied. Then, after subtracting the empty target contribution, we normalized each yield to the number of nuclei in the target per unit area N_t. The results are shown in the plot of Fig. 3.13 and listed in the table 3.3.

The maximum value for the cross section for both reactions is found at $Z_1+Z_2=81$. The partial cross section gradually decreases with decreasing in Z_1+Z_2 since the fission barriers become higher as more nucleons are removed from the fissioning nuclei and the fissility is decreased. Therefore, higher excitation energies are needed to undergo fission. Since in the ^{208}Pb+d reaction the average excitation energy induced in the system is larger, total fission cross section is also increased and the fissile systems with lower Z_1+Z_2 values are produced when compared to the ^{208}Pb+p case. It is worth pointing out that for values of $Z_1+Z_2>80$, there exists a difference between both curves that can be explained in terms of impact parameter. In the case of

Z_1+Z_2	σ_p (mb)	σ_d (mb)
84	0.58±0.11	0.48±0.10
83	11.11±0.82	7.14±0.53
82	28.84±2.00	18.60±1.26
81	32.72±2.26	26.55±1.76
80	26.73±1.86	26.12±1.73
79	18.13±1.29	24.38±1.61
78	10.91±0.81	21.03±1.40
77	6.72±0.53	17.76±1.20
76	3.91±0.35	14.00±0.96
75	2.10±0.24	11.45±0.80
74	1.48±0.20	8.54±0.62
73	0.95±0.17	6.58±0.50

Table 3.3: Values of the partial fission cross sections for ^{208}Pb+p (σ_p) and ^{208}Pb+d (σ_d) at 500 A MeV.

very peripheral collisions (high impact parameter) the lead projectile might be excited either by the proton or the neutron. Owing to this reason the expected partial fission cross sections decreases since the total fission cross section of ^{208}Pb+n is lower than in the proton-induced case [Tar11]. Events with Z_1+Z_2=83 correspond to projectiles which underwent fission after a charge-exchange reaction.

3.5. Width of the fission fragments nuclear-charge distribution

Another signature we exploited in this work is that of the widths of the fission fragments charge distributions (σ_z) determined for each fissioning system Z_1+Z_2. As stated in the chapter 1, the temperature of the system at

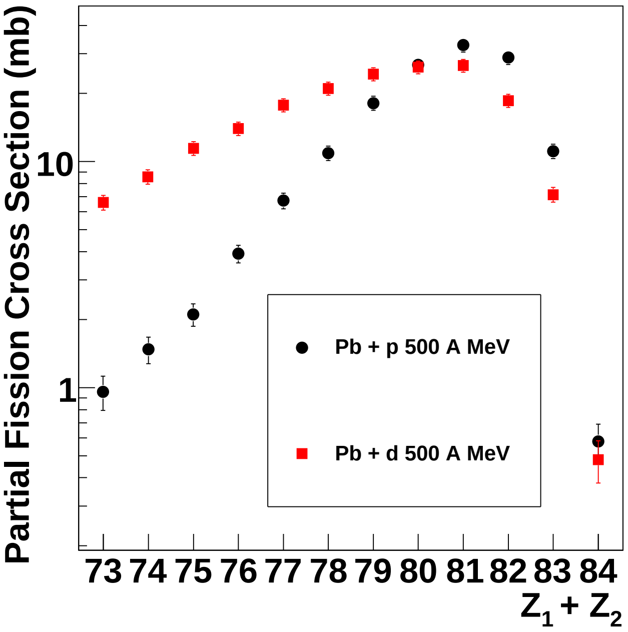

Figure 3.13: Partial fission cross sections. Solid circles and solid squares refer to ^{208}Pb+p and ^{208}Pb+d at 500 A MeV, respectively.

the saddle point is associated with the width of this distribution following the equation 1.7. A value for the integral charge distribution of the fission fragments σ_z of 6.5 ± 0.4 charge units was measured in the present experiment for the ^{208}Pb+p reaction, in rather good agreement with the value of 6.3 ± 0.3 charge units of the Ref. [FD05]. Going a step further, the evolution of the temperature T_{sad}, and, therefore the excitation energy at the saddle point, was investigated by measuring σ_z for each Z_1+Z_2 value. The distributions are shown in Fig. 3.14.

The mean value of the distribution, as expected, decreases with decreasing in Z_1+Z_2 [Sch10]. Conversely, the width of the distribution is increased since the excitation energy of the fissioning nuclei increases for lower values of Z_1+Z_2 as can be seen in Fig. 3.15. This figure also shows that σ_z has the same value in both reactions within the errors bars for each Z_1+Z_2 value independently of whether a proton or deuterium target is used, indicating that the temperature gained by the system does not depend on the reaction used. However, fluctuations may appear since the mass of the fissioning system differs for each Z_1+Z_2 value and the properties concerning excitation

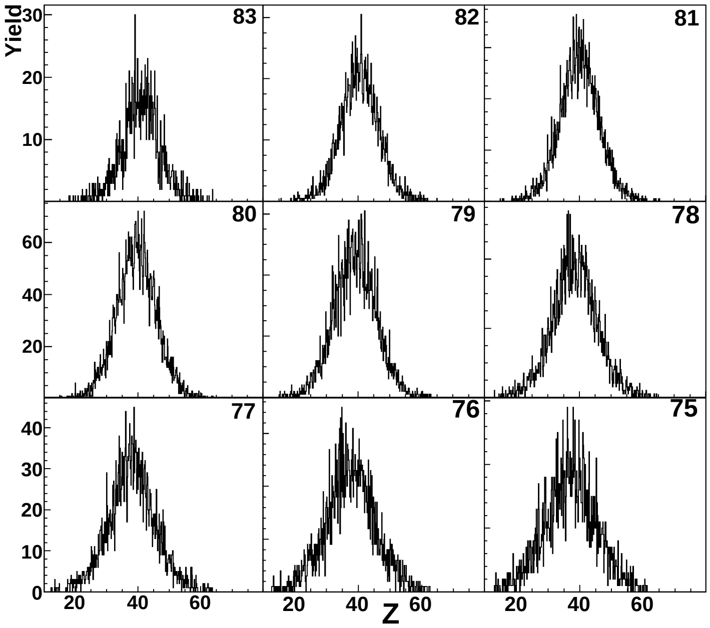

Figure 3.14: Experimental widths of the charge distribution of the fission fragments. The number in the upper right corner represents each Z_1+Z_2 value.

energy may change.

3.6. Comparison with model calculations

In order to infer qualitative results about the influence of the nuclear dissipation and the transient delay on the fission of ^{208}Pb at high excitation energy calculations with state-of-the-art codes are needed. For this purpose, we have used two different intra-nuclear cascade codes, INCL and ISABEL, describing the interaction stage. These codes were coupled to the statistical evaporation code ABLA which includes a time-dependent description of the fission width. As can be seen in Fig. 3.16, for the highest values of Z_1+Z_2, calculations performed with INCL+ABLA for the reaction ^{208}Pb+p at 500 A MeV considering Bohr-Wheeler fission width (solid black line) overestimate the experimental values while calculations performed considering $\beta = 4.0 \times 10^{21}\ s^{-1}$ (dashed black line) have a good agreement in the range from Z_1+Z_2=80 up 82. Nevertheless, partial fission cross sections of fissile systems with higher excitation energies (Z_1+Z_2<80) are not properly reproduced. Calculations performed with ISABEL+ABLA with the same β values fail in the predictions of the experimental data. It is worth mentioning that

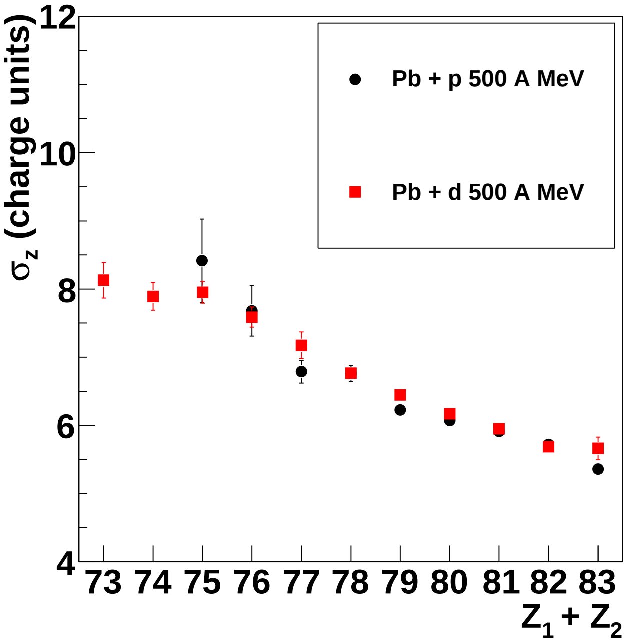

Figure 3.15: Width of the charge distribution of the fission fragments for each Z_1+Z_2 *value. Solid circles and solid squares refer to* ^{208}*Pb+p and* ^{208}*Pb+d at 500 A MeV, respectively.*

both cascade provide similar total fission cross sections, 96 and 114 mb for INCL and ISABEL ($\beta = 4.0 \times 10^{21}\ s^{-1}$), respectively. In this sense, one can deduce that the shape of the calculated curves depends only on the excitation energy induced to the system in the cascade stage which define the characteristics of the fissioning system, while the value of the cross sections depends on the magnitude of the dissipative coefficient defined in the de-excitation stage. On the other hand, calculations made for the ^{208}Pb+d reaction at 500 A MeV with INCL+ABLA codes are presented together with the experimental data in Fig. 3.17. The model predictions considering $\beta = 4.0 \times 10^{21}\ s^{-1}$ (dashed-dotted line) have a rather good agreement in almost the entire range studied here. Calculations performed according to the statistical model ($\beta = 0\ s^{-1}$) overestimate the experimental values (solid line). The version of the ISABEL code used in this work does not allow calculations using deuterons as projectile.

We have seen here and in the previous chapter that only rough qualitative conclusions about the strength of the dissipative effects can be inferred from

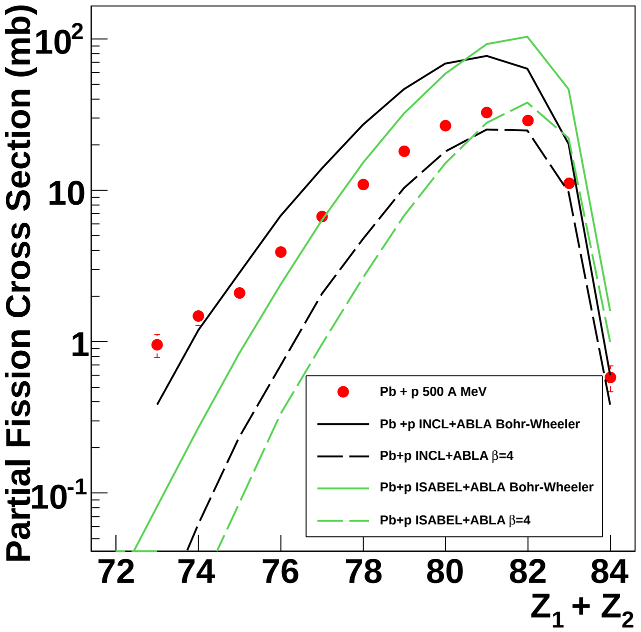

Figure 3.16: Partial fission cross section as a function of Z_1+Z_2 for the reaction ^{208}Pb+p at 500 A MeV compared to several calculations performed with INCL+ABLA (black) and ISABEL+ABLA (green) with $\beta = 0$ (solid line) and $\beta = 4.0 \times 10^{21}$ s^{-1} (dashed line), respectively.

signatures related to the fission cross sections and thus transient time has to be investigated in other observables more sensitive to these effects. Contrary to the fission probability where the modification of the fission barrier, angular momentum and fissility of the fissioning system caused by the evaporation of particles smear out transient effects, σ_z is especially sensitive to pre-saddle dynamics due to its strong connection with T_{sad}. Rich information can be extracted from the comparison of the experimental data with calculations performed with INCL+ABLA. As can be seen in Fig. 3.18, calculations for ^{208}Pb+p at 500 A MeV according to the statistical (solid line) and Kramers (dash-dotted line) models overestimate the experimental values of σ_z while predictions using $\beta = 4.0 \times 10^{21}$ s^{-1} show a drastic reduction of σ_z (dashed line refers to ^{208}Pb+d and dotted line refers to ^{208}Pb+p both at 500 A MeV), and thus, of T_{sad}. This reduction of T_{sad} is caused by a fission delay that enhances the evaporation of lighter particles, mainly neutrons, causing the nucleus to cool down. One has to consider that the value of σ_z is determined

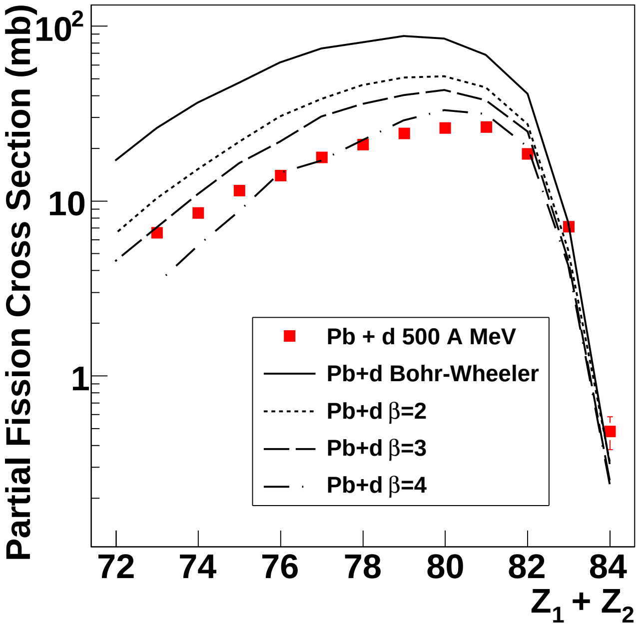

Figure 3.17: Partial fission cross sections as a function of Z_1+Z_2 for the reaction ^{208}Pb+d at 500 A MeV compared to calculations performed with INCL+ABLA for different values of β.

during the evaporation stage and therefore, the shape of the Z_{fiss} distribution which is mainly determined by the excitation energy induced to the system during the cascade stage does not have an appreciable effect on the transient time. It is worth pointing out that this reduction of σ_z is attributed only to the transient time and not to the dissipation strength, as shown in Fig. 3.18.

In conclusion, the comparison of the experimental data with several calculations performed with INCL+ABLA and ISABEL+ABLA provide valuable information about the behavior of a fissioning system at high excitation energy. While partial fission cross sections are used to benchmark the intranuclear cascades, σ_z validates the performance of the evaporation code we have utilized for these calculations. Therefore, one can see that each signature is sensitive to one stage of the process.

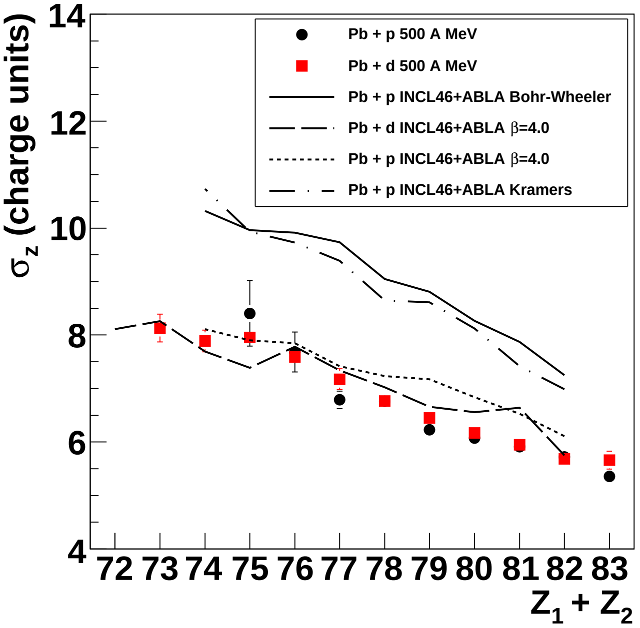

Figure 3.18: σ_z as a function of Z_1+Z_2 for both reactions studied in this work compared to calculations performed with INCL+ABLA.

3.7. Conclusions

In the present chapter we investigated proton- and deuteron-induced fission of ^{208}Pb at 500 A MeV of energy. A dedicated experimental setup using the inverse kinematics technique was used to unambiguously detect both fission fragments in coincidence with high acceptance and efficiency and determined their atomic number. With this information we reconstructed the charge of the fissioning system which allowed us to determine several observables sensitive to dissipative and transient effects. We determined with high precision the total and partial fission cross sections as a function of the atomic number of the fissioning system, and, the width of the fission fragments charge distribution, σ_z for both reactions. Partial fission cross sections provide valuable information about the cascade stage revealing that deuteron-induced fission lead to higher excited fissioning systems with respect to the reaction induced by protons. Concerning σ_z as a function of Z_1+Z_2, since for both reactions we obtained similar values of this observable for each system studied here, we conclude that this signature is only sensitive to the temperature at the saddle point, T_{sad}, and thus does not depend on which reaction is used to produce the fissioning system.

In addition, a comparison of the experimental results with calculations performed with codes based on models describing the fission process support the manifestation of transient and dissipative effects on the fission process at high excitation energies. This comparison allowed us to benchmark both intra-nuclear cascades, INCL and ISABEL, utilized in this work. We proved that the characteristics of the fissioning system are well defined during the stage described by these codes and they provide different values according to the excitation energy they induce to the system. For ^{208}Pb+d at 500 A MeV, calculations made with INCL+ABLA are in good agreement with the experimental data considering a $\beta = 4.0 \times 10^{21}\ s^{-1}$, and moreover, we have demonstrated that a statistical description of the process lead to an overestimation of the data. This is also consistent with the range of β values considered in the calculations performed to probe the effect of the transient time on the σ_z signature through model calculations.

In conclusion, fission at high excitation energies can be described as a two-step partially decoupled process where the properties of the fissioning system are defined during the first stage, and, the de-excitation mode, in which dissipative effects and transient delay play a key role, is determined during a second stage. This was proved with experimental observables sensitive to each stage and with model calculations supporting these signatures.

Chapter 4

Next-generation fission experiments and needs to improve ToF measurements

In the previous chapters we have demonstrated that a dedicated experimental setup is mandatory in order to provide accurate data on fission fragment nuclear-charges and yields. A substantial progress has been accomplished in the understanding of the dynamics of the fission process with the available technology utilized in these experiments. However, the measurement of other observables requires a more complex detection system, and therefore, an experimental effort is been carried out to improve the resolution, acceptance and efficiency of the current detectors for future outstanding experiments. One of the main challenges is the precise measurement of the masses of the fission fragments that will be made by including in new experimental setups based on the ideas presented in [Sch00], a dipole magnet and a state-of-the-art time-of-flight (ToF) wall with unprecedented time resolution. Considering a flight-path of few meters and a mass resolution of around $\Delta A/A = 3 \times 10^{-3}$, a demanding time resolution of the order of tens of picoseconds is needed to isotopically separate fission fragments masses, and thus, the choice of a proper detection technology is critical for such a ToF wall detector.

In this chapter, we present the R&D carried out in order to design a RPC-based (Resistive Plate Chambers) ToF wall. In the first section, a brief review of three future experiments to be conducted at GSI using this detection scheme (SOFIA, R^{3}B and FELISe) will be presented. In the framework of the R^{3}B experiment, we will explain the main requirements and constraints of a ToF wall for the detection of relativistic ions. Then, we will compare two different technologies for the design of this ToF wall: organic scintillators coupled to fast photomultipliers and Resistive Plate Chambers (RPCs). Since the latest option was considered for its construction, an intensive R&D was carried out to prove the feasibility of RPCs for the detection of relativistic heavy ions, especially of those with typical fission fragments masses. Finally, in the last section we will present the conceptual design of the modules that will constitute the final detector.

4.1. Future fission experiments at GSI

4.1.1. SOFIA

SOFIA (Studies On Fission In Aladin) is a new generation fission experiment in inverse kinematics that will be performed at GSI. The goal of such experiment is the accurate measurement of the fission yields of radioactive actinides with masses below A = 238 ($^{219-232}Ac$, $^{220-236}Th$, $^{225-237}Pa$, $^{230-238}U$ and $^{233-238}Np$) and stable nuclei such as ^{208}Pb. These radioactive nuclei will be produced at the FRS and delivered, with an energy of 600 A MeV, to the ALADIN/LAND experimental area [LAN] where the fission setup based on [Sch00] will be located. An schematic view of the setup is represented in Fig. 4.1. An active target consisting of several lead layers will be used to induce the fission of the projectile either via electromagnetic excitation or nuclear reaction. A double ionization chamber will detect both fission fragments in coincidence and determine their nuclear charges corrected by the velocity. The accurate isotopic identification of the fission fragments will be made using the magnetic field of the ALADIN dipole magnet following the relation:

$$\frac{A}{Z} \sim \frac{B\rho}{\beta\gamma} \tag{4.1}$$

where B is the dipole magnetic field, ρ is the curvature of the particle inside the field, and $\beta\gamma$ is the reduced momentum. The velocity of the fission fragments will be determined with a time-of-flight measurement using a plastic scintillator wall. To separate masses of the fission fragments with a flight-path of 7 m, a challenging resolution of 35 ps FWHM is required. The tracking of the particles, in order to give a precise measurement of the velocity, will be made using two Multi-Wire Proportional Counters (MWPC) with very good spatial resolution, and, the position inside the double ionization chamber given by the segmented anodes and the drift-time of the ionized electrons. The neutron multiplicity will be measured with the LAND neutron wall [Bla92].

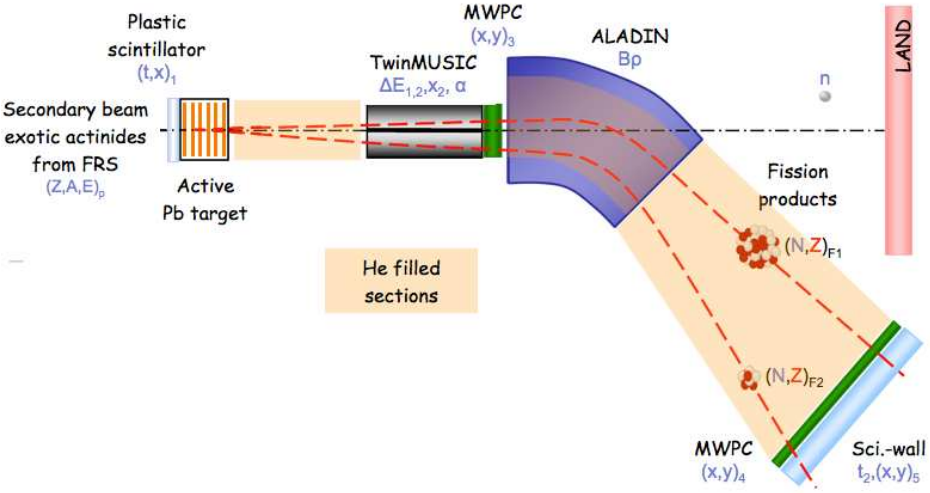

Figure 4.1: Experimental setup for SOFIA experiment

4.1.2. R^{3}B

R^{3}B (Reactions with Relativistic Radioactive Beams) [R3B] experiment will be part of the forthcoming FAIR international accelerator facility (Facility for Antiproton and Ion Research) [FAI] to be built at GSI. The experiment will cover experimental reactions with exotic nuclei far off stability providing unique experimental conditions worldwide. The current GSI installations will be utilized as pre-accelerator of the new SIS100/300 double superconducting synchrotron that will provide ions and antiproton beams with unprecedented characteristics. Intensities of the order of 10^{12} and 10^5 will be achieved for primary [1] and rare isotope secondary beams, respectively. These secondary beams will be produced in the Super-FRS [Gei03] (Superconducting FRagment Separator) and delivered to other experimental areas. The R^{3}B experiment, located at the focal plane of the high-energy branch of Super-FRS, is a future experimental setup aiming at the complete measurement and reconstruction of nuclear reactions in inverse kinematics with beams, both stable and radioactive, at high energy. A wide and outstanding scientific program, focused on studies concerning nuclear structure and dynamics through knockout, quasi-free scattering, charge-exchange or fission reactions among

---

[1] Elements up to uranium will be accelerated with an energy up to 1.5 A GeV.

others, will be carried out using the R^{3}B versatile setup (see Fig. 4.2 for an schematic drawing) which is based on the present ALADIN/LAND reaction setup introducing a substantial technological improvement. Therefore, state-of-the-art detectors with high efficiency, acceptance and resolution are required.

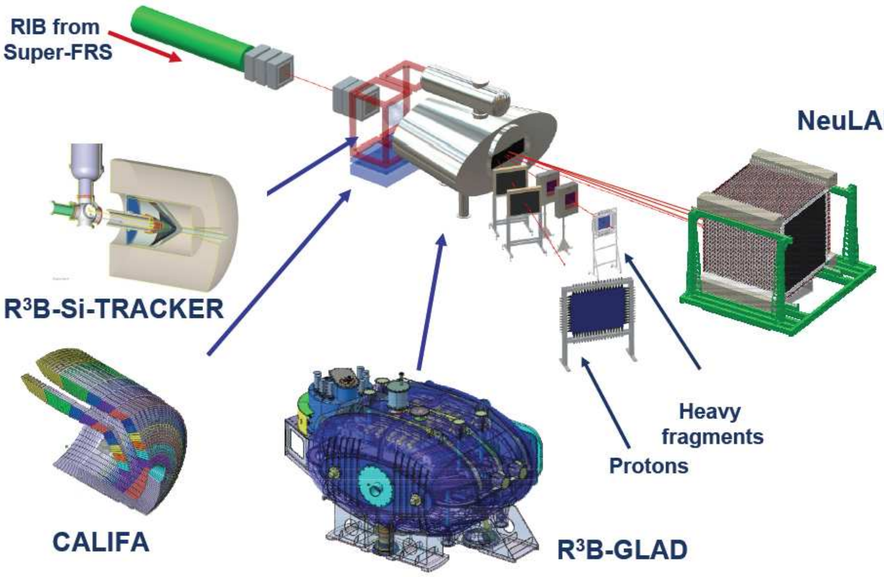

Figure 4.2: Conceptual drawing of the R^{3}B experimental setup.

The main detector system of R^{3}B consists of a large acceptance dipole (GLAD) with around 5 Tm of integral field, heavy-ion silicon tracker detectors, a large-area time-of-flight wall for fission and spallation measurements, a total γ-absorption calorimeter (CALIFA) and a high resolution neutron time-of-flight spectrometer (NeuLAND). Fission experiments will follow a configuration similar to that of the SOFIA experiment using these detectors benefiting from the large acceptance and bending power of the GLAD dipole. The technological improvement of the R^{3}B setup will allow to extend the limits of our knowledge of the dynamics of the fission process and structure effects.

4.1.3. FELISe

Also within the FAIR facility, FELISe (Fission at ELectron-Ion Scattering experiment) will investigate the fission process in exotic heavy ions induced by electrons by exchange of a photon between them. The heavy ions will be produced at the Super-FRS, similarly to SOFIA experiment and the electrons will be accelerated up to 500MeV by the Electron Linear Accelerator and the Electron Antiproton Ring accelerator. Both will be injected in the New Experimental Storage Ring (NESR) where the reaction will take place.

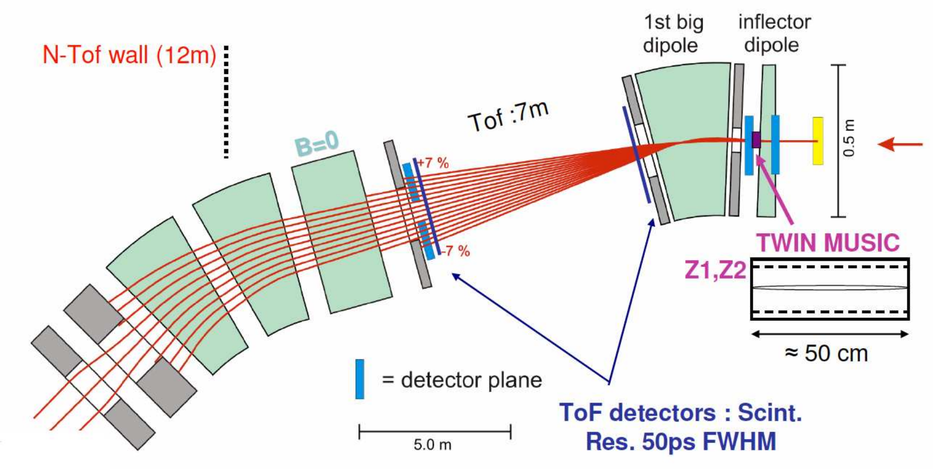

Figure 4.3: FELISE experimental setup.

The detection setup for fission experiments will include a double ionization chamber to identify in charge both fission fragments, a time-of-flight wall and a big dipole to measure the mass with the $\beta\rho$ method and three tracking detectors to measure the position of the fragments. The determination of the excitation energy of the fissioning nuclei by measuring the energy of the scattered electron in an electron recoil spectrometer will constitute a substantial improvement with respect to previous experiments.

4.2. Conceptual design and requirements of the ToF wall of the R^{3}B experiment: iToF

Since the main purpose of the ToF wall of the R^{3}B experiment (hereafter iToF, ion Time-of-Flight wall) is the detection and time-of-flight measurement of relativistic ions produced in fragmentation, fission and also multifragmentation reactions, several parameters must be fixed to establish the conceptual design of such detector. The mass resolution depends on the length of the flight-path, defined as the distance from the reaction vertex to the iToF. Hence, the dimensions of the detection plane are constrained by the flight-path.

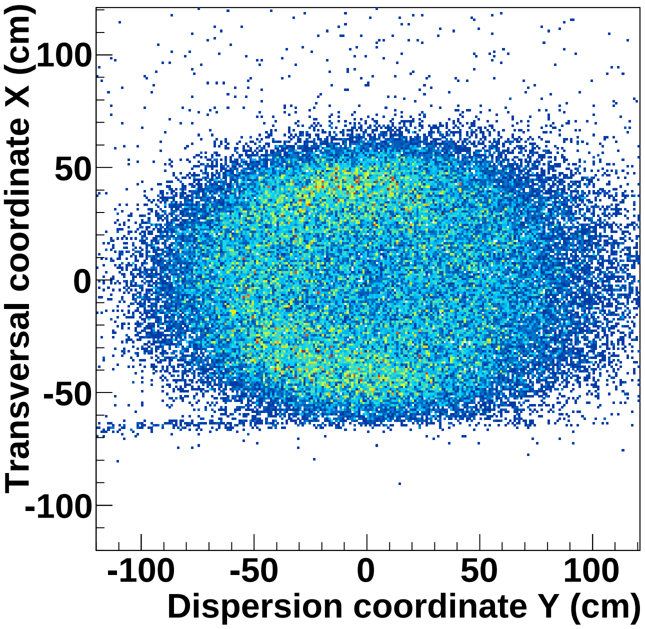

Figure 4.4: Spatial distribution of the fission residues produced in the reaction ^{208}*Pb+*^{238}*U in the iToF detection plane.*

If we want to isotopically separate masses of fission fragments (A<150) a time resolution of around 50 ps (standard deviation) is required for a flight-path of 15 m. In the case of fragmentation of ^{208}Pb or ^{238}U, typically used to produce very neutron-rich species, the time resolution needed is around 30 ps (standard deviation) for fragments with masses around A=200, but the angular aperture is smaller. On the other hand, fission of ^{238}U or ^{208}Pb at 400 A MeV is a benchmark case since it represents the lowest energy of interest in R^{3}B and also the highest angular aperture of the fragments distribution. A simulation of the experimental scheme of the R^{3}B setup performed with GEANT4 transport code provides the geometry and distribution of the products of the reaction. In order to do this, we considered a ^{208}Pb beam impinging onto a ^{238}U target at 400 A MeV of energy. The kinematics of the reaction products were determined with INCL4.6+ABLA codes. Then, in GEANT4 the reaction vertex was placed before the large acceptance dipole (GLAD) and the particles of interest were transported and deflected towards the iToF taking into account their masses and energies. Considering a flight-path of 15 m, the angular aperture in the detection plane is 1 m in the vertical direction, and due to the dispersion introduced by the dipole, the aperture covers up to 2 m in the horizontal direction (see Fig. 4.4).

iToF could be adapted in each case to provide a better time resolution according to the reaction to be measured. This can be achieved by increasing the number of detection planes, n (improving the measurement by a factor $\sqrt{n}$) or by increasing the flight-path. Moreover, beyond fission and fragmentation, the detector could be adapted to reactions where light nuclei and particles are produced. These requirements show clearly that the detector have to cover a broad range of nuclei with different nuclear charges and therefore accommodate a huge dynamical range. A flexible and modular design for the iToF is proposed to adapt the surface and the number of planes to each specific case.

The multi-hit capabilities of the detector are designed according to the particle multiplicities of the reaction mechanisms of interest. Medium-mass residues produced in fission reactions are accompanied mostly by neutrons, while heavy-mass residues are produced together with protons, neutrons, alpha particles and light-mass nuclei. Therefore, as can be seen in Fig. 4.5, each detection plane will be divided in several independent modules segmented in strips covering a surface of 1 m and 2 m in the vertical and horizontal coordinates, respectively [AP06; Cas12a]. The granularity of the detector will be improved by crossing 90° each detection plane as represented in Fig. 4.5. The foreseen reaction rates of the R^{3}B experimental programs will be around few hundred reactions per second in the cases of interest, at the limit. Thus, the expected rates per surface unit will be limited to several ions/cm^2 per second considering multiplicities below 10 and the surface of the detector. With this geometry, the multi-hit capabilities of the detector will be fulfilled.

Since the angular straggling after several meters of flight is a non-negligible quantity, the impact point position has to be determined to correct the length of the flight-path, and to accurately define the velocity required for identification. Due to the relative orientation between consecutive detection planes, the position resolution in the dispersion and transversal coordinates will be given by the time difference between the signals measured in both extremes of the strip where the particle impinged.

4.3. ToF detectors

The measurement of the time-of-flight of the particles in high-energy and nuclear physics experiments is commonly performed using fast detectors capable to reach time resolutions better than hundreds of picoseconds. Two different technologies are discussed in this section: organic scintillators cou-

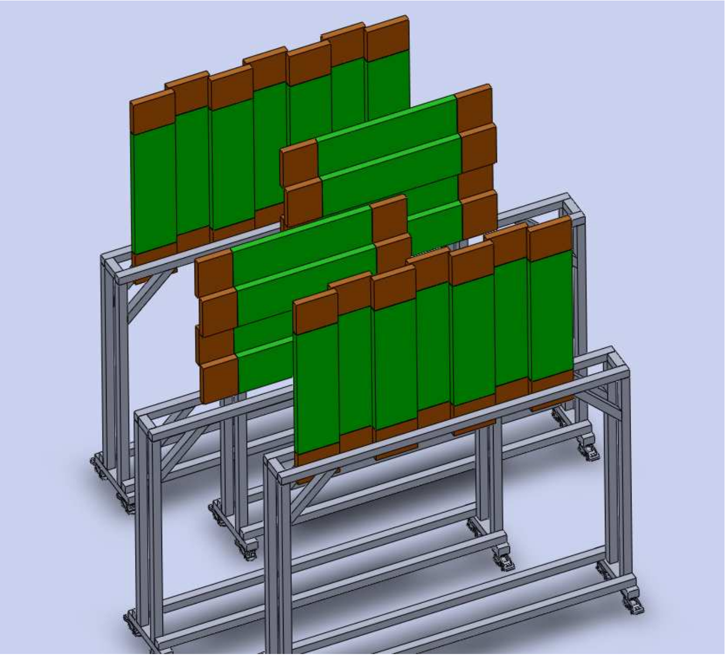

Figure 4.5: Conceptual design of the iToF.

pled to fast photomultipliers (PMTs) and RPCs. Here, we will discuss their general features and their performances for ToF measurements.

4.3.1. Scintillation detectors

There exist many types of scintillator materials with different characteristics suitable for a wide range of applications. The choice of a proper scintillator is a compromise among several parameters such as scintillation efficiency, linearity in light conversion, decay time, optical quality, transparency to the wavelength of emission and index of refraction. Scintillators can be classified basically in two groups: inorganic crystals and organic (plastic and liquid) scintillators. The former are excellent for γ spectroscopy due to its density the linear behavior of the scintillators in the conversion of deposited energy into light, although their responses and decay times are slower. For timing measurements organic plastic scintillators coupled to fast PMTs are the most used detectors owing to their time resolution, fast recovery and the possibility of manufacture the material to assemble large-size structures such as time-of-flight walls. There exists several large-area scintillator walls installed in high energy physics experiments such as HADES at GSI with a time resolution of about 100 ps (standard deviation), the ToF wall of the HARP experiment with 160 ps of time resolution and the ToF barrel of the former DELPHI experiment at CERN. Moreover, a scintillator-based ToF wall with an expected resolution of around 100 ps is proposed for the forthcoming PANDA experiment at GSI[Bus05].

4.3.1.1. Organic scintillators

A particle crossing an organic scintillator deposits part of its kinetic energy ionizing the molecules and exciting the electrons and the vibrational states near the electronic ground state. The scintillation light yielded in the transitions made by free valence electrons of the molecules has transparent wavelength with respect to the medium due to the energy shift caused by vibrational quanta (Stokes shift). The scintillation efficiency corresponds to the fraction of the deposited energy converted into light and depends on how many light-emitting de-excitation modes are available. The scintillator is optically coupled to a fast PMT with an spectral response in the range of the wavelength of the emitted light. The light is guided to the photomultiplier and converted into photoelectrons that are accelerated and amplified in the dynodes creating a cascade of secondary electrons which is collected at the anode forming the fast pulse signal. In most organic scintillators, the fluorescent light has a decay time τ of around few ns and the prompt fluorescence intensity is given by:

$$I = I_0 exp(-t/\tau) \tag{4.2}$$

This also makes the use of organic scintillators suitable for timing applications in high counting rate environments. It is also known that the time resolution strongly depends on the number of photons emitted [Nis03] according to $\sigma \propto N_p^{-0.5}$, where N_p is the number of photoelectrons. Therefore, the time resolution improves as the number of photoelectrons increase.

4.3.1.2. Performance with heavy ions

Organic scintillators provide excellent time resolutions when measuring relativistic heavy ions due to its large energy deposition and photon emission which is enhanced for thicker devices. However, there exists a compromise between the thickness of the scintillator and the induced energy straggling that should be taken into account. It has been reported resolutions below 10 ps (standard deviation) for a BICRON BC422Q scintillator of 110 ps of rise time, 50 mm length and 0.5 mm thickness coupled to Hamamatsu R4998 PMTs (0.7 ns) irradiated by a ^{40}Ar beam at 95 MeV/u [Nis03]. In this experiment, two leading-edge discriminators, Kaizu and Phillips Discriminator 630 were used to discriminate and reshape the signals. A Kaizu TDC-3781 (Time-to-Digital Converter) digitized the the timing signals. On the other hand, the FRS at GSI is equipped with BC420 fast plastic scintillators of 20 cm length and 5 mm thickness coupled to Hamamatsu R2083 PMTs achieving 150 ps (FWMH) of resolution with fast heavy ions. The current research in fast organic scintillator technology for future nuclear physics experiments where a ToF wall is needed, such as SOFIA (see Sec. 4.1.1), has achieved very promising time resolutions of about 35 ps (FWHM) with a 300 and 600 mm length scintillators of 1 mm thickness (EJ-232) and a rise time below 100 ps, coupled to fast Hamamatsu H6533 PMTs (0.7 ns of rise time) and irradiated by a ^{56}Fe beam of 350 A MeV [Bai10]. The signals were discriminated with an ultra-fast CFD (Constant Fraction Discriminator) developed by Phillips Scientific and the time-of-flight measurement was done with an ORTEC 566 TAC (Time-to-Amplitude Converter). Concerning larger sizes, scintillator-based ToF walls of around 1 m × 1 m of area with time resolutions well below 200 ps (standard deviation) have been already implemented in nuclear physics experiments [LAN; Sch00] to measure the charge and velocity of residues produced in interactions of relativistic heavy-ion beams.

4.3.2. Resistive Plate Chambers

RPCs are gaseous detectors consisting of resistive parallel plates with plane electrodes defining a small gap filled with a proper gas mixture and a high electric field across it. Several large-scale high-energy physics experiments worldwide such as ATLAS [Aie04] and CMS [Abb98] at CERN utilize RPCs as muon trigger with about 1 ns of time resolution and high efficiency detection. Versions of RPC with hundred of μm gas gaps are also used as fast timing detectors (tRPCs) with resolutions better than 100 ps standard deviation in experiments such as HARP [Amm07] and ALICE [Aki09] at CERN, FOPI [Kiš11] and HADES [Bla09] at GSI and STAR [Wan10] at BNL. All these experiments use RPCs developed to detect minimum ionizing particles (MIPs) and after years of intense R&D, the proper working parameters regarding gas mixture, field intensity and irradiation rates have been well established.

4.3.2.1. Working principles of the RPCs

The first RPCs were designed by R. Santonico and R. Cardarelli in 1981 [San81; Car88]. RPCs consists of two parallel plate electrodes defining a gap between them, with at least one of the electrodes made of a high resistivity material of around 10^{12} Ωm (see Fig. 4.6). The gap, whose size may range from hundreds of μm up to few mm, is filled with a highly quenching gas mixture consisting of sulfur hexafluoride (SF_6) used as dielectric gas to control the formation of the avalanche, isobutane (iso-C_4H_{10}) and tetrafluoroethane ($C_2H_2F_4$) as a self-quenching ionization medium. The working principle is that of a gas ionization chamber operated with a high uniform electric field across the gap with typical values of 100 kV/cm for 300 μm gap. The charge carriers released in the ionization of a particle crossing the detector are drifted towards the cathode and the anode. Secondary electrons may be originated by ionizations induced by the primary accelerated electrons. The former are propagated and multiplied forming a Townsend avalanche where the number of total electrons n created along a mean path x is given by the following expression:

$$n = n_0 exp(\alpha x) \tag{4.3}$$

α being the first Townsend coefficient and n_0 the initial number of electrons. The signal induced by the avalanche is read out from strips placed in the electrodes. The resistivity of the layers is a key parameter that determines the response time of the detector. The charge collected in the resistive electrode exponentially decays according to:

$$Q(t) = Q_0 e^{-t/\tau} \tag{4.4}$$

with $\tau = \rho \varepsilon_0 \varepsilon_r$, where ρ is the resistivity of the material, ε_0 is the dielectric constant and ε_r is the permittivity of the material. Therefore, low values of the resistivity lead to shorter relaxation times τ. Owing to the charge carriers in the resistive electrode, the electric field is locally reduced and thus the detector is inhibited during a time of the order of τ, around the spatial point where the avalanche was formed. The electric field is also affected during the progress of the avalanche that creates a space charge effect. If the gain is increased, photons may contribute to the avalanche formation increasing it, and, may lead to the creation of pulses with much higher charge called streamers. For even higher gas-gap voltages, a conductive channel may be created between both resistive electrodes leading to a local discharge with the possibility of spark formation. According to this, RPCs can operate in either two different regimes, avalanche or streamer modes.

4.3.2.2. Avalanche RPCs

The avalanche working mode is preferred for trigger and timing purposes. The average charge of an avalanche pulse is smaller than that of a streamer pulse, thus its counting rate capability is improved (1 KHz/cm^2 for MIPs)

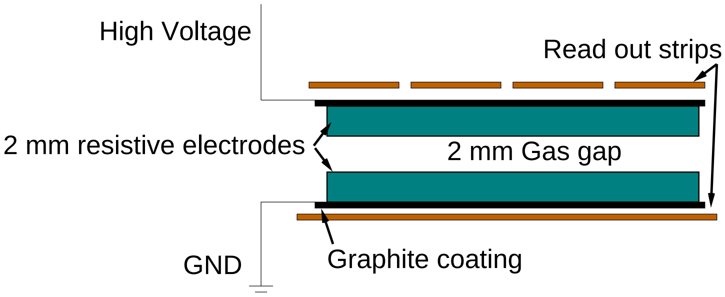

Figure 4.6: Schematic drawing of a 2 mm gap RPC. Conceptual design taken from [San81; Car88].

because the detector needs less time to recover. Furthermore, the presence of streamer pulses may deteriorate the time resolution due to the precursor pulse that often accompanies it. Besides the resistivity of the electrode material, there exists other factors to take into account in order to control the streamer production. The usual gas mixture, containing a small amount of SF_6 which is an excellent electronic quencher, and the control of the applied high voltage are critical parameters concerning the streamer production.

While trigger RPCs, deployed in large-area experiments to trigger MIPs, usually consists of one gas-gap of around 2 mm of thickness with electric fields of the order of 50 kV/cm and time resolutions of around 1 ns, tRPCs are assembled in narrow multi-gap (200-300 μm) structures [Zeb96; Fon00], as shown in Fig 4.7, improving its efficiency according to $\epsilon = 1-(1-\epsilon_g)^n$, where n and ϵ_g are the number of gaps and its efficiency, respectively. Efficiencies of 90%-94% has been attained with these tRPCs measuring MIPs [Fon02]. Considering independent measurements in each gap, the time resolution is improved following:

$$\sigma = \frac{\sigma_n}{\sqrt{n}} \tag{4.5}$$

tRPCs operated at about 100 kV/cm of electric field yield time resolutions around 45 ps (standard deviation) [Amm10] for MIPs. Due to the low average charge of avalanche pulses the use of low-noise high-frequency front-end electronics is compulsory to preserve the timing properties of the tRPCs. This is also necessary in order to discriminate the avalanche precursor of the streamer pulses. In the present work we will focus on the study of tRPCs for the detection of fast ions.

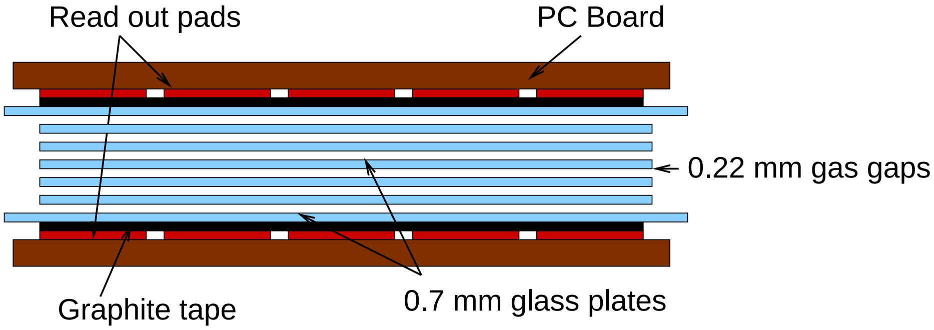

Figure 4.7: Schematic drawing of a multi-gap tRPC.

4.3.2.3. Streamer RPCs

In applications and experiments where the counting rate and timing capabilities does not represent a limiting factor, the use of the streamer mode really simplifies the read out of the pulse and therefore preamplifiers are not needed. With high electric fields of around 40 kV/cm, streamer mode RPCs reach around 99% of efficiency with MIPs but with relatively low counting rate capability (few hundreds Hz/cm^2). Experiments such as BABAR at SLAC [Zal00], OPERA at LNGS [Dus01] or ARGO at YangBaJing [Bac00] utilize detection systems based on streamer mode RPCs.

4.4. Detection of relativistic heavy ions with RPCs

Owing to its excellent timing properties and efficiency values, recently it has been proposed the use of RPCs as one of the options for the construction of the ion time-of-flight wall (iToF) for the R^{3}B experiment (see section 4.1.2). The use of RPCs for the detection of relativistic heavy ions, and the information concerning its performance under such conditions is scarce [Cas12b; Cab09]. The much larger energy deposition of relativistic highly charged ions with respect to MIPs and the rate capabilities are key parameters that must be investigated in order to find a proper working point to preserve the outstanding properties of the tRPCs. Thus, we started few years ago a dedicated R&D program in order to construct and characterize tRPCs prototypes dedicated to the detection of heavy ions.

The aim of this section is to study the behavior of such prototypes under relativistic ion irradiation. We will describe the construction of the tRPCs and the different analog front-end electronics developed for these prototypes.

This section is also dedicated to fully describe the performance of tRPC prototypes studied in different experiments with heavy ions and electrons: detection efficiency and time resolution varying different parameters such as gap voltage or gas mixture. The rate limit for ions above which the time resolution degrades is also a key point that will be studied further in this chapter. For this purpose we used a dedicated data acquisition systems which features and characteristics are also explained in this section.

4.4.1. Development and construction of tRPC prototypes

All the prototypes constructed and tested in this work were adapted to the detection of heavy ions at relativistic energies. One of the most relevant issues when detecting heavy ions is the energy and angular straggling induced by the layers of matter. In time resolution terms, this straggling induces a broadening of the time distribution, and therefore it degrades the measurement. For instance, the energy and angular straggling induced to a ^{238}U ion at 400 A MeV after crossing 2 mm of soda-lime glass is around 15 A MeV and 0.5 mrad, respectively. We used the AMADEUS code to evaluate these quantities [AMA]. Moreover, ions could be stopped before passing through the detector if the energy loss is high enough. Thus, all the prototypes are optimized with the minimum amount of matter possible in its active detection area.

The first small prototype (hereafter RPC-11) was designed as a symmetric double gas-gap structure using four soda-lime glass plates of $6 \pm 2 \times 10^{12} \Omega m$ of resistivity, and, 15 cm × 7 cm of area and 1 mm thickness (see upper panel of Fig. 4.8). Nylon fishing line of 300 μm was used as spacer to create the gas-gap. Two strips, made of self-adhesive copper tape of 150 mm length, 20 mm width and 2 mm pitch, were situated in each one of the three planes defined by the glass stack assembly acting as electrodes and signal pick-up. The stack was placed in between two G10 plates of 2 mm thickness to pack the plates and provide the assembly an additional rigidity. The high voltage was supplied through the middle electrode while the external ones acted as the ground reference. The signal was picked-up from both extremes of the strips, previously decoupled from the high voltage. During the measurements only one of the strips was active and the prototypes were placed inside an aluminum box to ensure the gas tightness and flow. We also constructed a single gas-gap version of the RPC-11 prototype (RPC-22).

A more optimized small prototype for timing measurements (RPC-25) was constructed with two stacked and aligned one-strip (20 mm width and

15 cm long) double-gap (300 μm) RPC structures made of 15 cm × 7 cm glass plates of 1 mm thickness, separated by few cm as shown in the lower panel of Fig. 4.8. The construction of each individual assembly was identical to the previous prototypes but here the G10 plates were removed and the glass plates were glued to pack the glass plates, and, two thin Kapton windows were made in the gas-tight aluminum box to reduce the amount of layers of matter, and thus, the energy and angular straggling.

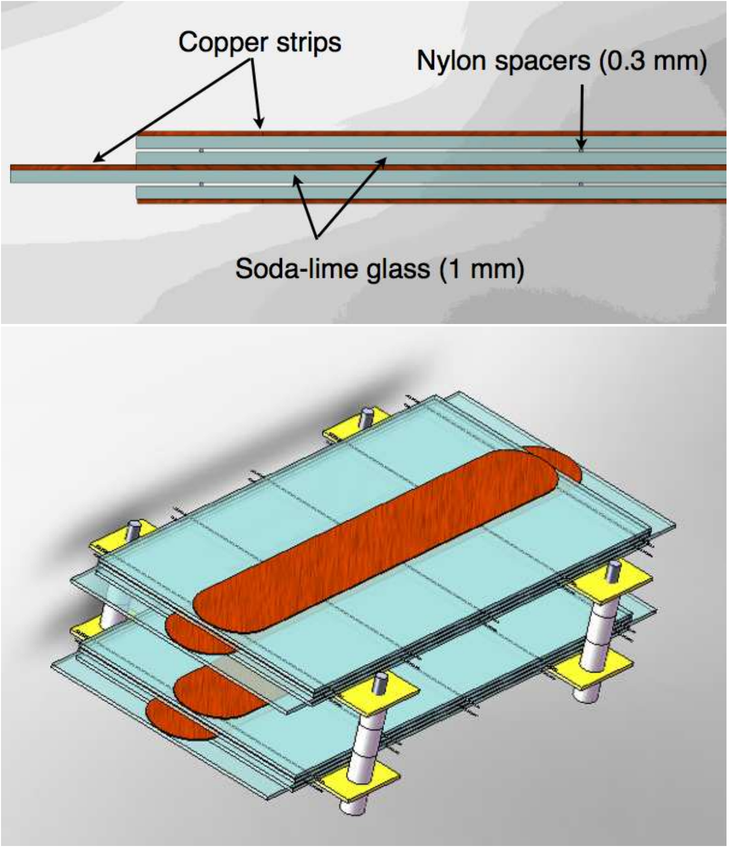

Figure 4.8: Upper panel: Lateral view of the schematic representation of a small double gas-gap prototype. Lower panel: Top view of two double gas-gap prototypes with a single strip.

Going a step further in the design, a large-area prototype (RPC-30) was constructed with only one gas-gap of 300 μm defined by a self-tight soda-lime glass structure (see Fig. 4.9). This self-contained multi-strip tRPC of 40 cm × 20 cm was assembled with two soda-lime glass plates of 1 mm thickness, glued in the edges to seal the gas-gap and ensure its tightness. The 5 strips of 20 mm width that define the active detection area were made of self-adhesive copper tape, glued to the external side of each plate. The induced signals were read out from both extremes of each strip. The HV was distributed to the copper strips in one of the plates of the module while the other plate was the ground reference. Taking into account that the range of ^{238}U or ^{208}Pb ions at 400 A MeV in soda-lime glass is about 15 mm, this one-gap structure represents an ideal option for the construction of the real-size iToF modules owing to the compromise between thickness (1 mm) and robustness of the glass plates. Furthermore, the total gas volume per module is drastically reduced corresponding to the active detection volume (about 100 cm^3). Two single-gap self-contained structures were stacked and placed in an aluminum structure making the strips coincide to perform time measurements between them (see Fig. 4.10). In addition, a single-strip version of this prototype was constructed (RPC-40) with two one-gap (300 μm) structures of 40 cm$\times$ 7 cm constructed with 1 mm soda-lime glass plates. Both structures were separated by 5 cm.

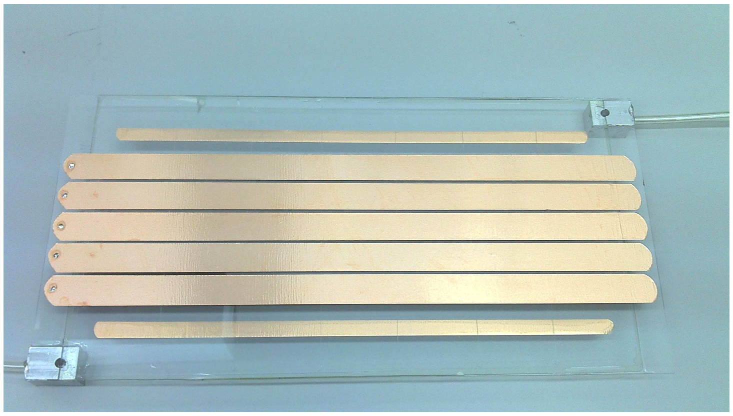

Figure 4.9: Single-gap self-contained multi-strip tRPC.

4.4.2. Analog front-end electronics (FEE)

The development of an appropriate pre-amplification stage capable to deal with the high-frequency bandwidth signals produced by the tRPCs (GHz) is a key parameter in order to obtain high-quality timing measurements. Also, the gain have to be adapted to the relatively low charge of the avalanche pulses and the wide nuclear charge range of the ions we want to detect. The quality and behavior of the electronic components and its complex impedance in the bandwidth range of interest is also another critical issue that complicates the design of the front-end electronics (FEE).

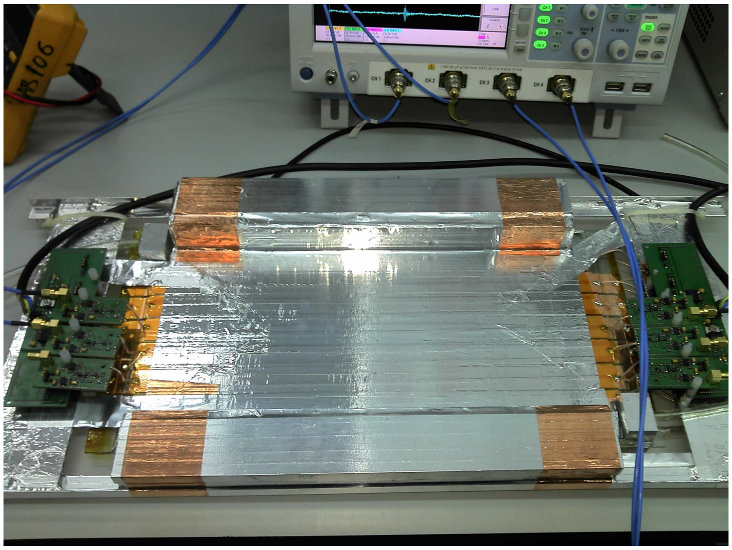

Figure 4.10: Two identical RPC structure shown in Fig. 4.9 assembled in an aluminum support.

The signal induced in the strip is decoupled from the HV and fed into the FEE board. A RCL filter is implemented in order to dump the highest frequencies down to hundreds of MHz to accommodate the signal to the amplifying stage (around 1 GHz), and, match the impedance between the latter and the strip. For the amplifying stage we implemented different solutions that we tested with the different prototypes. For the double-strip double-gap prototypes (RPC-11 and RPC-22) we used two commercial trans-impedance amplifiers in cascade: GALI-S66 and MAXIM-4223 having a bandwidth up to 1 GHz. The rise time of the amplified output signals was about 12 ns and the noise level was below 20 mV. On the other hand, since the RPC-25 prototype was optimized for time resolution measurements, the amplifier stage was designed in order to reduce the rise time of the signal and adapt it to our specific data acquisition system. For this prototype we used a commercial wide-band transistor BFR92A (5 GHz) and MAXIM-4224 current amplifier. The signals amplified by this FEE had a rise time of around 4 ns and a noise level below 10 mV. In all these prototypes , the output signals were transmitted using LEMO-00 coaxial cables having 50 Ω of impedance.

The RPC-30 and RPC-40 prototypes were equipped with a slightly different FEE cards. To improve the signal/noise ratio the MAXIM-4224 chip was replaced by the OPA657 trans-impedance amplifier with 1.6 GHz bandwidth and a gain up to 44 dB. The output signal, having a noise level was below 5 mV and a rise time of 4 ns, was transmitted using a specific semi-rigid coaxial cable with SMA (SubMiniature version A) connectors featuring up to 3 GHz of bandwidth and 50 Ω of impedance. The selection of such electronic system (FEE + cable) was proposed in order to preserve the quality of the signal and its timing properties as well as to adapt its amplitude and width to our acquisition system input.

4.4.2.1. FEE calibration

The charge output of the FEE is a key parameter that is commonly used to correct the time-walk (slewing) effect on time-of-flight measurements. Time-walk arises from the variation in the height of the pulses and it is especially critical for small charges or amplitudes. Therefore, a charge calibration is mandatory in order to establish the response and limits of our FEE. The charge and amplitude calibration was done feeding the card with a fast pulse of variable amplitude (from 10 up to 300 mV) and width (from 4 up to 13 ns), and, a rise time of around 2.5 ns (400 MHz). These fast signals were constructed using a passive differentiator circuit connected at the output of a square-pulse generator. An oscilloscope with 1 GHz of bandwidth and a sampling speed of 5 Gs/s was used to digitize the full pulse (see Fig. 4.11).

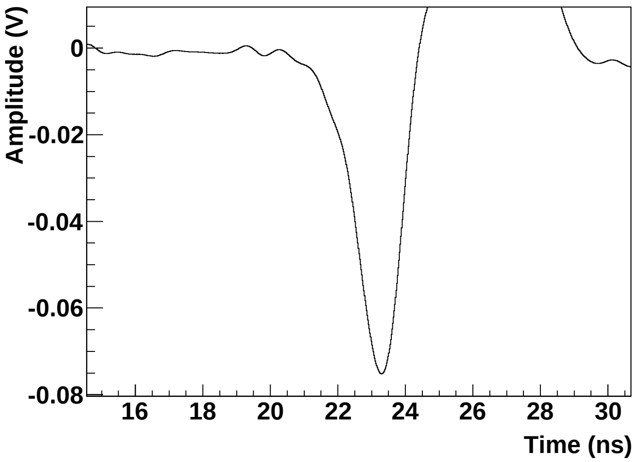

Figure 4.11: FEE calibration pulse digitized in the oscilloscope.

The amplitude and charge calibration curves of the RPC-30 prototype FEE (transistor+OPA657) are shown in Fig. 4.12 and Fig. 4.13, respectively. One can see that the FEE input and output amplitudes show a linear correlation from 10 up to 60 mV with a gain factor about 5.5 (slope). The FEE starts to saturate at around 100 mV of input amplitude and the gain factor is progressively reduced down to 2.2 at 650 mV. Concerning the charge calibration, a lineal correlation was found in the range from 0 to 16 pC of input charge with a gain factor of around 4. However, the entire range (from 0 to 150 pC) could be fitted to a second order polynomial function showing a slight saturation regime.

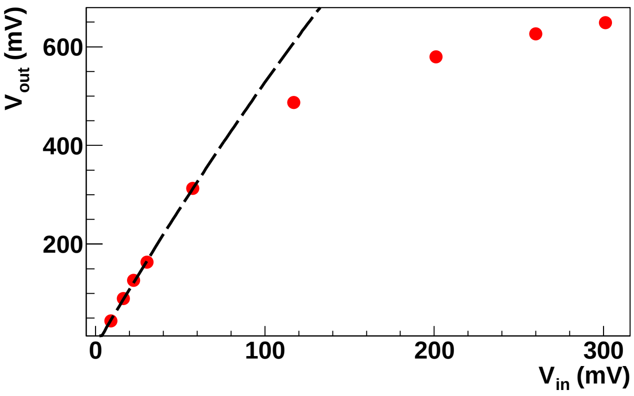

Figure 4.12: Transistor+OPA657 FEE amplitude calibration curve (See text for details).

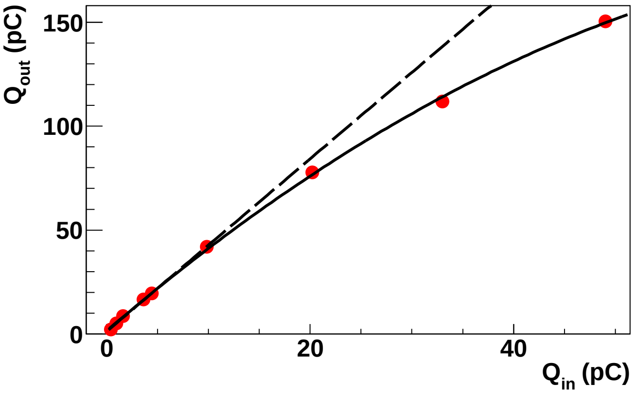

Figure 4.13: Same as Fig. 4.12 but for charge.

Similarly, we also calibrated the FEE installed in the RPC-25 prototype (transistor+MAXIM-4224) using the same procedure explained before. The amplitude calibration curve of this FEE represented in Fig. 4.14 show a correlation between the input and output amplitudes with a gain factor of around 20. Compared to the transistor+OPA657 FEE, the saturation effects seems to be smoother and the curve could be fitted to a second order function in the entire range. The slight change in the slope of the amplitude curve around $V_{in} = 40$ is an artifact caused by the change of the voltage range of the pulse generator. On the other hand, a linear correlation with a gain factor of about 22 was found between the charge of the input and output pulses (see Fig. 4.15).

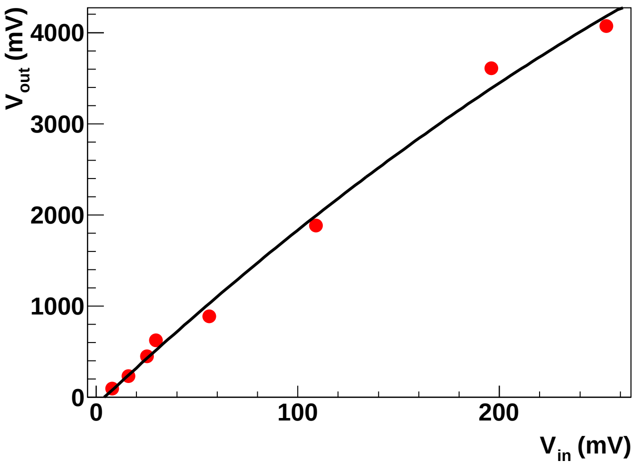

Figure 4.14: Transistor+MAXIM-4224FEE amplitude calibration curve (See text for details).

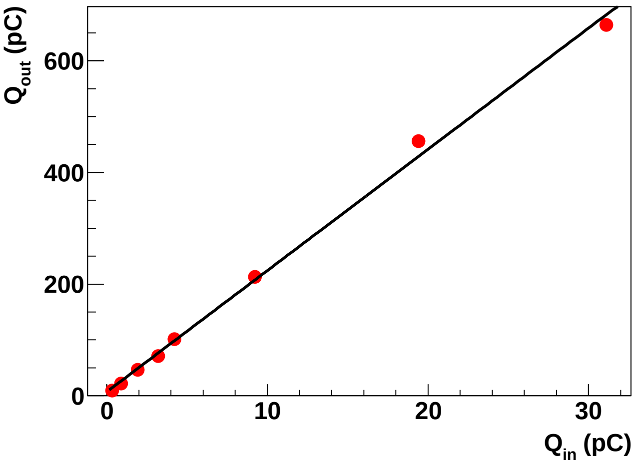

Figure 4.15: Same as Fig. 4.14 but for charge.

In conclusion, this characterization of the response the FEE will allow us to extract quantitative results of the measurements made with the different prototypes with different FEE boards and therefore compare them.

4.4.3. Experimental setups

Since the experimental tests were done bombarding the prototypes with heavy ions at relativistic energies, the determination of the performance of the tRPCs and its characterization requires a capable trigger system with high efficiency for the detection of heavy ions to unambiguously identify particles traversing the detector. BICRON BC420 plastic scintillators of 120 mm × 20 mm and 10 mm thickness and EJ-232 (Eljen Technology) scintillators with a rise time well below 100 ps and a dimension of 140 mm × 30 mm and 1 mm thickness were used as external trigger system to determine the intrinsic detection efficiency and time resolution of the tRPCs prototypes. The scintillators were coupled to fast Hamamatsu H6533 PMTs, with 0.7 ns of rise time, allowing read out from both extremes. The trigger system scheme and the layout of the scintillators and the tRPC are shown in the upper and lower panels of the Fig. 4.16, respectively. During the tests, the tRPC prototypes to be studied were placed in the beam line surrounded by two plastic scintillator detectors (two BC420 or two EJ-232) and the trigger was given by the coincidence of the signals of the four photomultipliers in temporal coincidence after being discriminated. Therefore, a beam particle traversing the scintillators and the tRPC was identified and clearly separated from the noise level. To reduce systematic uncertainties associated to the setup geometry the transversal dimension of the trigger detector was aligned and adapted to the width of the prototypes active strip (20 mm).

4.4.4. Data acquisition systems

The data acquisition systems we have used to digitize and analyze the signal pulses of the tRPCs were based on the standard VME bus. The hardware control was made by means of a CES RIO3 processor and a TRIVA module controlled the dead-time of the acquisition. The triggers, given by the coincidence of the four signals of the PMTs, were managed and constructed using standard NIM electronic modules (Fan-In Fan-Out, leading-edge discriminator, octal gate generator and coincidence). If the trigger is accepted, then is provided to the TRIVA module allowing the read out of the data, controlled by the MBS (Multi-Branch System) software. To fully digitize the signals coming from the PMTs and the FEE of the tRPCs we used VME flash-ADC (fADC) boards based on the MATACQ32 chip with 2 GS of sampling speed

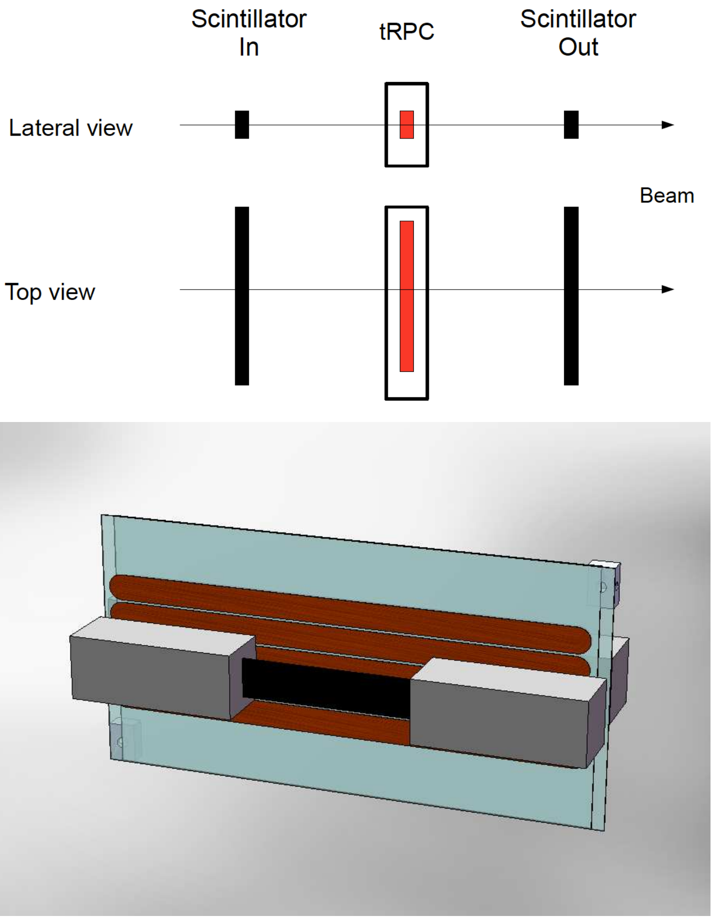

Figure 4.16: Upper panel: Scheme of the scintillator-based external trigger for efficiency and timing measurements. Lower panel: Layout of the tRPC placed in between two scintillation detectors.

developed by M2J [M2J]. The digitization of the pulse allowed us to investigate the signal formation in the tRPC and study its characteristics. The efficiency and streamer production was determined by means of a comprehensive pulse shape analysis. However, the time resolution of this system is limited to 500 ps by the sampling speed of the fADC modules and the acquisition rate is restricted to few hundreds of Hz. A scheme of this system is presented in Fig. 4.17 and the shape of a pulse of the transistor+OPA FEE registered by the fADC is shown in Fig. 4.18.

To overcome this problem, an specific and more optimized data acquisition system is required for timing measurements. As a solution, we utilized the compact TACQUILA board, with a dedicated FEE coupled to it

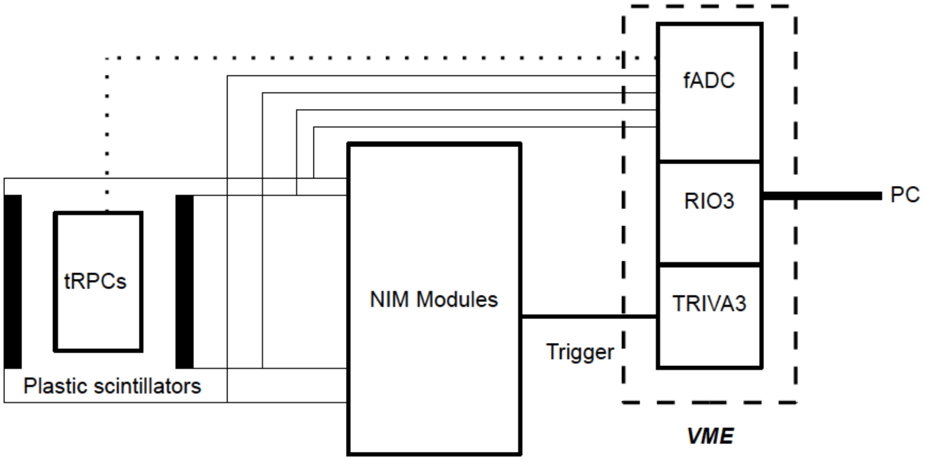

Figure 4.17: Scheme of the fADC-based data acquisition system.

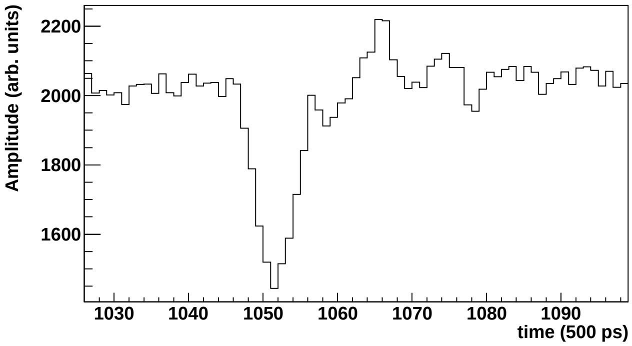

Figure 4.18: Typical pulse registered with fADC data acquisition system. The pulse corresponds to a ^{136}Xe ion detected in the RPC-30 prototype. Each channel in the y and x axis corresponds to 2 mV and 500 ps, respectively.

(STAR), developed for timing measurements with tRPCs in the FOPI experiment [Koc05]. This board consists of 16 channels with differential inputs of 50 Ω of impedance and a TAC ASIC (Time-to-Amplitude Converter) integrated chip for timing measurements in each one of them. A common threshold value for each channel can be set in order to discriminate the signals according to its amplitude. Additionally, the charge of the pulses can be digitized with a QDC piggy-back board. The bandwidth of the complete system is around 1 GHz and its intrinsic time resolution about 25 ps [Sch04].

In this case, the hardware and dead time control was made with the RIO3 and TRIVA boards, but, the triggers were managed by a VULOM module instead of the NIM logic trigger used for the fADC and distributed by means of a TRIDI module. The data read out (MBS) was made with a SAM board, specifically designed for this kind of systems, sending the data trough a differential bus (GTB) to a computer running under LynxOS operating system (see Fig. 4.19).

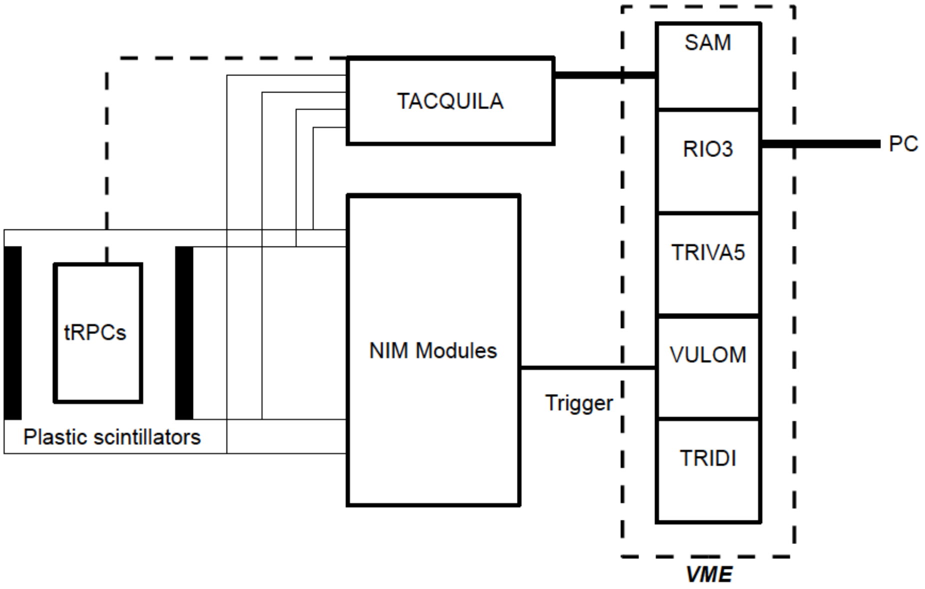

Figure 4.19: Same as Fig. 4.17 but for TACQUILA system.

The signals of the detectors and a internal 40 MHz clock provided the *start* and *stop* signals for each TAC, respectively. Therefore all signals must fit within a 25 ns time window. This will be improved in the future in an advanced TACQUILA design, which includes an extra channel to synchronize the timing of the channels, beyond the natural 40 MHz clock of the original design. This is important in order to fit all the physics cases in the appropriate time window. The time signal provided by the TAC is digitized in a 12-bit ADC (4096 channels) and, simultaneously, the 10-bit QDC (1024 channels) continuously integrates the charge of the signal pulse. The QDC resets after a pre-fixed time. When a trigger is accepted, the data is registered and monitored by the acquisition. Each TACQUILA channel was calibrated in time and charge and the QDC pedestals were evaluated and subtracted in the measurements. The time calibration was done by dividing the number of channels spanned by each ADC spectrum by 25 ns. Concerning the charge calibration (see the plot in Fig. 4.20), we fed TACQUILA with the same pulses we used for the calibration of the FEE boards (see detailed description at Sec. 4.4.2), which allowed us to determine the correlation between input pulse charge, Q_{in}, and QDC channel, Q_{TAC}.

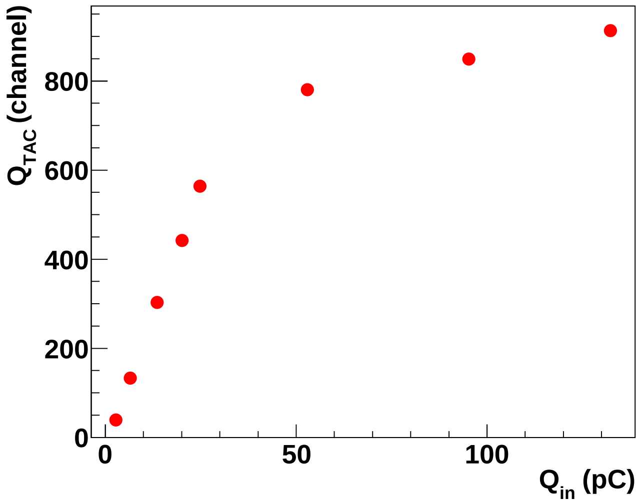

Figure 4.20: TACQUILA charge calibration curve. See text for details.

In addition, the intrinsic time resolution of the FEE (transistor + OPA657) + TACQUILA system was also determined to evaluate its contribution to the time-of-flight measurements. In order to do this, we used two different FEE boards fed with the same signal with their output directly connected to TACQUILA. The resolution was determined with the time difference between both calibrated channels yielding a value of $\sigma_{elec} = 48/\sqrt{2} = 34\ ps$ (see Fig. 4.21).

4.4.5. Dedicated experiments

In order to investigate the performance of the tRPCs in a proper scenario we conducted several experiments with relativistic ions with different nuclear charges at GSI (Germany), and, with electrons at ELSA (CEA-DAM, France) and ELBE (HZDR-Rossendorf, Germany). We will explain in this section the different experiments carried out to characterize the FEE and the tRPC prototypes in efficiency and time resolution terms and determine its optimum working point. A survey of the different experiments and its main features is presented in Table 4.1.

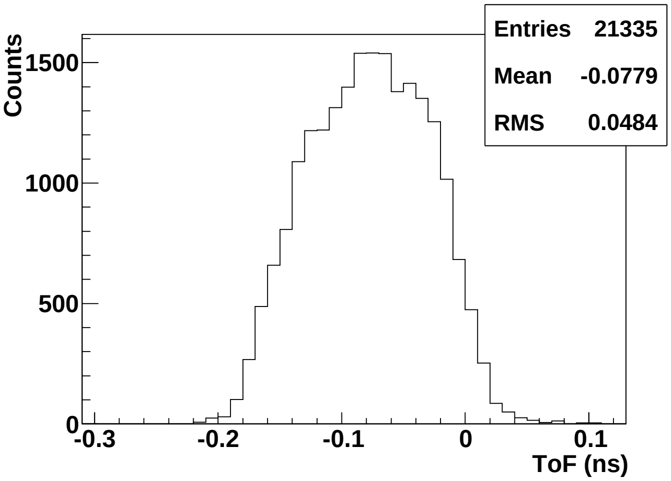

Figure 4.21: Distribution of the time difference between two TACQUILA channels fed with the same pulse amplified by two different FEE boards.

Beam	Energy	Prototype	Rate	Trigger system
^{12}C	700 A MeV	RPC-11	tens of Hz/cm^2	2 BC420+H6533
^{64}Ni	500 A MeV	RPC-11/RPC-12	tens of Hz/cm^2	2 BC420+H6533
^{238}U frag.	750 A MeV	RPC-11	tens of Hz/cm^2	2 BC420+H6533
^{136}Xe	560 A MeV	RPC-30	2-5 Hz/cm^2	2 EJ-232+H6533
^{238}U	1 A GeV	RPC-25	10 Hz/cm^2	self-trigger
e$^-$ bunches	10 MeV	RPC-25	5 Hz	1 EJ-232+H6533
Single e^-	40 MeV	RPC-40	up to 13 MHz	self-trigger

Table 4.1: Experiments performed with different tRPC prototypes.

In experiments conducted at GSI the RPC-11 and RPC-12 prototypes were irradiated with a ^{12}C and a ^{64}Ni beams at 700 and 500 A MeV of energy, respectively, with a repetition rate of few tens of Hz/cm^2 [Cas12b]. Furthermore, another experiment was conducted where RPC-11 prototype was bombarded with medium-mass fragments produced in the fragmentation of ^{238}U ions at 750 A MeV [Ayy12]. In these experiments, we used a external trigger with full efficiency in the detection of heavy ions, composed by two BC420 plastic scintillators (10 mm thickness) coupled to two Hamamatsu H6533 PMTs. The RPCs were supplied with a gas mixture composed of 90% of $C_2H_2F_4$ and 10% of SF_6. The signals from the tRPCs (GALI-S66+MAXIM4223 FEE) and the PMTs were fully digitized in our fADC-based acquisition.

The performance of the RPC-30 prototype, composed by two single-gap multi-strip modules, was measured also at GSI by bombarding the prototype with a ^{136}Xe beam at 560 A MeV with a repetition rate below 30 Hz and a spill of 5 s of duration. The signal time and charge distributions were digitized using TACQUILA board. Because of the synchrotron operation mode at such a low rate, this was largely fluctuating from 4 up to 50 Hz between different spills. A 1 Hz calibration trigger implemented in the TACQUILA acquisition system was used to monitor the beam fluctuation at each second, and moreover, allowed us to determine two different rate per unit area intervals considering a cross section for the beam spot of around 3 cm^2. Both modules of the prototype were surrounded by an external trigger made of two EJ-232 plastic scintillators of 1 mm thickness coupled to two PMTs as explained in the section 4.4.1. The trigger system was aligned with the central strips of both modules defining the active detection zone. We used a gas mixture composed by 90% of $C_2H_2F_4$ and 10% of SF_6, without iso-C_4H_{10}. The prototype was operated in a high voltage (HV) plateau ranging from 2700 up to 3400 V. Another different beam test was done irradiating the RPC-25 prototype with a beam of ^{238}U at 1000 A MeV with a rate of 10 Hz/cm^2. In this experiment the coincidence of the four signals given by FEE channels of both modules of the RPC-25 prototype provided the trigger for the TACQUILA acquisition system. The detector was operated at 2800 V with the same gas mixture we used in the previous experiments.

The RPC-25 was also tested using an electron beam at ELSA facility [Par]. 10 MeV mono-energetic electrons were delivered in bunches (about 10^4) of a few ps length. According to the features of such beam, we simulate the energy lost by the heavy ions in the RPC by means of many electron losses in the same spot. In such a short time, each bunch induces a unique signal in each tRPC module whose charge is correlated with the number of electrons of the bunch that can be modulated using a polarizer allowing us to vary the beam intensity in two orders of magnitude. A low repetition rate of 5 Hz was considered during all the experiment. In this case, the detection trigger was constructed using the temporal coincidence of the four signals provided by both modules of the RPC-25 (two signals per module) and the signals of a thin plastic scintillator (similar to the one used in the ^{136}Xe experiment) placed upstream of the tRPCs. The signals were digitized using the TACQUILA board. The gas mixture we used in this experiment was composed by 90% of $C_2H_2F_4$ and 10% of SF_6 and the tRPCs were operated at different voltages and beam intensities during the measurements.

At the ELBE facility, the RPC-40 was irradiated with a single electron beam of 40 MeV and up to 13 MHz of repetition rate. We used three different gas mixtures completely free of iso-butane, just varying the proportion of SF_6. The chamber was operated at 3200 V.

4.4.6. Working parameters

In this section we present the results of the experiments we performed with the different prototypes. The main working parameters of the tRPCs, efficiency and time resolution, are discussed and compared to extract conclusions about its performance under such conditions.

4.4.6.1. Time resolution

The time resolution of the RPC-30 prototype under ^{136}Xe irradiation was obtained from the ToF measurement between the central strip of both tRPCs of the prototype, assuming both modules with the same time resolution. Considering the resolution of the time-of-flight as:

$$\sigma^2_{ToF} = \sigma^2_{RPC1} + \sigma^2_{RPC2} \tag{4.6}$$

where σ^2_{RPC1} and σ^2_{RPC2} are the time resolutions of the first and the second tRPC modules of the RPC-30 prototype. Assuming both modules with the same time resolution ($\sigma^2_{RPC1} = \sigma^2_{RPC2} = \sigma^2_{RPC}$), we obtain:

$$\sigma_{tRPC} = \frac{\sigma_{ToF}}{\sqrt{2}} \tag{4.7}$$

The plastic scintillator placed upstream of the prototype was used to determine the position of the beam and reject possible contaminants. The position, shown in 4.22, was defined as the time difference between the signals read out from both PMTs of this scintillator, T^1_L and T^1_R. Only the beam particles between both dashed lines were considered. The relative angle of incidence, defined as the difference between the position measured in both scintillators, was also determined to check the alignment of the particles with the beam direction (see Fig. 4.23).

Considering these conditions, we calculated the time-of-flight between both tRPCs, and therefore, the time resolution of each module was given by:

$$\sigma_{tRPC} = \frac{T^{RPC1}_L - T^{RPC2}_L}{\sqrt{2}} \tag{4.8}$$

where T^{RPC1}_L and T^{RPC2}_L are the times of the left channels of the central strips of the first and the second tRPC digitized in TACQUILA. At 2800 V, a

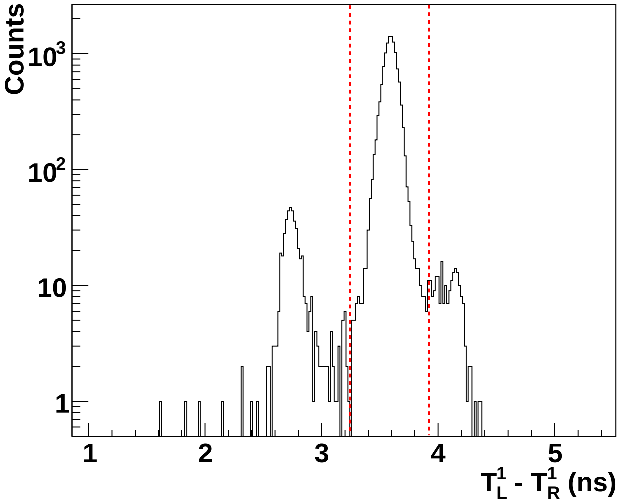

Figure 4.22: Position of the ^{136}Xe beam in the first scintillator.

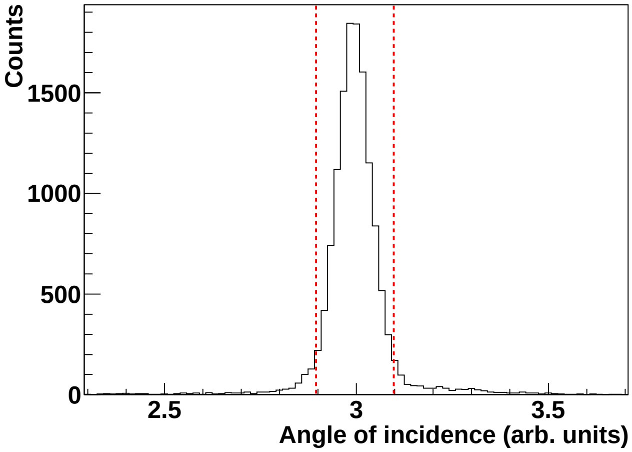

Figure 4.23: Relative angle of incidence of the ^{136}Xe ions measured by the plastic scintillators. The narrow shape of the distribution indicates the collimation of the beam.

time resolution of $\frac{70\ ps}{\sqrt{2}} = 49\ ps$ (1.5-σ [2]) was achieved with an irradiation rate of around 1-2 Hz/cm^2 (see Fig. 4.24). This resolution was slightly improved

---

[2] the Gaussian distribution was fitted in a range of 1.5-σ around the mean value

by correcting the existing time-walk effect due to the variation of the height of the pulses, reaching a time resolution of around $\frac{67\ ps}{\sqrt{2}} = 47\ ps$ (1.5-σ). To do this, we represented the time of flight as a function of the charge of the pulse of the left channel of the second RPC (Q_L^{RPC2}). In the upper right panel of the Fig. 4.24 one can see the slight correlation due to low amplitude signals that was corrected using a second order polynomial function. It is worth pointing out that the tails at $3-\sigma$ amounted to 25% due to an artifact caused by a incorrect operation of the detector probably caused either by the amplification of the FEE or the proper setup of the TACQUILA acquisition. The events of the tail at the right side of the distribution increases with the applied voltage and rate, having a value of 35% at 3400 V and 3-5 Hz/cm^2, respectively. Nevertheless, in the two dimensional plots of the right panels of Fig. 4.24 one can see that these artifact events are clearly distinguishable (around 0.5 ns in the y axis of the plot of the lower panel) from the physical events of the ToF distribution and these only affect to the determination of the time resolution beyond 1.5-σ, and, to the time-walk effect correction with respect to the charge of the pulse measured in the left channel of the first RPC (Q_L^{RPC1}). A dedicated investigation is being carried out in order to identify and solve such problems.

We investigated also the effect of the high voltage in the time resolution under a constant irradiation rate. As can be seen in the Fig. 4.29, the time resolution (σ_{RPC}) strongly depends on the applied high voltage. There exists a minimum value at 2800 V of 47 ps and the resolution degrades as the voltage is increased, reaching a value of 60 ps (1.5-σ) at 3400 V. For lower voltage values, the time resolution slightly increases due to the reduction on the pulse amplitude, having around 51 ps (1.5-σ) at 2700 V. These time resolution values were determined after each respective time slewing corrections.

We also present in Fig. 4.26 the linear correlation between the applied voltage and the mean value of the signal charge distribution. In this plot, the value and its uncertainty corresponds to the mean and the RMS of the charge distribution, respectively. This give us a mean value of the signal charge for the best time resolution measurement (2800 V) of 5.5 pC. There exist a compromise between the amplification of the signal by increasing the high voltage and the time resolution. Higher amplifications may lead to higher pulse amplitudes, thus, better values of the time resolution, but, also higher streamer production. Unfortunately, due to the low charge resolution of TACQUILA QDC, the avalanche pulses could not be separated from streamers in this case, and therefore, we assumed that an increasing contribution of the latter led to a degradation of the time resolution. In conclusion, a high voltage plateau was found between 2700 and 2900 V where the tRPC can be safely operated reducing the streamers contribution. The amplification of the signal

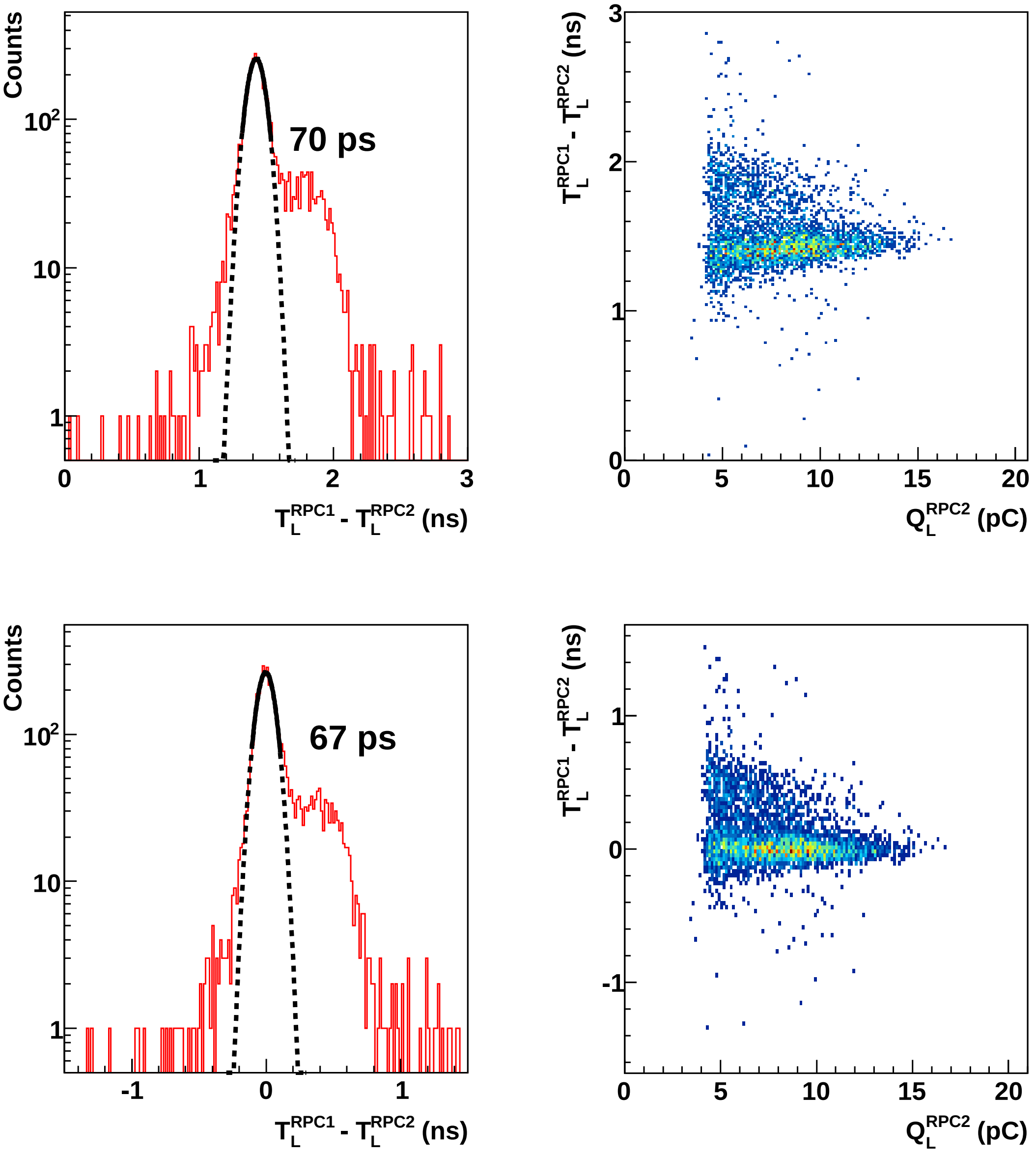

Figure 4.24: Left panels: Time of flight distribution of ^{136}*Xe ions measured between both modules of the RPC-30 prototype operated at 2800 V and a rate of 1-2 Hz/cm*^{2} *before (upper panel) and after (lower panel) the slewing correction. Right panels: Time of flight measured in the RPC-30 prototype as a function of* Q_L^{RPC2} *before (upper panel) and after (lower panel) slewing correction.*

can be made also increasing the gain of the amplification stage of the FEE which would in principle improve the time resolution without increasing the streamer production.

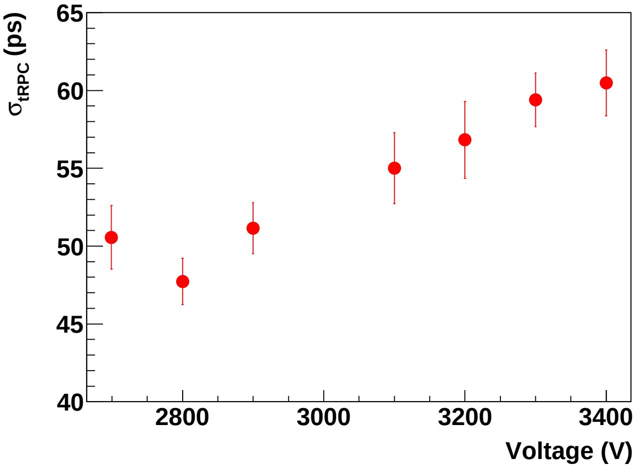

Figure 4.25: Time resolution (1.5-σ) of the RPC-30 prototype as a function of the applied voltage for ^{136}Xe at 560 A MeV and 1-2 Hz/cm^2 of irradiation rate.

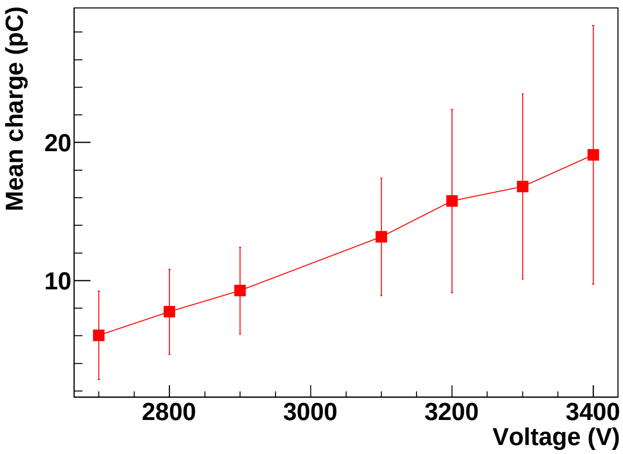

Figure 4.26: Mean value of the signal charge distribution as a function of the applied voltage for ^{136}Xe at 560 A MeV.

Time resolution was measured also in the experiment conducted at the FRagment Separator (GSI) where the RPC-25 prototype was irradiated ^{238}U beam at 1000 A MeV with a rate of 10 Hz/cm^2. This rate represents a substantial increase in energy deposition with respect to ^{136}Xe considering the nuclear charge of each ion. To reduce to the minimum the rate per area unit, the beam was defocused using the FRS spectrometer and only ^{238}U particles impinging in the center of the strips of both modules of this prototype were considered (see Fig. 4.27). The position was calculated with the time difference between the signal measured at both ends of the strip of each module (RPC1 and RPC2).

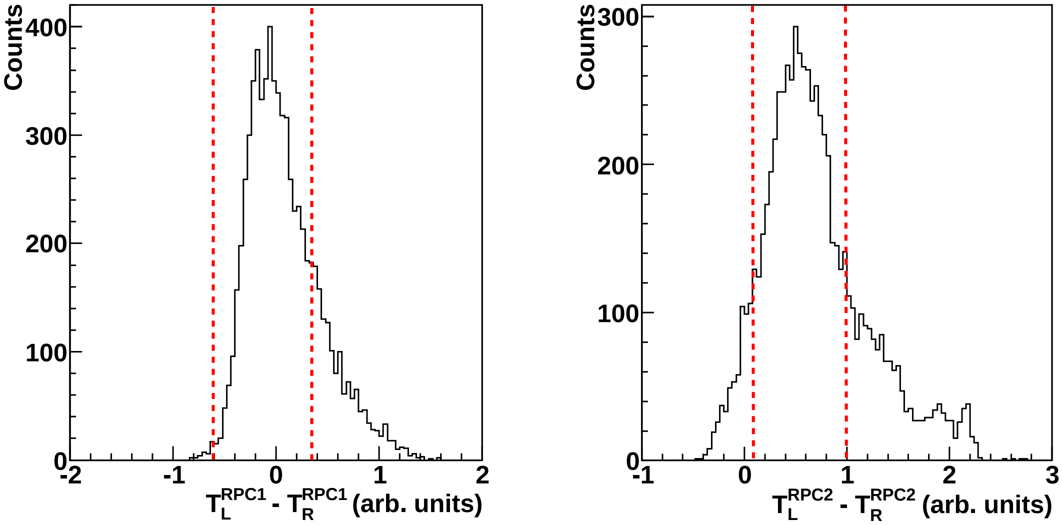

Figure 4.27: Left panel: Position of the ^{238}U beam in the first RPC. Only events between both dashed lines were considered. Right panel: Same as left panel but for the second RPC.

We followed the same procedure utilized before to determine the time of flight between both modules of this prototype. According to the equation 4.8, a time resolution of $\frac{97}{\sqrt{2}} = 69$ ps (1.5-σ) was obtained after slewing correction, with a value of a mean value of the signal charge distribution of 8.6 pC. Figure 4.28 show the time of flight distributions measured between the left FEE channel of both modules of the RPC-25 prototype and its correlation with the charge of the signal, Q_L^{RPC1}. The tails at $3 - \sigma$ amounted to 10%.

The time resolution of the RPC-25 prototype was also measured with electrons bunches simulating the energy deposition of an ion with a given atomic number. We measured the time difference between the two tRPC modules and each of the modules with respect to the plastic scintillator to

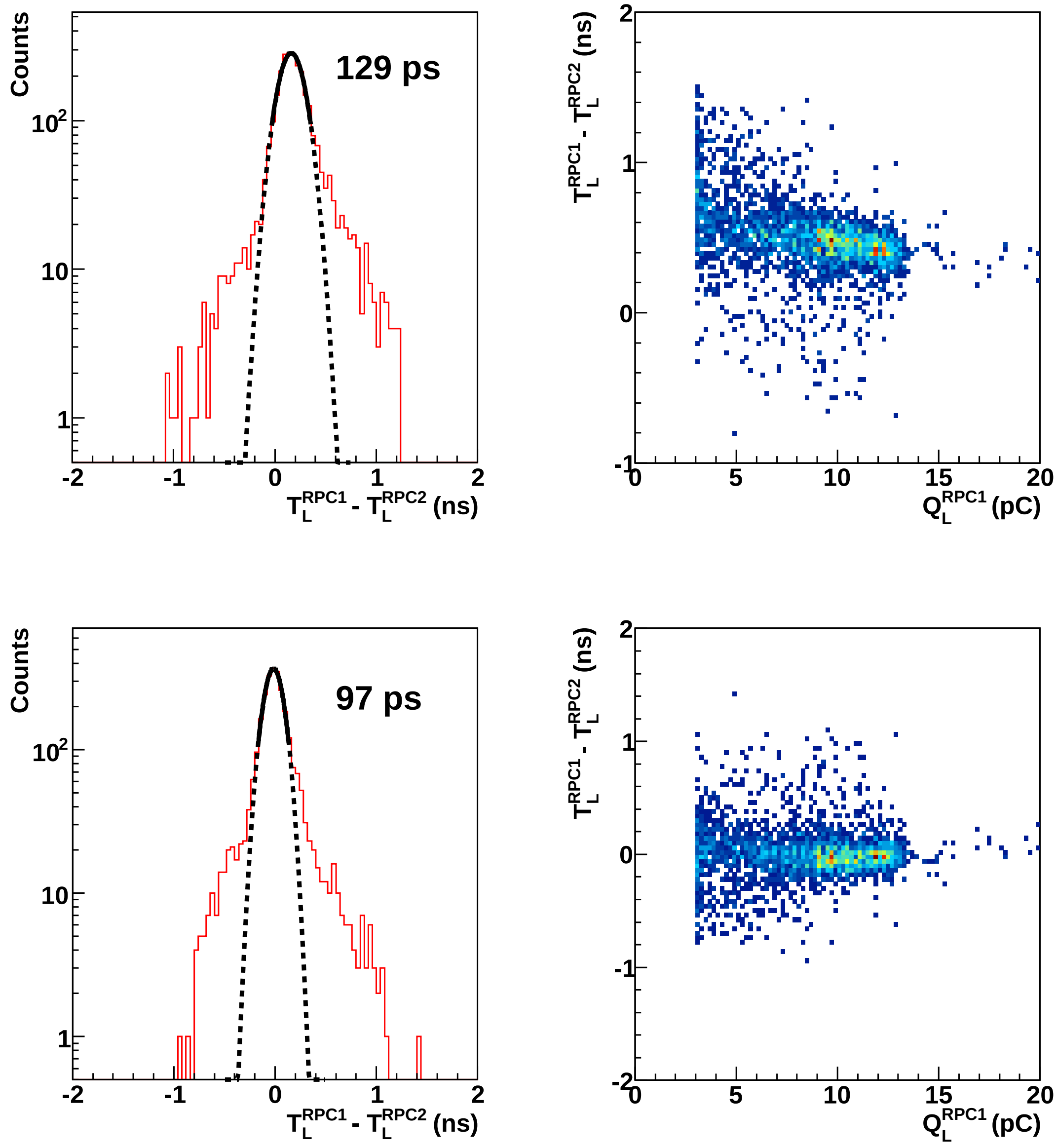

Figure 4.28: Left panels: Time of flight distribution of ^{238}U *ions measured between both modules of the RPC-25 prototype operated at 2800 V and a rate of 10 Hz/cm*^{2} *before (upper panel) and after (lower panel) the slewing correction. Right panels: Time of flight measured in the RPC-25 prototype as a function of* Q_L^{RPC1} *before (upper panel) and after (lower panel) slewing correction.*

determine the time resolution of each individual detector. Fig. 4.29 shows the time resolution of the best performing tRPC (RPC2) as a function of the beam intensity at 2800 (triangles) and 3000 V (open circles). As can be seen, the time resolution of this tRPC presents a strong dependence with respect to the beam intensity reaching a value of 30 ps (1.5-σ) for an intensity of 20%, which is close to TACQUILA's intrinsic resolution. At around 0.5%, the time resolution is degraded to 80 ps (1.5-σ). The large number of electrons per bunch, that increases with the beam intensity, favors the formation of high amplitude pulses due to multiple avalanches created during its short length (few ps), and as a consequence the time resolution is improved. Also, it is worth pointing out that no significant difference was found in the time resolution measured at two different voltages (2800 and 3000 V). The resolution of the reference scintillator is also presented in this plot having values comparable to the ones measured with the RPC-25 for the highest beam intensities. The time resolution of the RPC-25 prototype (2800 V) as a function of the mean charge of the signal is shown in Fig. 4.30 for electron bunches (triangles) and ^{238}U (star). The time resolution of the reference scintillator is also included (squares).

It has to be considered that in the electron bunches and ^{238}U experiments the signals coming from the tRPCs were divided to construct the acquisition trigger. Thus, the amplitude and charge of the signals were reduced to half of their initial value. Moreover as mentioned before, the RPC-30 prototype used to measure ^{136}Xe ions was equipped with a FEE (transistor+OPA657) with a charge gain factor of 4, while the FEE equipped in the RPC-25 prototype (transistor+MAXIM4224) had a charge gain factor of around 22 in the range of interest. It has be taken also into account that the charge of the signal induced in the double-gap tRPC can be the double with respect to the single-gap tRPC because the signal corresponds to the sum of the signals induced in each gap. This leads to a total gain factor between both FEE ranging from 2.5 up to 5. The mean value of the charge of the signals induced in RPC-30 prototype by ^{136}Xe ions at 2800 V is about 5.5 pC. This value can be extrapolated into the transistor+MAXIM4224 FEE, yielding a value that can be in a range from 14 up to 28 pC. As can be seen in Fig. 4.30, for those mean values of the extrapolated mean charge, a time resolution between 35 and 55 ps (1.5-σ) was achieved with the RPC-25 and the transistor+MAXIM4224 FEE measuring electron bunches, in good agreement with the value of 47 ps (1.5-σ) obtained with the RPC-30 measuring ^{136}Xe (solid circle). Therefore, measurements using electron bunches represent an alternative method to investigate the behavior of the tRPC under large charge depositions. However, in the case of ^{238}U a general comparison is not possible since one has to consider the critical influence of the rate effects on the mean charge value of the pulses. This will be studied for the ^{136}Xe experiment in the next section.

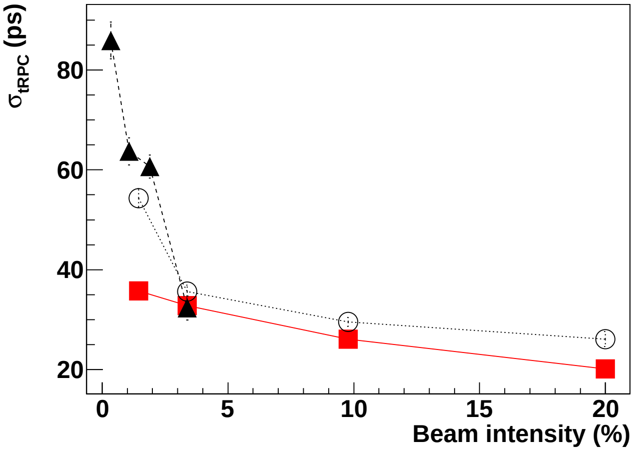

Figure 4.29: Time resolution of one of the tRPC modules of the RPC-25 prototype as a function of the electron beam intensity at 2800 V (triangles) and 3000 V (open circles). Squares refers to the time resolution of the reference scintillator.

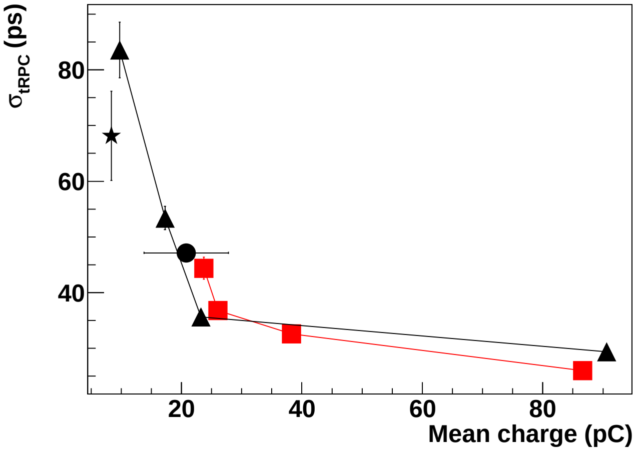

Figure 4.30: Time resolution as a function of the charge of the signal. RPC-25 with electron bunches (triangles), RPC-25 with ^{238}U (star), reference scintillator with electron bunches (squares) and RPC-30 with ^{136}Xe after extrapolation (solid circle). See text for details.

4.4.6.2. Effect of the rate in the time resolution

Irradiation rate is a key parameter that can smear out the timing performances of the tRPCs especially in the detection of heavy ions where the deposited energies are much larger compared to MIPs. A local reduction of the effective gap field is produced with an increase of the rate due to the space charge effect which could be especially important in the case of the heavy ions. We have explained in the previous section that during the ^{136}Xe experiment we were able to determine two different rate intervals of 1-2 and 3-5 Hz/cm^2, respectively. In Fig. 4.31 the mean charge of the signals is represented as a function of the applied voltage for the different rate intervals considered here. We observe an effect of the charge reduction as the rate increases for each value of the voltage. However, the effect seems to be constant along the entire range revealing that the voltage does not play a key role in the charge quenching.

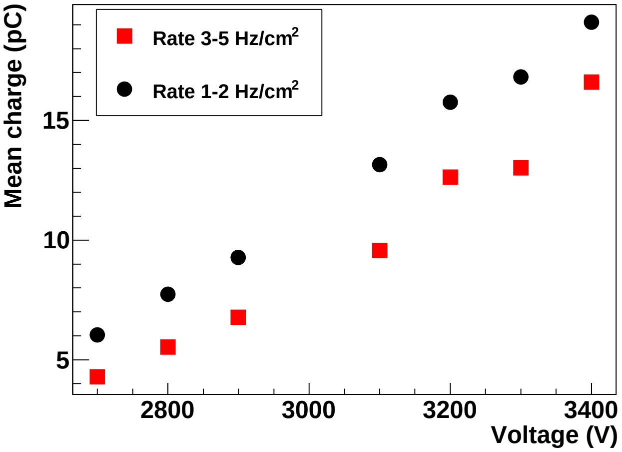

Figure 4.31: Mean value of the signal charge as a function of the applied voltage for ^{136}Xe at 560 A MeV at two different irradiation rates per surface unit.

At higher rates, an electric-field screening is clearly induced due to the large amount of charge carriers moving inside the gap. Since the tRPC does not have enough time to *eliminate* the charge collected at the electrodes, each particle sees an average reduction of the effective gap field, the avalanche process is less intense and as a consequence the mean value of the signal charge distribution and its width are reduced, as can be seen in Fig. 4.32.

For example, at 2900 V the value of the charge for an irradiation rate of 1-2 Hz/cm^2 is around 9 pC. If the rate is increased up to 3-5 Hz/cm^2,

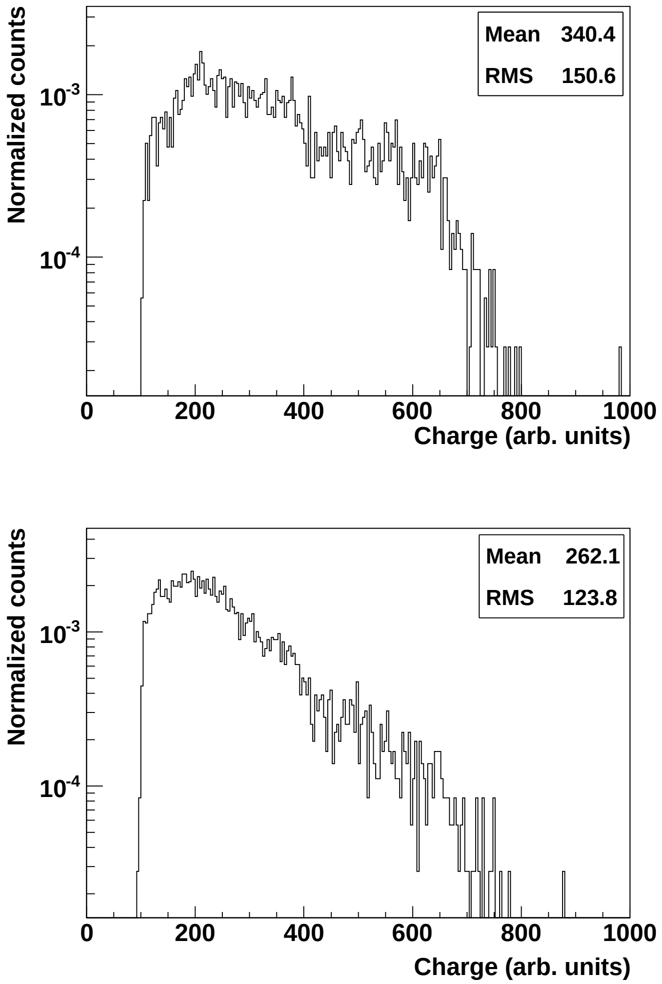

Figure 4.32: Upper panel: Normalized signal charge distribution of the RPC-30 under an irradiation rate of 1-2 Hz/cm^2. Lower panel: Same as the upper panel but for an irradiation rate of of 3-5 Hz/cm^2.

the applied voltage has to be increased up to 3100 V to preserve the same equivalent field. Therefore, as shown in Fig. 4.33 the time resolution is degraded when the irradiation rate is increased from 1-2 up 3-5 Hz/cm^2 due to the reduction of the mean charge of the pulses. This effect is dramatically enhanced for higher values of the high voltage probably due to other mechanisms that play an important role in the formation of the signal under such conditions. The mean and width reduction of the charge distribution due to the charge damping really difficults the separation between avalanche and streamer pulses.

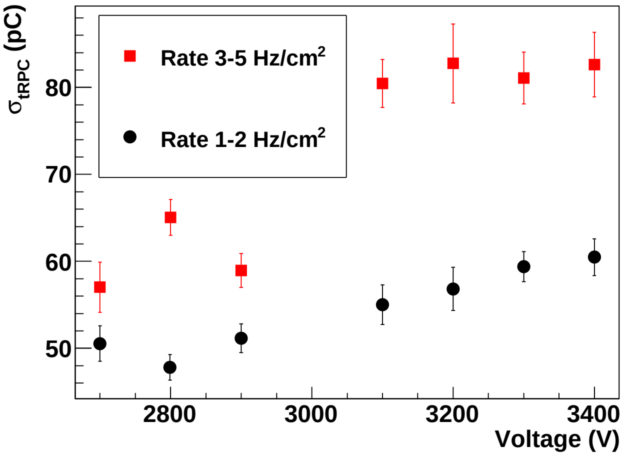

Figure 4.33: Time resolution as a function of the applied voltage for ^{136}Xe at 560 A MeV at two different irradiation rates per surface unit.

4.4.6.3. Effect of the gas mixture

To investigate the effect of the gas mixture, an experiment was performed at HZDR - Rossendorf (Germany) where the RPC-40 prototype was irradiated with a single electron beam of 40 MeV. We used three different gas mixtures completely free of iso-butane, just varying the proportion of SF_6. The chamber was operated at 3200 V. For each gas mixture we obtained a similar time resolution of around 200 ps due to the beam profile, which is far from the results obtained with heavy ions and electron bunches. Therefore, we investigated the role of the gas mixture on the streamer formation. Contrary to the case of the ^{136}Xe, streamer pulses could be separated from the avalanche pulses in the charge distributions, probably due to the relatively low electric-field screening effect induced by the free charge carriers liberated in the ionization of the gas by these 40 MeV electrons, almost in the range of MIPs. The results are presented in the table 4.2 and the charge distributions digitized by TACQUILA are shown in the Fig. 4.34. As expected, the reduction of the proportion of SF_6 in the gas mixture leads to a substantial increase of the streamer pulses (up to 24%) since the avalanche formation is less quenched. However, an adequate reduced proportion of SF_6 may favor the pulse charge amplification minimizing the walk-time effect and leading to an improvement of the time resolution while keeping the streamer production as low as possible.

Gas mixture	Streamer ratio (%)
90% $C_2H_2F_4$ - 10% SF_6	1%
95% $C_2H_2F_4$ - 5% SF_6	8%
99% $C_2H_2F_4$ - 1% SF_6	24%

Table 4.2: Ratio of streamers for different gas mixtures.

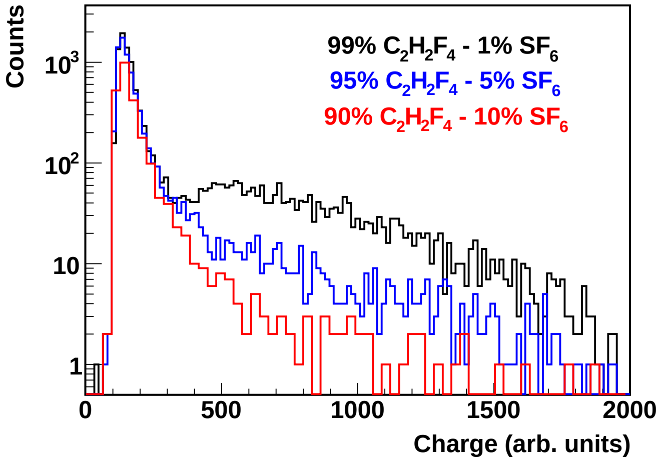

Figure 4.34: Charge distributions obtained for different gas mixtures.

4.4.6.4. Efficiency and streamer production

The efficiency of the RPC-11 (double-gap) and RPC-22 (single-gap) prototypes was measured for different ions with a wide range of nuclear charges. To do this, we performed two experiments at GSI where the prototypes were irradiated with a ^{12}C and a ^{64}Ni beams at 700 and 500 A MeV of energy, respectively, and a repetition rate of few tens of Hz/cm^2. Similarly to the ^{136}Xe experiment,

The efficiency was determined with the ratio of ions detected by the RPCs and the scintillators, respectively. The amplitude threshold from which we determined whether a particle induced a signal in the detectors was set considering the noise level of the PMTs and FEE of the RPCs.

In the experiment with ^{12}C, the efficiency of the RPC-11 was investigated. The thickness of the scintillators made it possible to identify projectiles traversing the RPC with different atomic numbers. The energy loss of the ions in the scintillators, which is proportional to the squared atomic number, was determined by integrating the signals coming from the PMTs. In the scatter plot of the Fig. 4.35 the energy loss of the ^{12}C ions in both plastic scintillators is shown. Ions created in nuclear reactions of the ^{12}C beam with layers of matter placed upstream of our setup are located in the diagonal of this plot. These ions had the same energy loss in both scintillators, thus, their atomic number did not change when traversing the RPC. A calibration was done considering that each spot of this line corresponds to an atomic number from Z=1 up to Z=6. On the other hand, ions located in the vertical line of the same plot reacted in any layer of matter of the setup losing protons. The projection onto the y axis displayed in the Fig. 4.36 corresponds to the energy loss in the scintillator placed downstream of the RPC. The peak with Z=1 is cut due to the thresholds applied to the signals coming from the PMTs to construct the acquisition trigger which ensure a negligible noise level. In the ^{65}Ni beam test we used the primary beam only for investigate the efficiency of the RPC-11 and the RPC-22.

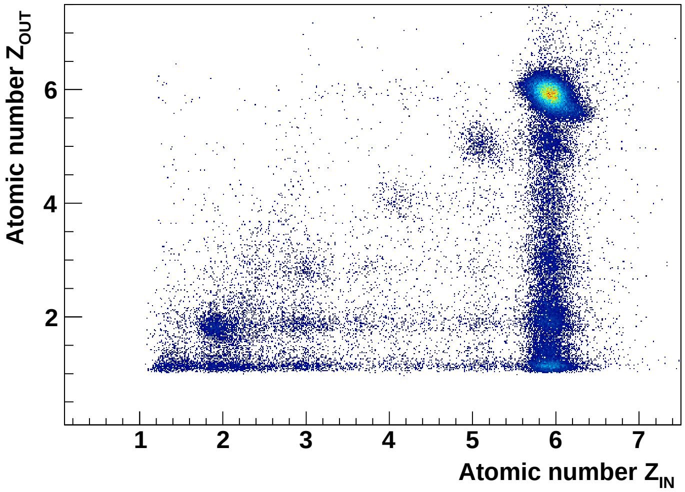

Figure 4.35: Two-dimensional plot of the energy loss of ^{12}C ions in both plastic scintillators. Z_{IN} and Z_{OUT} refers to the scintillators placed upstream and downstream of the target, respectively.

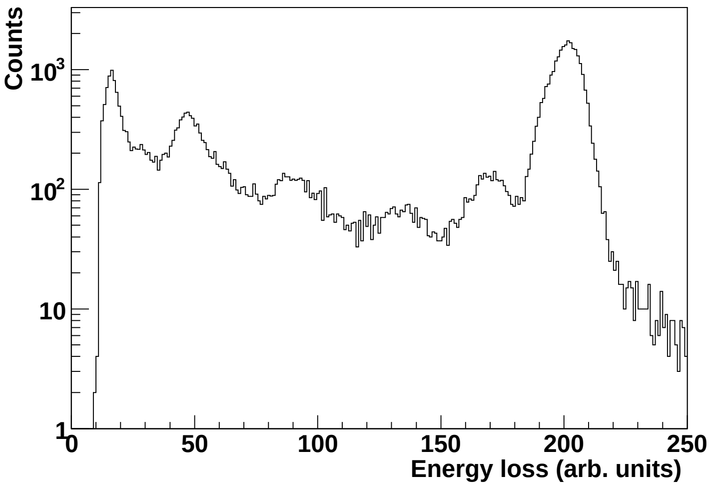

Figure 4.36: Energy loss of ^{12}C *ions in the scintillator placed downstream of the RPC.*

The efficiency for ions with different atomic numbers as a function of the high voltage is plot in the Fig. 4.37. For Z=2 (open circles) detection efficiencies near 100% are rapidly achieved for voltages higher than 2500 V. In what concerns ions with Z=6 (open squares) we obtained an efficiency of 100% in all the high voltage range studied here. The value of the detection efficiency for protons (open triangles) at 2500 V drops to 55% and is increased up to 90% for high voltage values higher than 3000 V. This is consistent with results for efficiency obtained with MIPs (90%-94% [Fon02]). Efficiency values for Z=2,3 and 4, also about 100%, are not included for the sake of simplicity. In this plot we also present the efficiency for Z=28 measured with the RPC-11 (stars) and RPC-22 (solid circles) prototypes. One can see that an efficiency close to 100% was reached with both single- and double-gap prototypes. To extend these results to higher atomic numbers we performed an experiment using a similar experimental scheme and working parameters where the efficiency of the RPC-11 prototype was determined under the irradiation of medium-mass nuclei produced in the ^{238}U fragmentation at 750 A MeV. An atomic range from Z=1 up to Z=38 was covered in this experiment but with poor energy loss resolution due to the limited dynamic range of the plastic scintillators. Moreover, the efficiency was also determined for the long-size one-gap prototype under ^{136}Xe irradiation (5 Hz/cm^2, by using the information of the spectra digitized with TACQUILA. Here, the efficiency was defined as the ratio between the number of events detected by one of the modules of this prototype and the number of registered triggers.

It has to be considered that the scintillators of the trigger were not perfectly aligned with the strip, thus, a possible geometrical factor could reduce the nominal value of the efficiency. Another issue is that of the threshold of each TACQUILA channel which value depends on the noise/signal ratio and is normally lower than the trigger threshold. Signals with an amplitude lower than this threshold are rejected,and therefore, the efficiency drops.

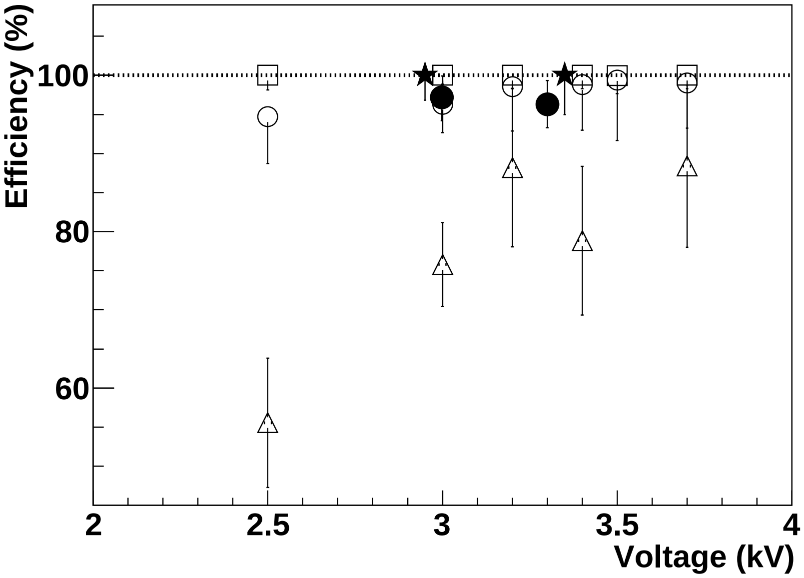

Figure 4.37: Detection efficiency of the RPC-11 as a function of the applied voltage for different atomic numbers: Z=1 (open triangles), Z=2 (open circles), Z=6 (open squares), Z=28 (stars) and Z=28 for the RPC-22 (solid circles).

The results of all these experiments are compiled in the Fig. 4.38 where we plot the efficiency as a function of the atomic number. We can conclude that the ionization produced by ions with atomic charges higher than Z=1 is sufficient to start the avalanche process even at values of electric field well below the typical ones of tRPCs devoted to MIPs measurements. The large plateaus that represent the efficiency respect to the nuclear charge and the voltage, are mandatory to define a working point with adequate parameters and gains. Moreover, we have tested that the dynamical range of the FEE accommodates the entire distribution of avalanche signals. No limitations due to the rate were observed, even at the higher values of the atomic number studied in this work. Furthermore, single-gap tRPCs (RPC-22 and long-size prototype) present detection efficiencies compatible with 100% which opens the possibility of a drastic reduction of matter in the design of the detector in order to reduce the straggling when detecting relativistic heavy ions.

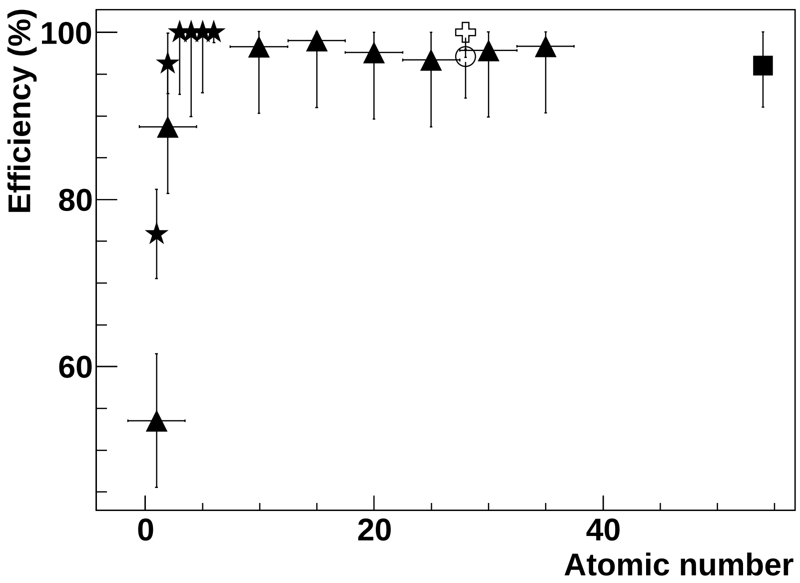

Figure 4.38: Efficiency as a function of the atomic number measured in different experiments: ^{238}*U fragments (triangles),* ^{12}*C (stars),* ^{65}*Ni for RPC-11 (cross) and RPC-22 (open circle), and* ^{136}*Xe (square).*

In the last part of this section the streamer production is analyzed for the experiments where the RPC-11 was irradiated with ions produced in the fragmentation of ^{12}C and ^{64}Ni ions. Owing to the large energy deposition of the ions in the active gas volume of the tRPC a relatively large fraction of streamers is expected which may induce negative effects such as dead-time increase and time resolution worsening. The FEE installed in this RPC (GALI-S66+MAXIM4223) allowed us to separate streamer from avalanche pulses due to the total gain of the amplifier stage. The ratio between the streamer signals respect to total as a function of the high voltage for different ions is shown in Fig. 4.39. As can be seen, the streamer ratio strongly depends on the gap voltage and the atomic number of the ions, being below 1% and 10% for Z=6 at 3000 V and 3200 V, respectively. Beyond the latter value of the voltage, the streamer ratio increases rapidly for all the atomic numbers. In the case of Z=28, the streamer contribution amounts up to 28%, but the trends indicates that for lower values of the field the ratio drops to a value between 5 and 10%. However, in the case of the single-gap RPC (RPC-

22) the streamer ratio is even lower at 3000 V (2%) due to the amount of streamers increases with the number of gaps.

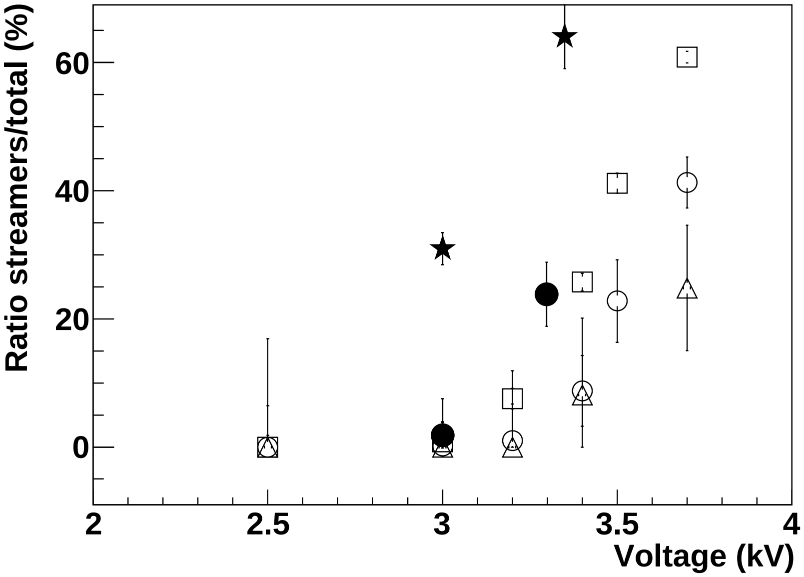

Figure 4.39: Ratio of streamer signals to total for different ions: Z=28 (stars), Z=6 (squares), Z=5 (circles),and Z=2 (triangles).

4.5. Conceptual design of the iToF tRPC modules

Considering the working parameters previously discussed, the tRPCs for the iToF will be constituted by single-gap gas-tight modules made of two soda-lime glass plates of 1 mm thickness glued together and segmented in 16 strips of 1000 mm × 20 mm width and 2 mm of separation, covering a surface of 1 m and 2 m in the vertical and horizontal coordinates, respectively. The spatial resolution expected, according to the time-resolution, is of some mm: enough for the purpose of the correction of the flight-path of the order of 15 meters. With this configuration, the resolution can be improved by measuring in the consecutive detecting planes of the iToF while minimizing the amount of matter, thus, the energy straggling. If four detection planes are considered, the total thickness of the detector amounts to 8 mm of soda-lime glass which fits with the typical range of the heaviest ions of interest

(15 mm for ^{238}U at 400 A MeV). This improve the time resolution a factor two. Multi-hit capabilities will be also fulfilled by crossing the strips of consecutive planes 90°. This configuration will ensure its proper performance under low rate conditions minimizing the streamer production and improving the efficiency up to around 100%.

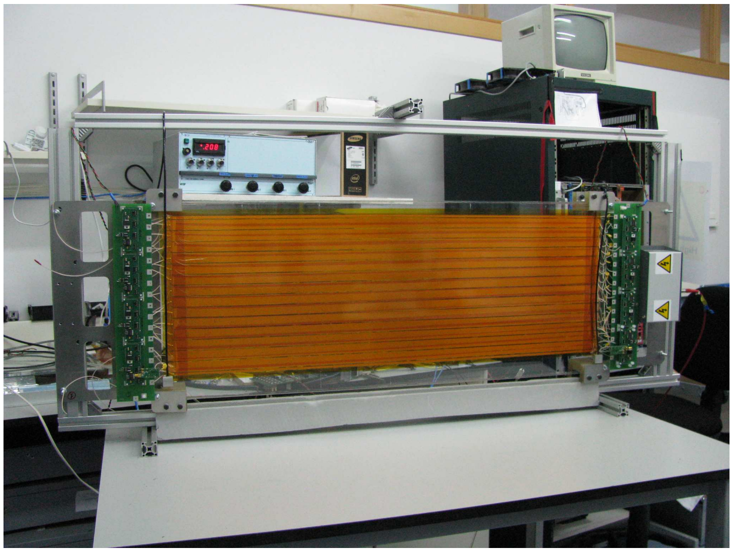

Figure 4.40: Multi-strip single-gap tRPC module for the iToF.

4.6. Conclusions

In this chapter we have investigated the performance of the tRPCs under relativistic heavy ion irradiation. Several tRPCs prototypes have been tested with ions with a wide range of atomic number such as ^{12}C, ^{64}Ni, ^{238}U and ^{136}Xe obtaining efficiency values of around 100% keeping the streamer production low enough. This defines a regime where the tRPCs can be safely operated It is worth pointing out that these efficiency values were achieved with both double- and sigle-gap tRPCs prototypes which opens the possibility of a reduction of the amount of layers of the detector. Time resolutions of around 70 ps were obtained with the RPC-25 prototype when measuring ^{238}U ions at a relatively high repetition rate of 10 Hz/cm^2, and, values of around 47 ps were achieved with the RPC-30 prototype under ^{136}Xe at 560 A MeV irradiation with a repetition rate of around 2 Hz/cm^2. According to the results we have obtained, we can conclude that the irradiation rate is a critical parameter that must be taken into account when working with heavy ions.

Resistive materials capable to deal with higher irradiation rates is an option that can be considered for future prototypes. We also have demonstrated that a gas mixture with proper proportions of SF_6 is a critical parameter to be determined in order to control the streamer formation under such large energy deposition.

On the other hand, the dedicated FEE developed for the prototype was designed and adapted to the signals produced by ions, and moreover, the data acquisition for timing measurements used in this work (TACQUILA) fulfills our needs. However, it has to be noted that the resolution of the FEE+TACQUILA system (34 ps) could be limiting the time resolution of the measurements. Despite this point, the performance of the electronic system is quite robust and works according to the requirement stated before. In conclusion, these tRPCs provide excellent time resolutions and high efficiencies dealing with relativistic heavy ions at low irradiation rate, and, their features can fulfill the requirements needed for the construction of a tRPC-based ion ToF wall.

Conclusions

In this work we have presented the results of two experiments performed to investigate the fission process at high excitation energies. We have studied the proton-induced fission of ^{181}Ta at 1000, 800, 500 and 300 A MeV, and, the proton- and deuteron-induced fission of ^{208}Pb at 500 MeV. Both experiments were performed at GSI using a dedicated setup for fission studies in inverse kinematics which allowed to unambiguously detect both fission fragments simultaneously and determine several observables.

In the ^{181}Ta experiment, two ionization chambers surrounding the target were used to select reactions produced in the liquid hydrogen cell which enhanced the selection of the fission events that were determined by measuring both fission fragments in coincidence using a double plastic scintillator covering the angular acceptance of the fragments emitted in forward direction. Total fission cross sections were determined with high accuracy and the results were compared to data measured in previous experiments. These new data complete the scarce measurements existing above 700 MeV and allowed to address the existing discrepancies. At energies below 500 MeV, where the expected low value of the cross section complicates the selection of the fission channel among other reactions mechanisms, we have demonstrated that a proper data reduction and a careful determination of the uncertainties provide precise values that enabled to clarify previous results. Our data are consistent with the highest values of the fission cross sections determined in previous experiments in that energy range. Moreover, these results are in good agreement in the entire energy range studied in this work when compared to the systematic predictions established by Prokofiev. Thus, in this experiment has been proved that the inverse kinematics technique enhances the detection of both fission fragments in reactions involving low fissility nuclei such as ^{181}Ta.

In addition, the results obtained from this experiment were compared with model calculations performed with an intra-nuclear cascade code (INCL and ISABEL) coupled to a code describing the evaporation process of a highly excited nucleus. For the latter stage we used ABLA statistical code including a time-dependent fission width governed by a friction parameter β, and, GEMINI++ code based on pure statistical description of fission. It has to be taken into account that the level-density parameter in ABLA was determined following Ignatyuk's prescription, while the level-density ratio a_f/a_n is fixed to 1.036 in GEMINI++. A complete benchmark of the codes revealed that the predictions obtained with INCL+ABLA and ISABEL+ABLA considering a value of $\beta = 4.0 \times 10^{21}\ s^{-1}$ have a rather good agreement with the experimental data, while INCL+GEMINI++ calculations underestimate the values in the entire range. Thus, we stated that higher excitation energies have to be induced into the system to undergo fission when using GEMINI++. We also prove that dissipative effects included in ABLA are too strong at low excitation energies (300 MeV of beam energy) where the fission decay rate depends on the density of states above the fission barrier according to Bohr-Wheleer's statistical model. This fact is stressed comparing the calculations with the experimental data and the Prokofiev systematics. We also demonstrated that despite calculations made with INCL and ISABEL provide similar values of the total fission cross section, fissioning systems determined with ISABEL provide lower angular momentum distributions reducing the fission probability. In conclusion, the total fission cross section does not represent a robust observable in order to characterize the predictive power of such codes, although several conclusions about the effect of the dissipation strength may be inferred.

An improved version of the previous detection setup including a double ionization chamber (Twin MUSIC) and a time-of-flight wall was utilized to investigate proton- and deuteron-induced fission of ^{208}Pb. In this case, we measured both fission fragments in coincidence using the Twin MUSIC which allowed us to determine their atomic number with high resolution. Using this information, the atomic number of the fissioning system was reconstructed (Z_1+Z_2) for both reactions. This enabled the determination of two observables with valuable information regarding dissipative effects on the fission process. While partial fission cross sections as a function of Z_1+Z_2 showed that higher excitation energies are induced in the reaction with the deuteron creating fissile systems with larger charge loss, while the width of the fission fragments charge distribution (σ_z) as a function of Z_1+Z_2 revealed that this signature only depends on the temperature the system has at the saddle point T_{sad}. These conclusions also support the fact that each one of these signatures are sensitive to one of the stage of the process. The partial fission cross sections are determined during the cascade stage while σ_z is sensitive to the evaporation phase.

To extract conclusions about the strength of the dissipation factor and the transient delay during the pre-saddle stage requires a comparison of the experimental results with model calculations. We validated the cascade stage performing calculations with INCL+ABLA and ISABEL+ABLA which proved that the shape of the distribution of the partial fission cross sections as a function of Z_1+Z_2 depends on the excitation energy initially induced to the system while their magnitude is given by the β value considered for the evaporation stage. For the reaction ^{208}Pb+d calculated with INCL+ABLA and $\beta = 4.0 \times 10^{21}\ s^{-1}$ partial fission cross sections have a good agreement with the experimental data in almost the entire Z_1+Z_2 range while calculations made according to a purely statistical model lead to an overestimation. Predictions of INCL+ABLA and ISABEL+ABLA concerning ^{208}Pb+p at 500 MeV show several discrepancies with respect to the experimental data, especially for those fissioning systems with higher excitation energy. The magnitude of the transient effects was estimated using the information inferred from the comparison of σ_z measured for both reactions with calculations made with INCL+ABLA proving that the data fits with predictions considering $\beta = 4.0 \times 10^{21}\ s^{-1}$. This fact was explained as a reduction of T_{sad} due to the delay induced in the system during the early stage of the fission process. According to the results obtained in this experiment, we conclude that spallation reactions investigated using the inverse kinematics technique are a powerful and reliable reaction mechanism to investigate dynamical effects of the fission process due to the characteristics of the fissioning systems and the measured observables.

The experimental setups described in this work will be substantially improved in next-generation fission experiments using the inverse kinematics technique (SOFIA, R^3B and FELISe) which will provide a most complete reconstruction of the fission reaction measuring other important observables constrained in the present experiments due to the limited available technology. One of the main challenges will be the measurement of the masses of the fission fragments. A state-of-the-art ToF wall with a demanding time resolution will be needed for this purpose. We have undertaken a dedicated R&D program to prove the feasibility of tRPCs (timing Resistive Plate Chambers) for the construction of such time-of-flight wall for fission residues and heavy ions in the framework of the R^3B experiment (iToF) for the future FAIR facility. In this work, we have demonstrated that tRPCs can be safely operated under the irradiation of relativistic heavy ions while keeping their outstanding timing properties. We have built and test several small-size double-gap single-strip tRPC prototypes with ions with a wide range of atomic number such as ^{12}C, ^{64}Ni and ^{238}U giving values of efficiency of 100% and time resolutions of around 70 ps while keeping the streamer production low enough. Moreover, outstanding time resolutions of about 40 ps have been obtained when measuring electron bunches. Nevertheless, according to the iToF requirements, the best results have been obtained so far with a single-gap self-contained multi-strip tRPC prototype made with two glass plates of 40 cm×20 cm of area and 1 mm thickness achieving efficiency values of around 100% and time resolutions of 47 ps under the irradiation of a ^{136}Xe beam at 560 A MeV and a repetition rate of 1-2 Hz/cm^2. The minimization of the amount of matter contained in this prototype will enable the possibility of a ToF wall with several detection planes which in principle would improve the time resolution of the measurements. However, one has to keep in mind that the effect of the rate is critical in such detectors, and thus, this opens the possibility of the construction of prototypes based on resistive materials capable to deal with higher irradiation rates.

We have demonstrated that the performance of the tRPC under relativistic heavy ion irradiation fulfills the requirements needed for the construction of the iToF detector, achieving time resolutions below 50 ps under low rate conditions. According to these results, a module of the iToF detector will consist in a single-gap multi-strip tRPC made with two soda-lime glass plates of 1000 mm× 425 mm glued together, defining a single 300 μm gap. The active detection zone will consist in 16 copper strips of 1000 mm × 20 mm, separated by 2 mm. A gas mixture consisting of 90% of $C_2H_2F_4$ and 10% of SF_6 will be used to control the streamer formation and will allow the correct performance of the tRPCs operated at 2800 V, at maximum.

Resumen en castellano

La fisión es un mecanismo extremadamente complejo que requiere un tratamiento dinámico para describir la evolución del proceso en términos de grados de libertad intrínsecos y colectivos. Las teorías de transporte [Wei80] basadas en cálculos realizados mediante ecuaciones de Langevin demuestran ser una herramienta potente y adecuada para describir la evolución colectiva del núcleo y constituye la base de los modelos actuales. Sin embargo, más de 70 años de intensa investigación revelan que el proceso de fisión esta lejos de ser completamente entendido y nuestro conocimiento teórico es insatisfactorio. Las medidas experimental de observables fuertemente ligados al proceso, tales como probabilidades de fisión, masas y cargas nucleares, energía cinética de los fragmentos y multiplicidades de partículas ligera y rayos γ, están limitadas por la tecnología disponible y resultados obtenidos con diferentes técnicas y dispositivos experimentales presentan inconsistencias. Se requiere una mejora substancial para resolver la discrepancias existentes, validar modelos modernos y extender los limites actuales de nuestro conocimiento sobre el proceso de fisión.

La fisión nuclear juega un papel fundamental en la descripción de varias propiedades nuclear y proveé información valiosa en temas generales de física y astrofísica. En efecto, temas como efectos de capa en núcleos super e hiperdeformados, el proceso r en la nucleosíntesis, la viscosidad de la materia nuclear y la transferencia de energía entre los fragmentos emergentes necesitan de una descripción correcta del proceso de fisión. También és extremadamente importante en la produccióndе haces de iones radioactivos (RIB) dedicados a estudiar las propiedades de núcleos exótic ricos en neutrones lejos de la estabilidad [PL11] y en el desarrollo de fuentes de espalación para el desarrollo de Sistemas Asistidos por Acelerador (ADS).

La primera descripción del proceso de fisión basado en el modelo de gota líquida fué establecida por Bohr-Wheeler [Boh39]. En este modelo estadístico, la probabilidad de desexcitación de un núcleo pesado esta gobernada por el espacio de fases disponible en el punto de silla (saddle point). Kramers [Kra40] propuso una descripción de la fisión como un proceso de difusión usando la ecuación de Fokker-Planck (FPE) que describe la evolución del sistema de acuerdo a los grados de libertad intrínsecos y colectivos. La solución a esta ecuación conduce a una reducción de la anchura de fisión predicha por el modelo estadśitico debida a la transferencia de energía entre los grados de libertad que se incluye como parámetro en la FPE (β). Pocos años depués el concepto de tiempo de tránsito fué introducido por Grangé *et al.* [Gra83] después de resolver numéricamente la FPE asumiendo unas condiciones iniciales que coinciden con las estudiadas en este trabajo. Esta solución lleva a una descripción de la anchura de fisión dependiente del tiempo que constituye una gran diferencia con respecto al modelo de Bohr-Wheeler. La fisión está altamente inhibida al principio del proceso que necesita un cierto tiempo de tránsito para alcanzar el valor estacionario (por encima de la barrera de fisión) de la anchura de fisión predicha por Kramers. Estas ideas establecen la bases de nuestro conocimiento actual de la dinámica del proceso de fisión.

En este trabajo hemos investigado la fisión del ^{181}Ta inducida por protones y la fisión del ^{208}Pb inducida por protones y deuterones a energías relativistas. Los experimentos se realizaron en el laboratorio GSI (Darmstadt) empleando un dispositivo experimental diseñado para estudios de fisión en cinemática inversa. Este dispositivo facilita el contaje de proyectiles y la identificación de los productos de la reacción. Los resultados obtenidos en estos experimentos se emplearon para extraer resultados cuantitativos acerca de effectos de disipación y tiempos dinámicos durante en la etapa durante la cual el sistema alcanza el punto de silla. El uso de modelos de reacción punteros que modelan el proceso de fisión es necesario para este propósito.

Los resultados obtenidos han demostrado que este dispositivo experimental, junto a la técnica utilizada, constituyen una herramienta potente para realizar experimentos dedicados a medir las propiedades del proceso de fisión. Sin embargo, la identificación isotópica de ambos fragmentos de fisión simultaneamente y con gran precisión, representa hoy en día un problema complejo presente en los más modernos sistemas de detección. El programa científico del futuro experimento R^{3}B en la instalación FAIR (Alemania) incluirá el estudio completo de reacciones de fisión espalación y multifragmentación en cinemática inversa usando un esquema de detección similar al de este trabajo, incluyendo además in dipolo magnético. La identificaciń isotópica de los productos de reacción requerirá detectores modernos y avanzados con alta eficiencia y aceptancia, y una resolución temporal por debajo de 30 ps. Para cumplir estos requisitos, se propone la construcción de un muro de tiempo de vuelo (ToF wall) basado en cámaras de placas resistivas (RPCs). Este tipo de detectores son ampliamente usados en experimentos de física de altas energías, pero su respuesta y funcionamiento en la detección de iones pesados a energías relativistas son escasamente conocidos. En este trabajo hemos estudiado la eficiencia de detección y la resolución de prototipos de RPC irradiados con diferentes haces de iones pesados y con electrones. Los resultados obtenidos indican la validez de estos detectores para la deteción de iones pesados y la construcción de un muro de tiempo de vuelo.

Fisión inducida por protones en ^{181}Ta

En este experimento realizado en el GSI, el haz de iones de ^{181}Ta se aceleró a 300, 500, 800 and 1000 A MeV de energía con una intensidad del orden de 10^4 iones/s, incidiendo posteriormente en un blanco de hidrógenos líquido. Debido a la cinemática de la reacción, ambos fragmentos de fisión son emitidos hacia delante, permitiendo su detección con alta eficiencia. La figura 1 muestra el esquema del dispositivo experimental.

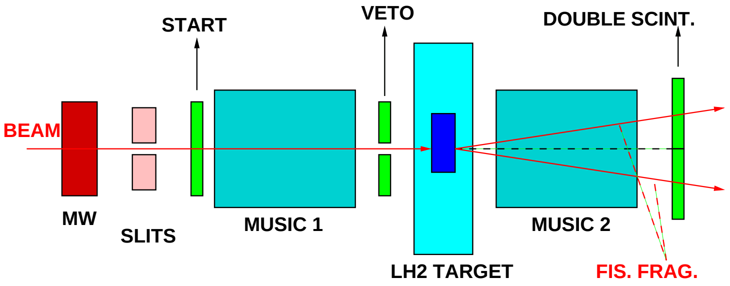

Figura 1: Esquema del montaje experimental usado en este experimento.

Dos cámaras de ionización (MUSIC80) [Pfü94] colocadas a la salida y entrada del blanco de hidrógeno respectivamente, midieron la pérdida de energía de las partículas de tántalo y la de los productos de la reacción. Mediante un gráfico bidimensional que representa la pérdida de energía en ambas cámaras de ionización identificamos reacciones de ^{181}Ta producidas en el blanco de hidrógeno y en capas de materia presentes en la línea de haz. De esta manera, seleccionamos los eventos de fisión producidos únicamente en el blanco. Usando un sistema de dos plásticos centelleadores, ambos fragmentos se detectan en coincidencia, permitiéndonos separar los fragmentos de fisión de otros productos de reacción con un número atómico similar que constituyen un importante fondo de contaminación debido a la baja probabilidad de fisión del ^{181}Ta. El numero de eventos de fisión se extrae de esta identificación, una vez corregido y eliminado el fondo de fragmentación y evaporación.

Las secciones eficaces de fisión se determinan con el cociente entre el número de eventos de fisión y número de proyectiles, ambos normalizados al espesor del blanco. Varios factores de corrección debidos a la eficiencia geométrica del dispositvo experimental, la atenuación de los proyectiles en el blanco y reacciones secundarias de los fragmentos de fisión. Además las incertidumbres estadísticas y sistemáticas se determinaron cuidasosamente para obtener medidas de gran precisión.

Las secciones eficaces obtenidas en este trabajo se presentan en la figura 2, comparados a otros resultados obtenidos en experimentos previos y con la sistemática establecida por Prokofiev. Nuestras medidas confirman los medidas realizadas por Yurevich *et al.* y las secciones eficaces predichas por la sistemática por encima de 700 MeV, resolviendo las discrepancias. A energás más bajas, los datos de este trabajo permiten clarificar los resultados previos, favoreciendo aquellos que presentan las secciones eficaces más altas. Además, en este rango tambieén se confirman las predicciones de la sistemática.

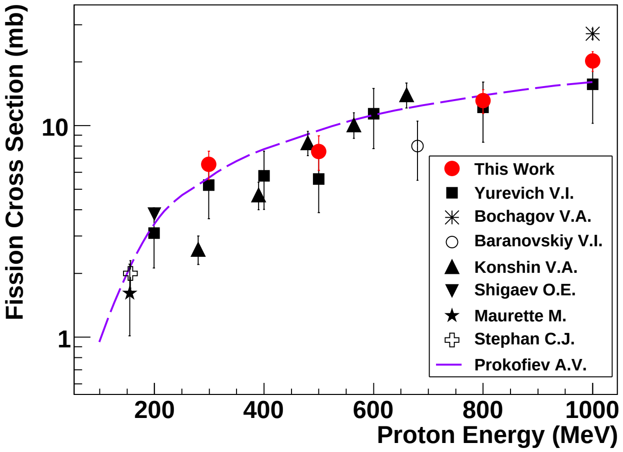

Figura 2: Secciones eficaces de fisión medidas en este trabajo (círculos) comparadas con datos medidos en experimentos anteriores y predicciones de la sistemática de Prokofiev (línea a trazos).

Los datos obtenidos también se comparan con cálculos realizados con códigos que describen el proceso de fisión a alta energía de excitation. En este trabajo hemos usado dos cascadas intranucleares (INCL e ISABEL) que describen el proceso de interacción entre el proton y el ^{181}Ta, y que son acoplados a un código de evaporación. Para esta segunda etapa, en este trabajo hemos usado el código estadístico ABLA que incluye una anchura de fisión dependiente del tiempo y un tratamiento de la disipación nuclear, y el código GEMINI++ que se basa puramente en una descripción estadística del proceso de fisión. La comparación con los datos experimentales nos permite validar su poder predictivo. Como puede verse en la figura 3, los resultados obtenidos usando INCL+ABLA e ISABEL+ABLA considerando un coeficiente de disipación $\beta = 2{,}0 \times 10^{21}\ s^{-1}$ están en buen acuerdo con los datos experimentales, mientras que los cálculos hechos con INCL+GEMINI++ subestiman los valores de sección eficaz. Esto es debido a que durante la evaporación calculada mediante GEMINI++, el sistema necesita más energía de exciatación inicial para poder fisionar.

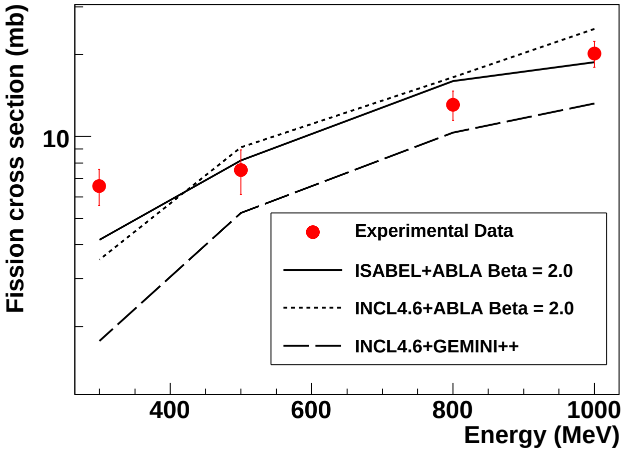

Figura 3: Secciones eficaces de fisión medidas en este trabajo (círculos) comparadas a cálculos realizados usando INCL4.6+ABLA y ISABEL+ABLA ($\beta = 2{,}0 \times 10^{21}\ s^{-1}$), y INCL+GEMINI++.

Fisión inducida por protones y deuterones en ^{208}Pb a 500 A MeV

En este experimento se siguió un procedimiento experimental similar al anterior, pero el sistema de detección se mejoró substancial mente incluyendo una camara de ionización doble (Twin MUSIC) y un muro de tiempo de vuelo, como puede verse en el esquema de la figura 4.

Usando cinemática inversa, los iones de ^{208}Pb son acelerados a 500 A MeV hasta el sistema de detección donde incide en el blanco de de hidrógeno o deuterio líquido produciéndose la reacción. Similarmente al experimento anterior, dos cámaras de ionización puestas delante y detrás del blanco en la línea de haz se utilizaron para identificar reacciones en el blanco de hidróngeno y no en otras capas de material presentes en la línea de haz. Los

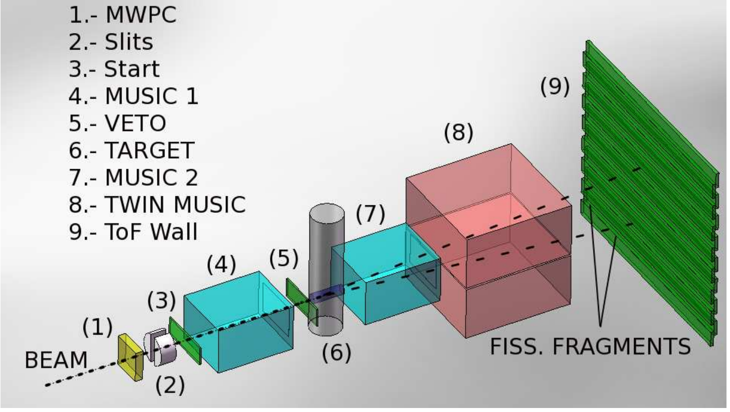

Figura 4: Sistema de detección usado en este experimento.

fragmentos de fisión se detectan simultaneamente en ambas partes de la doble cámara de ionización, y a su vez, son identificados en número atómico (Z) con una resolución del orden de $\Delta Z = 0{,}55$. La eficiencia de detección de la Twin MUSIC se determinó mediante la posición de los fragmentos de fisión en el muro de tiempo de vuelo. Con esta información somos capaces de reconstruir el número atómico del sistema fisionante Z_1+Z_2.

Varios observables pueden extraerse a partir de estas medidas. La sección eficaz total de fisión para ambas reacciones se determinó con gran precisión. Para extraer conclusiones acerca del proceso, estudiamos la sección eficaz de fisión parcial y la anchura de la distribución de carga de los fragmentos de fisión (σ_z), ambas en función de Z_1+Z_2. Estos observables son sensibles a los efectos de disipación y tiempo de tránsito y nos permiten estudiar las características derivadas de inducir la fisión con protones o con deuterones.

La sección eficaces parciales muestra una diferencia clara entre la energía de excitación inducida en ambos sistemas (ver figura 5), siendo mayor en el caso del deuterón, lo que nos permite crear sistema fisionantes con un menor número atómico. Así pues, la forma del espectro de secciones eficaces parciales está estrechamente relacionada con la distribución de energía de excitación, la cual a su vez, sólo depende de cómo el sistema fisionante se define durante la etapa de colisión.

Respecto a σ_z en función de Z_1+Z_2, podemos observar en la figura 6, que para ambos sistemas se obtienen resultados similares, lo que indica que este proceso es independiente del canal de entrada usado para crear el sistema fisionante, y está estrechamente relacionado con la temperatura que alcanza el sistema en el punto de silla (T_{sad}) [Ben02]. Además, este observable se determina durante la etapa de evaporación, lo que significa que cada uno de los observables definidos es sensible a una de las etapas del proceso de fisión.

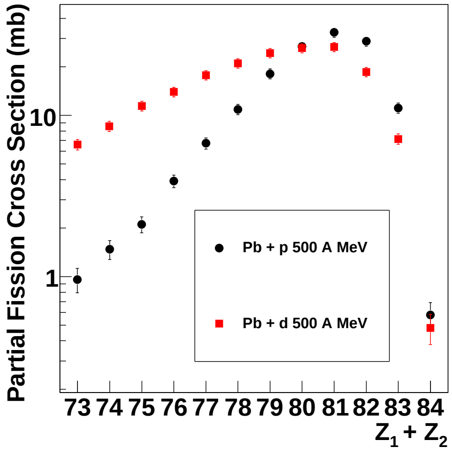

Figura 5: Secciones eficaces parciales de fisión en función de Z_1*+*Z_2 *para las reacciones* ^{208}*Pb+p (círculos) y* ^{208}*Pb+d (cuadrados) a 500 A MeV.*

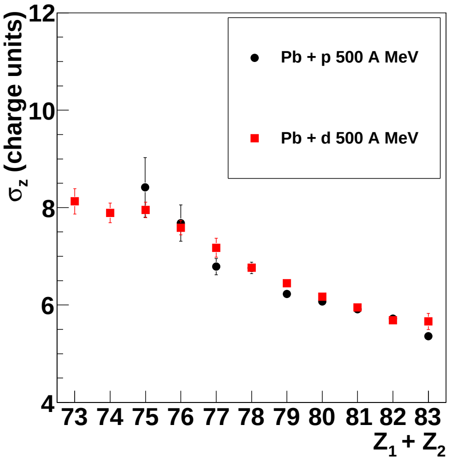

Figura 6: σ_z *en función de* Z_1*+*Z_2*.*

Estos resultados se comparan con cálculos realizados con códigos que describen la fisión, lo que nos permite determinar cual es el efecto de la disipación nuclear en el proceso de fisión. Para cálculos realizados con INCL+ABLA e ISABEL+ABLA para la reacción ^{208}Pb+p a 500 A MeV obtenemos una sección eficaz total de fisión similar, 96 y 114 respectivamente ($\beta = 4{,}0 \times 10^{21}\ s^{-1}$). Sin embargo, como podemos ver en el panel superior de la figura 7, la forma de la curva calculada en ambos casos es bastante diferente debido a la energía de excitación inducida en la etapa de colisión. En el caso de la reacción ^{208}Pb+d a 500 A MeV (panel inferior de la figura 7), existe un buen acuerdo entre cálculos realizados con INCL+ABLA considerando $\beta = 4{,}0 \times 10^{21}\ s^{-1}$ y los datos experimentales.

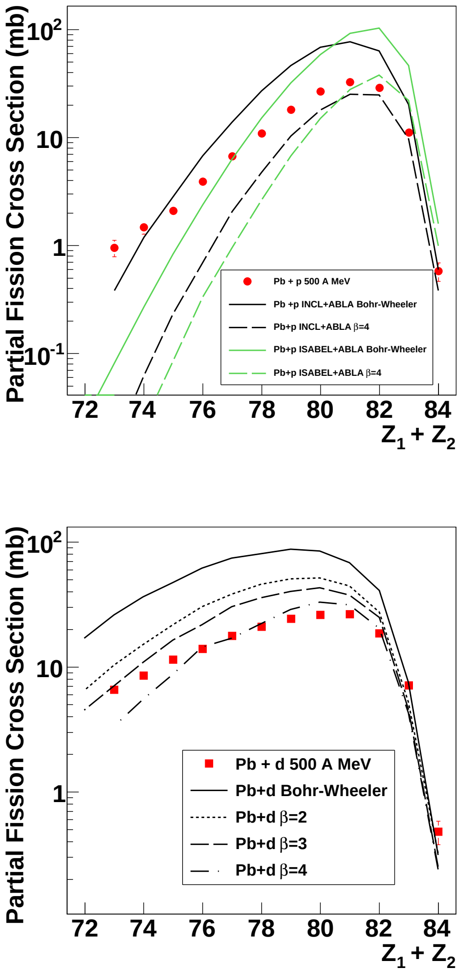

Figura 7: Panel superior: Sección eficaz parcial en función de Z_1+Z_2 para la reacción ^{208}Pb+p a 500 A MeV en comparación con cálculos realizados con INCL+ABLA (negro) and ISABEL+ABLA (verde) con $\beta = 0$ (línea sólida) y $\beta = 4{,}0 \times 10^{21}\ s^{-1}$ (línea a trazos), respectivamente. Panel inferior: Sección eficaz parcial en función de Z_1+Z_2 para la reacción ^{208}Pb+d a 500 A MeV en comparación con cálculos realizados con INCL+ABLA para varios valores de β.

Sin embargo, la sección eficaz no es un buen observable para inferir efectos de tránsito en sistemas fisionantes. Para poder extraer alguna conclusión cuantitativa, comparamos σ_z en función de Z$_1$+Z$_2$ con cálculos realizados con INCL+ABLA. Como se puede observar en la figura 8, los cálculos considerando $\beta = 0\ s^{-1}$ sobreestiman los valores experimentales de σ_z. Es necesario introducir un valor de $\beta = 4{,}0 \times 10^{21}\ s^{-1}$ en los cálculos que nos permite deducir que el tiempo de tránsito reduce σ_z, y por consiguiente, T$_{sad}$.

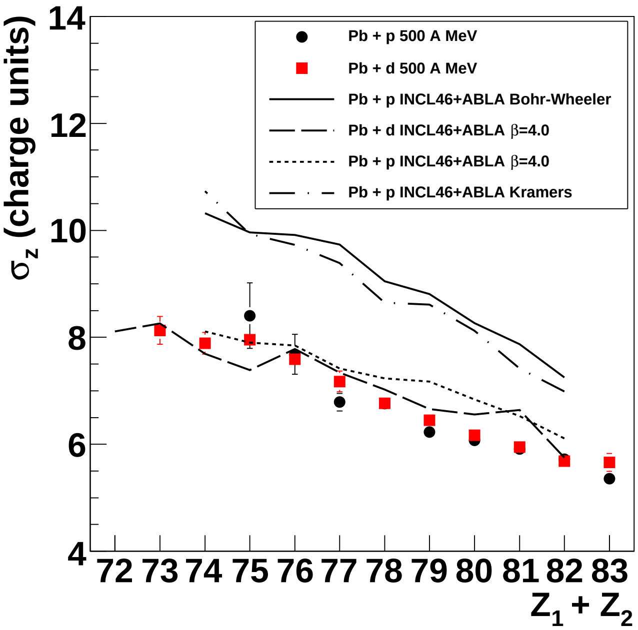

Figura 8: σ_z en función de Z_1+Z_2 para las dos reacciones estudiadas en este trabajo en comparación con cálculos realizados con INCL+ABLA.

Futuros experimentos de fisión y necesidad de mejorar las medidas de tiempo de vuelo.

Los experimentos de fisión de próxima generación que utilizarán la técnica de cinemática inversa (SOFIA, R^{3}B y FELISe), incluirán detectores modernos y punteros adecuados a los elevados requisitos necesarios para proveer medidas completas de alta precisión. Uno de los mayores retos lo constituye la identificación isotópica de ambos fragmentos de fisión simultaneamente.

Hemos visto que es posible determinar con gran precisión el número atómico de los fragmentos de fisión con buena resolución, sin embargo, para separar isotópicamente los fragmentos de fisión, es necesario un muro de tiempo de vuelo con una alta resolución temporal. En este documento se describe el trabajo de investigación y desarrollo llevado a cabo para considerar la construcción de un muro de tiempo de vuelo basado en cámaras de placas resistivas (RPCs) para el experimento R^3B. Estos detectores gaseosos funcionan aplicando un campo eléctrico intenso (100 kV/cm) entre dos electrodos resistivos de geometría planoparalela, de tal manera que una partícula que ioniza el gas contenido en el *gap* definido entre los dos electrodos, provoca una avalancha Townsend que induce una señal muy rápida en los electrodos. La información acerca del funcionamiento de dichos detectores para la detección de iones pesados a energías relativistas es bastante escasa, y por lo tanto es necesaria una caracterización que pruebe su viabilidad para dicho propósito.

Para ello hemos construido varios prototipos de RPCs de diferentes tamaños, con el propósto de caracterizarlos (junto a la electrónica desarollada conjuntamente) en diversos experimentos con iones pesados y electrones. Los resultados más concluyentes se obtuvieron con un prototipo (RPC-25) que consistía en dos módulos de RPC independientes con un tamaño de 15 cm × 7 cm y con un solo *strip* o pista de cobre de 20 mm de anchura , construídos con vidrio de 1 mm de espesor definiendo una estructura de doble *gap* de 300 μm. Para las medidas, ambos módulos se metieron en el interior de una caja de aluminio estanca para preservar el flujo de gas. Además, obtuvimos resultados comparables con un prototipo (RPC-30) consistente en dos módulos independientes de 40 cm × 20 cm de tamaño y con 5 *strips* de cobre de 20 cm de anchura. La mayor diferencia respecto al prototipo anterior es que cada módulo se ensambló únicamente pegando dos vidrios de 1 mm de espesor definiendo una estructura estanca de un solo *gap* de 300 μm con la mínima cantidad posible de materia. En todos las medidas con estos prototipos hemos usado una mezcla gaseosa que contiene 90 % de $C_2H_2F_4$ y 10 % of SF_6,

El prototipo RPC-25 se testó con un haz que suministraba electrones en paquetes de alrededor de 10^4 electrones, a una energía de 10 MeV y a diferentes intensidades, obteniendo valores excelentes de resolución temporal alcanzando valores de resolución temporal de alrededor de 35 ps para una intensidad del haz del 22 % y un voltaje del detector de 2800 V. La carga de la señal inducida en este case era proporcional a la intensidad del haz. Este mismo prototipo se utilizó en un experimento donde fué irradiado con un haz de ^{238}U a 1 A GeV de energía con una tasa de 10 Hz/cm^2 obteniendo un valor de la resolución temporal de 69 ps operando el detector con un voltaje de 2800 V. Por otra parte, el prototipo RPC-30 se caracterizó en un experimento para medir iones de ^{136}Xe a 560 A MeV de energía, con unas tasas de 1-2 Hz/cm^2 y 3-5 Hz/cm^2. A 2800 V de voltaje de operación y una tasa de irradiación de 1-2 Hz/cm^2, se obtuvo una resolución temporal de 47 ps y una eficiencia de detección cercana al 100 %. A tasas mayores la resolución temporal se degrada, obteniendo un valor de la resolución temporal de 60 ps para una tasa de 3-5 Hz/cm^2. Estos resultados se compilan en la figura 9, representando la resolución temporal en función de la carga de la señal inducida en los electrodos para poder comparar los datos obtenidos en todos los experimentos.

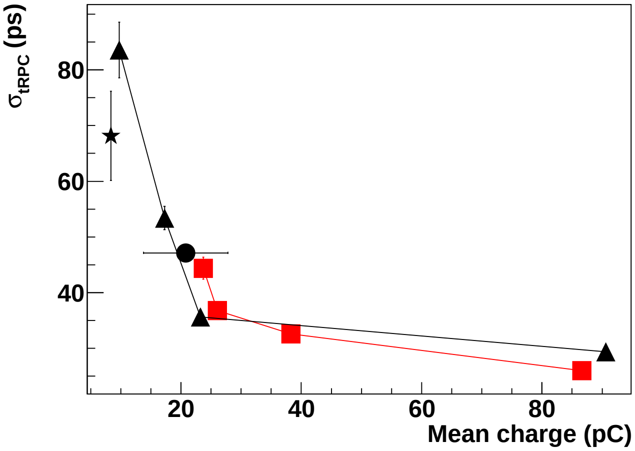

Figura 9: Resolución temporal en función de la carga. RPC-25 con paquetes de electrones (triángulos) y con ^{238}U (estrella), RPC-30 con ^{136}Xe (círculo).

Teniendo en cuenta estos resultados podemos concluir que las RPCs pueden ser usadas para la detección y medida de tiempo de iones pesados relativistas cubriendo un rango amplio en número atómico, obteniendo resoluciones temporales por debajo de los 50 ps y eficiencias de detección cercanas al 100 % siempre teniendo en cuenta que la tasa de irradiación por unidad de superficie afecta drásticamente al funcionamiento del detector. Esto abre la posibilidad de construir un muro de tiempo de vuelo para el experimento de R^{3}B basados en RPCs teniendo en cuenta los requisitos más importantes de dicho detector.

En conclusión, en este trabajo se ha investigado el proceso de fisión a alta energía de excitación usando la técnica de cinemática inversa. En particular se han estudiado las reacciones ^{181}Ta+p a 300, 500, 800 y 1000 A MeV, y ^{208}Pb+p y ^{208}Pb+d a 500 MeV. Se han estudiado los efectos dinámicos en el proceso de fisión en estas reacciones con la ayuda de códigos punteros que describen este proceso en dos etapas: cascada intranuclear y evaporación. Se han validado estos códigos mediante comparación con los datos experimentales.

Por otra parte hemos demostrado la validez de las RPCs para la detección de iones pesados con energías relativistas, a través de un programa extenso de I+D donde hemos probados diversos prototipos en experimentos con diversos tipos de iones. Los resultados indican que bajo ciertas condiciones, estos detectores ofrecen excelentes resoluciones temporales por debajo de los 50 ps manteniendo una eficiencia de detección cercana al 100 %, lo que los convierte en sólidos candidatos para la construcción de un muro de tiempo de vuelo para el futuro experimento de R^{3}B.

Bibliography

[Abb98] M. Abbrescia *et al.*, *Beam test results on double-gap resistive plate chambers proposed for CMS experiment*, Nuclear Instruments and Methods in Physics Research Section A: Accelerators, Spectrometers, Detectors and Associated Equipment **414** (1998) 135 – 148, ISSN 0168-9002.

[Aie04] G. Aielli *et al.*, *Test and performances of the RPC trigger chambers of the ATLAS experiment at LHC*, Nuclear Instruments and Methods in Physics Research Section A: Accelerators, Spectrometers, Detectors and Associated Equipment **533** (2004) 193 – 198, ISSN 0168-9002.

[Aki09] A. Akindinov *et al.*, *Final test of the MRPC production for the ALICE TOF detector*, Nuclear Instruments and Methods in Physics Research Section A: Accelerators, Spectrometers, Detectors and Associated Equipment **602** (2009) 709 – 712, ISSN 0168-9002.

[AMA] *AMADEUS is available online at*, `http://www-wnt.gsi.de/CHARMS/amadeus.htm`.

[Amm07] V. Ammosov *et al.*, *The HARP resistive plate chambers: Characteristics and physics performance*, Nuclear Instruments and Methods in Physics Research Section A: Accelerators, Spectrometers, Detectors and Associated Equipment **578** (2007) 119 – 138.

[Amm10] V. Ammosov *et al.*, *Time resolution of a 6-gap resistive plate chamber with strip readout*, Instruments and Experimental Techniques **53** (2010) 175–179, 10.1134/S0020441210020041.

[AP06] H. Alvarez-Pol *et al.*, *Conceptual design of a large area time-of-flight wall for the R3B experiment at FAIR*, Nuclear Physics B - Proceedings Supplements **158** (2006) 186 – 189.

[Arm70] P. Armbruster, *On the calculation of charge values of fission fragments*, Nuclear Physics A **140** (1970) 385 – 399.

[Ayy12] Y. Ayyad *et al.*, *First results with RPC prototypes for the detection of relativistic heavy-ions at the R3B experiment*, Nuclear Instruments and Methods in Physics Research Section A: Accelerators, Spectrometers, Detectors and Associated Equipment **661, Supplement 1** (2012) S141 – S144.

[Bac00] C. Bacci *et al.*, *Results from the analysis of data collected with a 50m2 RPC carpet at YangBaJing*, Nuclear Instruments and Methods in Physics Research Section A: Accelerators, Spectrometers, Detectors and Associated Equipment **456** (2000) 121 – 125.

[Bai10] A. Bail, *Workshop on Large-Area-Picosecond-Photodetectors electronics for particle physics and medical imaging, LPC, France* (2010).

[Bar62] V. I. Baranovskiy, A. N. Murin and B. K. Preobrazhenskiy, Radiokhimiya **4** (1962) 470.

[Ben01] J. Benlliure *et al.*, *Isotopic production cross sections of fission residues in 197Au-on-proton collisions at 800 A MeV*, Nuclear Physics A **683** (2001) 513 – 539, ISSN 0375-9474.

[Ben02] J. Benlliure *et al.*, *Signatures of fission dynamics in highly excited nuclei produced in 197Au (800A MeV) on proton collisions*, Nuclear Physics A **700** (2002) 469 – 491.

[Ber84] J. Berger, M. Girod and D. Gogny, *Microscopic analysis of collective dynamics in low energy fission*, Nuclear Physics A **428** (1984) 23 – 36.

[Ber03] M. Bernas *et al.*, *Fission-residues produced in the spallation reaction 238U + p at 1 A GeV*, Nuclear Physics A **725** (2003) 213 – 253.

[Bha86] K. H. Bhatt, P. Grangé and B. Hiller, *Nuclear friction and lifetime of induced fission*, Phys. Rev. C **33** (1986) 954–968.

[Bla92] T. Blaich *et al.*, *A large area detector for high-energy neutrons*, Nuclear Instruments and Methods in Physics Research Section A: Accelerators, Spectrometers, Detectors and Associated Equipment **314** (1992) 136 – 154.

[Bla09] A. Blanco *et al.*, *In-beam measurements of the HADES-TOF RPC wall*, Nuclear Instruments and Methods in Physics Research Section A: Accelerators, Spectrometers, Detectors and Associated Equipment **602** (2009) 691 – 695.

[Blo78] J. Blocki *et al.*, *One-body dissipation and the super-viscidity of nuclei*, Annals of Physics **113** (1978) 330 – 386.

[Boc78] B. A. Bochagov *et al.*, Sov. J. Nucl. Phys. **28** (1978) 291.

[Boh39] N. Bohr and J. A. Wheeler, *The Mechanism of Nuclear Fission*, Phys. Rev. **56** (1939) 426–450.

[Bou02] A. Boudard *et al.*, *Intranuclear cascade model for a comprehensive description of spallation reaction data*, Phys. Rev. C **66** (2002) 044615.

[Bur96] R. Burman and L. Daemen, Nucl. Instr. and Meth. Phys. Res. A **370** (1996) 335–340.

[Bus05] M. Bussa, *The PANDA experiment at FAIR*, Czechoslovak Journal of Physics **55** (2005) A279–A288.

[Cab09] P. Cabanelas *et al.*, *Performances of 4-gap timing RPCs for relativistic ions in the range Z = 16*, Journal of Instrumentation **4** (2009) P11007.

[Car88] R. Cardarelli *et al.*, *Progress in resistive plate counters*, Nuclear Instruments and Methods in Physics Research Section A: Accelerators, Spectrometers, Detectors and Associated Equipment **263** (1988) 20 – 25.

[Cas12a] E. Casarejos *et al.*, *Design of iToF: A ToF-wall detector to identify relativistic ions in R3B-FAIR*, Nuclear Instruments and Methods in Physics Research Section A: Accelerators, Spectrometers, Detectors and Associated Equipment **661, Supplement 1** (2012) S137 – S140.

[Cas12b] E. Casarejos *et al.*, *Detection efficiency of relativistic heavy-ions with resistive-plate chambers*, Nuclear Instruments and Methods in Physics Research Section A: Accelerators, Spectrometers, Detectors and Associated Equipment **674** (2012) 39 – 45.

[Cha01] G. Chaudhuri and S. Pal, *Fission widths of hot nuclei from Langevin dynamics*, Phys. Rev. C **63** (2001) 064603.

[Cla03] K. N. Clausen, ESS, The European Spallation Source, ICANS XVI, 16th Meeting of the International Collaboration on Advanced Neutron Sources Düsseldorf Neuss, Germany. (2003).

[Dus01] S. Dusini *et al.*, *Design and prototype tests of the RPC system for the OPERA spectrometers* (2001) 117 – 120.

[Enq01] *Isotopic yields and kinetic energies of primary residues in 1 A GeV 208Pb+p reactions*, Nuclear Physics A **686** (2001) 481 – 524.

[FAI] *FAIR web page*, `http://www.gsi.de/fair/`.

[FD05] B. Fernández-Domínguez *et al.*, *Nuclide cross-sections of fission fragments in the reaction 208Pb + p at 500 A MeV*, Nuclear Physics A (2005) 227 – 267.

[Fon69] P. Fong, *Statistical Theory of Nuclear Fission*, Cordon and Breach, New York (1969).

[Fon00] P. Fonte, A. Smirnitski and M. Williams, *A new high-resolution TOF technology*, Nuclear Instruments and Methods in Physics Research Section A: Accelerators, Spectrometers, Detectors and Associated Equipment **443** (2000) 201 – 204.

[Fon02] P. Fonte, *Applications and new developments in resistive plate chambers*, Nuclear Science, IEEE Transactions on **49** (2002) 881 – 887.

[Frö98] P. Fröbrich and I. Gontchar, *Langevin description of fusion, deep-inelastic collisions and heavy-ion-induced fission*, Physics Reports **292** (1998) 131 – 237, ISSN 0370-1573, doi:10.1016/S0370-1573(97)00042-2.

[Fuk90] T. Fukahori and S. Pearlstein, Proceedings of the Advisory Group Meeting Organized by IAEA, Vienna, October (1990) 9–12.

[Gai91] J. J. Gaimard and K. H. Schmidt, *A reexamination of the abrasion-ablation model for the description of the nuclear fragmentation reaction*, Nuclear Physics A **531** (1991) 709 – 745.

[Gav81] A. Gavron *et al.*, *Time Scale of Fission at High Angular Momentum*, Phys. Rev. Lett. **47** (1981) 1255–1258.

[Gav82] A. Gavron *et al.*, *Time Scale of Fission at High Angular Momentum*, Phys. Rev. Lett. **48** (1982) 835–836.

[Gei92] H. Geissel *et al.*, *The GSI projectile fragment separator (FRS): a versatile magnetic system for relativistic heavy ions*, Nuclear Instruments and Methods in Physics Research Section B: Beam Interactions with Materials and Atoms **70** (1992) 286 – 297.

[Gei03] H. Geissel *et al.*, *The Super-FRS project at GSI*, Nuclear Instruments and Methods in Physics Research Section B: Beam Interactions with Materials and Atoms **204** (2003) 71 – 85, 14th International Conference on Electromagnetic Isotope Separators and Techniques Related to their Applications.

[Gol99] F. Goldenbaum *et al.*, *Fission Time Evolution with Excitation Energy from a Crystal Blocking Experiment*, Phys. Rev. Lett. **82** (1999) 5012–5015.

[Gou05] H. Goutte *et al.*, *Microscopic approach of fission dynamics applied to fragment kinetic energy and mass distributions in* ^{238}U, Phys. Rev. C **71** (2005) 024316.

[Gra83] P. Grangé, L. Jun-Qing and H. A. Weidenmüller, *Induced nuclear fission viewed as a diffusion process: Transients*, Phys. Rev. C **27** (1983) 2063–2077.

[Gro75] D. Gross, *Theory of nuclear friction*, Nuclear Physics A **240** (1975) 472 – 484.

[Hah39] O. Hahn and F. Strassmann, *Über den Nachweis und das Verhalten der bei der Bestrahlung des Urans mittels Neutronen entstehenden Erdalkalimetalle*, Naturwissenschaften **27** (1939) 89.

[Hau52] W. Hauser and H. Feshbach, *The Inelastic Scattering of Neutrons*, Phys. Rev. **87** (1952) 366–373.

[Hil92] D. Hilscher and H. Rossner, *Dynamics of nuclear fission*, Ann. Phys. Fr. **17** (1992) 471.

[Hin92] D. J. Hinde *et al.*, *Neutron emission as a probe of fusion-fission and quasifission dynamics*, Phys. Rev. C **45** (1992) 1229–1259.

[Hof97] H. Hofmann, *A quantal transport theory for nuclear collective motion: The merits of a locally harmonic approximation*, Physics Reports **284** (1997) 137 – 380.

[Hof01] H. Hofmann *et al.*, *Nuclear fission: The "onset of dissipation" from a microscopic point of view*, Phys. Rev. C **64** (2001) 054316.

[Ign75] A. V. Ignatyuk *et al.*, Sov. J. Nucl. Phys. **21** (1975) 612.

[ISO] *ISOLDE web page:*, `http://isolde.web.cern.ch/isolde/`.

[Jon97] M. de Jong, A. Ignatyuk and K.-H. Schmidt, *Angular momentum in peripheral fragmentation reactions*, Nuclear Physics A **613** (1997) 435 – 444.

[Jur03] B. Jurado, K.-H. Schmidt and J. Benlliure, *Time evolution of the fission-decay width under the influence of dissipation*, Physics Letters B **553** (2003) 186 – 190.

[Jur04] B. Jurado *et al.*, *Transient Effects in Fission from New Experimental Signatures*, Phys. Rev. Lett. **93** (2004) 072501.

[Jur05] B. Jurado *et al.*, *A critical analysis of the modelling of dissipation in fission*, Nuclear Physics A **747** (2005) 14 – 43.

[Kar75] P. J. Karol, *Nucleus-nucleus reaction cross sections at high energies: Soft-spheres model*, Phys. Rev. C **11** (1975) 1203–1209.

[Kel09] A. Kelic, M. V. Ricciardi and K.-H. Shcmidt, ArXiv:0906.4193.v1. (2009).

[Kiš11] M. Kiš *et al.*, *A Multi-strip Multi-gap RPC Barrel for Time-of-Flight Measurements*, Nuclear Instruments and Methods in Physics Research Section A: Accelerators, Spectrometers, Detectors and Associated Equipment **646** (2011) 27 – 34.

[Koc05] K. Koch *et al.*, *A new TAC-based multichannel front-end electronics for TOF experiments with very high time resolution*, Nuclear Science, IEEE Transactions on **52** (2005) 745 – 747.

[Kon66] V. A. Konshin, Sov. J. Nucl. Phys. **2** (1966) 489.

[Kra40] H. A. Kramers, Physika VII (1940) 284.

[LAN] *LAND web page*, `http://www.gsi.de/forschung/kp/kp2/collaborations/land/index_e.html`.

[M2J] *M2J Company, France, MATACQ32 chip based VME boards.*

[Man10] D. Mancusi, R. J. Charity and J. Cugnon, *Unified description of fission in fusion and spallation reactions*, Phys. Rev. C **82** (2010) 044610.

[Mau65] M. Maurette and C. Stephan, Proc. Int. Conf. Physics and Chemistry of Fission, Salzburg, austria, March 22-26 (1965).

[MBS] *MBS web page:*, `http://www-win.gsi.de/daq/`.

[Mol93] J. D. Molitoris *et al.*, *Molecular-orbital study of late-fission times in deep-inelastic* ^{238}U+^{238}U *collisions*, Phys. Rev. Lett. **70** (1993) 537–540.

[Möl01] P. Möller *et al.*, *Nuclear fission modes and fragment mass asymmetries in a five-dimensdional deformation space*, Nature **409** (2001) 785.

[Mor75] L. G. Moretto, *Statistical emission of large fragments: A general theoretical approach*, Nuclear Physics A **247** (1975) 211 – 230.

[Mor95] L. G. Moretto *et al.*, Phys. Rev. Lett. **75** (1995) 4186.

[Nif01] H. Nifenecker *et al.*, Nucl. Instr. and Meth. A **463** (2001) 428.

[Nis03] S. Nishimura *et al.*, *Systematic studies of scintillation detector with timing resolution of 10 ps for heavy ion beam*, Nuclear Instruments and Methods in Physics Research Section A: Accelerators, Spectrometers, Detectors and Associated Equipment **510** (2003) 377 – 388.

[Nör83] W. Nörenberg, *Dissipative diabatic dynamics: A shell-model approach to large-amplitude collective nuclear motion*, Nuclear Physics A **409** (1983) 191 – 211.

[Par] C. Paradela *et al.*, *In preparation* .

[Pau94] P. Paul and M. Thoennessen, Phys. Rev. C **44** (1994) 65.

[Per07] J. Pereira *et al.*, *Isotopic production cross sections and recoil velocities of spallation-fission fragments in the reaction 238U(1A GeV) + d*, Physical Review C (Nuclear Physics) **75** (2007) 014602.

[Pfü94] M. Pfützner *et al.*, *Energy deposition by relativistic heavy ions in thin argon absorbers*, Nuclear Instruments and Methods in Physics Research Section B: Beam Interactions with Materials and Atoms **86** (1994) 213 – 218.

[PL11] D. Pérez-Loureiro *et al.*, *Production of neutron-rich nuclei in fragmentation reactions of projectiles at relativistic energies*, Physics Letters B **703** (2011) 552 – 556.

[Pro01] A. V. Prokofiev, Nucl. Instr. and Meth. Phys. A **463** (2001) 557.

[R3B] *R3B web page*, `http://www.gsi.de/forschung/kp/kr/R3B_e.html`.

[Ris89] H. Risken, *The Fokker-Planck Equation*, Springer, Berlin (1989).

[Rus97] A. Y. Rusanov, M. G. Itkis and V. N. Okolovic, Phys. At. Nucl. **60** (1997) 683.

[San81] R. Santonico and R. Cardarelli, *Development of resistive plate counters*, Nuclear Instruments and Methods in Physics Research **187** (1981) 377 – 380.

[Sax94] A. Saxena *et al.*, *Entrance channel effects in the fusion-fission time scales from studies of prescission neutron multiplicities*, Phys. Rev. C **49** (1994) 932–940.

[Sch00] K.-H. Schmidt *et al.*, *Relativistic radioactive beams: A new access to nuclear-fission studies*, Nuclear Physics A **665** (2000) 221 – 267, ISSN 0375-9474.

[Sch04] A. Schüttauf, *Timing RPCs in FOPI*, Nuclear Instruments and Methods in Physics Research Section A: Accelerators, Spectrometers, Detectors and Associated Equipment **533** (2004) 65–68.

[Sch10] C. Schmitt *et al.*, *Fragmentation of spherical radioactive heavy nuclei as a novel probe of transient effects in fission*, Phys. Rev. C **81** (2010) 064602.

[Sci07] Scientific Discovery through Advanced Computing (2007), issue 6, Winter.

[Ser47] R. Serber, *Nuclear Reactions at High Energies*, Phys. Rev. **72** (1947) 1114–1115.

[Shi73] O. E. Shigaev *et al.*, Rept. Khlopin Radiev. Inst., Leningrad Reports **17** (1973).

[Sie86] A. J. Sierk, *Macroscopic model of rotating nuclei*, Phys. Rev. C **33** (1986) 2039–2053.

[Ste67] C. Stephan and M. L. Perlman, Phys. Rev. **164** (1967) 1528.

[Ste91] H. Stelzer, *Multiwire chambers with a two-stage gas amplification*, Nuclear Instruments and Methods in Physics Research Section A: Accelerators, Spectrometers, Detectors and Associated Equipment **310** (1991) 103 – 106.

[Str67] V. Strutinsky, *Shell effects in nuclear masses and deformation energies*, Nuclear Physics A **95** (1967) 420 – 442.

[Tar11] D. Tarrío *et al.*, *Neutron-induced fission cross section of* $^{\mathrm{nat}}$*Pb and* ^{209}Bi *from threshold to 1 GeV: An improved parametrization*, Phys. Rev. C **83** (2011) 044620.

[Tho93] M. Thoennessen and G. F. Berstch, Phys. Rev. Lett. **71** (1993) 4303.

[Vai10] L. A. Vaishnene *et al.*, *Isotopic effect in the energy dependence of the total fission cross section of lead and 209Bi nuclei for protons with energies up to 1 GeV*, Bulletin of the Russian Academy of Sciences: Physics **74** (2010) 496–499.

[Wan10] Y. Wang *et al.*, *Production and quality control of STAR-TOF MRPC*, Nuclear Instruments and Methods in Physics Research Section A: Accelerators, Spectrometers, Detectors and Associated Equipment **613** (2010) 200 – 206.

[Wei80] H. A. Weidenmüller, Prog. Part. Nucl. Phys. **3** (1980) 49.

[Wil76] B. D. Wilkins, E. P. Steinberg and R. R. Chasman, *Scission-point model of nuclear fission based on deformed-shell effects*, Phys. Rev. C **14** (1976) 1832–1863.

[Wil04] H. Wilschut and V. Kravchuk, *Developing an atomic clock for fission lifetime measurements*, Nuclear Physics A **734** (2004) 156 – 163.

[Yar79] Y. Yariv and Z. Fraenkel, *Intranuclear cascade calculation of high-energy heavy-ion interactions*, Phys. Rev. C **20** (1979) 2227–2243.

[Ye12] W. Ye, *Spallation reactions induced by high energy protons: A possible way to probe dissipation in nuclear fission with excitation energy at scission*, Phys. Rev. C **85** (2012) 011601.

[Yur05] V. I. Yurevich *et al.*, Jour. Fiz. Elementarnykh Chastic i Atomn. Yadra, Letters **2** (2005) 49.

[Zal00] A. Zallo, *The BaBar RPC system*, Nuclear Instruments and Methods in Physics Research Section A: Accelerators, Spectrometers, Detectors and Associated Equipment **456** (2000) 117 – 120.

[Zeb96] E. C. Zeballos *et al.*, *A new type of resistive plate chamber: The multigap RPC*, Nuclear Instruments and Methods in Physics Research Section A: Accelerators, Spectrometers, Detectors and Associated Equipment **374** (1996) 132 – 135.